



UNIVERSITÀ
DEGLI STUDI
FIRENZE

DOTTORATO DI RICERCA IN
SCIENZE DELLA TERRA

CICLO XXXI

*MODELING INFRASONIC SOURCES RELATED TO
DENSITY CURRENTS*

Settore Scientifico Disciplinare GEO/10

Dottorando

Dott. Giulia Barfucci

Tutore

Prof. Maurizio Ripepe

Dott. Matteo Cerminara

Prof. Emanuele Marchetti

Coordinatore

Prof. Lorella Francalanci

Anni 2015/2018

Abstract

Pyroclastic Density Currents (PDCs) are among the most impressive, and hazardous phenomena of volcanic activity. Understanding their dynamics remains a major challenge. Gravity driven flows, dominated by the fluid-particles interaction, are in fact difficult to access for field measurements and complex to model and describe numerically. To date, the use of infrasonic arrays has shown to be able to detect and track PDC's run-out automatically and in real-time, strongly improving the monitoring of this dangerous volcanic activity. However, relying only infrasonic (or seismic) signal we are not able yet to quantify physical parameters of the PDC, strongly limiting our ability to timely assess the correct volcanic hazard. We here present a new integrated approach that, by the aid of computational modeling, aims to find theoretical and empirical relations between the geophysical signal and the dynamical properties of the flow. In particular we show that, for a dilute PDC the upper and turbulent part of the flow is well developed and coupled with the atmosphere and thus is very effective in generating infrasound. We use the ASHEE model to simulate the dynamic evolution of the gas-particle density current, including the infrasound generation and propagation process. The relationship between PDCs dynamics and acoustic wave-field is explored by varying both numerical and initial conditions in a stratified atmosphere. Comparing synthetic signal with real infrasound recorded associated with density currents activity, we find a strong correlation between the frequency content of the signal and the dimensions of the density current. Our study may have strong implication in terms of hazard assessment. Infrasonic signals could be used to remotely estimate physical properties of PDCs dynamics providing data to constrain observations and improve our ability to monitor such phenomena.

Contents

1	Introduction	7
1.1	Density currents	8
1.1.1	Pyroclastic density currents	9
1.1.2	Snow avalanches	10
1.1.3	Rock and debris avalanches	11
1.2	Acoustic monitoring of surficial mass movements	12
1.3	Aims and objectives	13
1.4	Outline of the work	14
1.5	Scientific outcomes	15
2	Geophysical observations: Long range acoustic propagation, the 21 July 2014 Askja landslide	17
2.1	Introduction	18
2.2	Infrasound Monitoring in Iceland	20
2.3	Askja landslide event and Infrasound detection	22
2.4	Modelling of in the infrasonic propagation	23
3	Geophysical observations: Dome collapse activity and PDCs production	29
3.1	Geophysical analysis of the collapse event and the following explosive phase	30
3.1.1	Abstract	30
3.1.2	Introduction	30
3.1.3	Instrumentation and Data Acquisition	32
3.1.4	Geophysical Observation of the Dome Collapse	32
3.1.5	Gravitational Dome Instability and the Materials Failure Law	35
3.1.6	Atmospheric Gravity Waves of PDC	37
3.1.7	Eruptive Source Parameters of Vulcanian Explosion	38

3.1.8	Discussion and Conclusions	41
3.2	Snow and Rock avalanche events	42
4	Geophysical observations: Debris flows activity, the Illgraben case study	49
4.1	Abstract	50
4.2	Introduction	51
4.3	Study site	53
4.4	Instrumental setup	54
4.5	Debris flow events	56
4.5.1	Infrasound array analysis of debris-flows	59
4.5.2	Spectral analysis of debris-flows	64
4.6	Discussion	65
4.6.1	Mechanisms of infrasound radiation by debris flow at Illgraben	65
Numerical simulation of infrasound radiated by an extended source.	68	
4.6.2	Seismo-acoustic coupling of radiated elastic energy	70
4.6.3	Use of infrasound monitoring as an early warning system for debris-flows	72
4.7	Conclusions	74
5	Modeling the infrasonic sources related to density currents	77
5.1	Background	78
5.1.1	Density currents and dam break configuration	78
5.1.2	Box-model	81
5.1.3	Multiphase flow modeling	83
5.2	Numerical simulations	86
5.2.1	The ASHEE code	86
5.2.2	Simulations setup	92
5.2.3	Simulations strategy	95
5.3	Analysis of numerical results	96
5.3.1	Gravity current evolution	96
5.3.2	Generation and propagation of acoustic waves	98
5.3.3	Comparison among different scales and initial condition	104

5.3.4	Dependence of the acoustic frequency from the typical source dimensions	107
5.3.5	Analysis of the numerical configuration	111
5.4	Chapter Conclusions	116
6	Discussion and Conclusions	119
6.1	Towards a quantitative use of infrasound: the frequency-magnitude relation	120
6.1.1	Numerical results	120
6.1.2	From the model to the real case	122
6.2	Linking current dynamics and acoustic emissions: a quest for explanation	124
6.2.1	Density currents as source of sound	124
6.2.2	Comparison between surficial mass movements with different dynamic	127
6.3	Conclusions	127
	Bibliography	140

Chapter 1

Introduction

This thesis concerns with the analysis of infrasonic signals produced by density currents, also referred as gravity currents, which are moving flows driven by density contrast in the gravity field.

Such multi-phase flows, characterized by turbulent dynamics, comprises a variety of other geophysical flows, for instance powder snow avalanches and rock or debris avalanches. Due to their intrinsic risk, the study of these phenomena plays an important role in many problems related to civil and environmental protection. Among gravity current, pyroclastic flows, constituted by suspended solid particles in an hot gas mixture, represent one of the most hazardous phenomena of volcanic activity.

The sudden occurrence, often with no evident precursors, the rapid evolution, and the possibly large traveled distances, set these phenomena as an open challenge for geophysical monitoring. Recently, effective advances towards a more efficient geophysical monitoring have been made applying seismic and acoustic techniques. To date, infrasound seems to be the most promising technique to detect and locate gravity currents in nature, and is becoming increasingly used. However, given the complexity of these phenomena, a source model describing the acoustic wavefield generated by density current dynamics is still lacking.

Therefore, extracting quantitative information from the acoustic and seismic signals generated by surficial mass movements remains an outstanding challenge [1].

In this thesis we present geophysical observations of infrasonic wavefield produced by density currents. Then, we explore via numerical simulations the interaction between the turbulent dilute part of the density current and

the acoustic waves generated in the atmosphere. Finally, we discuss the relationship between model output and geophysical observations as a basis for inferring the physical processes underlying the acoustic emission from density currents.

1.1 Density currents

Gravity currents occur in both natural and men-made situations. Primarily they configure as horizontal flows. Often a density difference of just a few percent is enough to generate them [2]. The term "Density currents" denotes a variety of phenomena at different scales throughout nature. Examples include atmospheric current and thunderstorms, haboobs, avalanches, pyroclastic flows, lahar and seafloor turbidity currents.

In this study we focus on the surficial mass movements: density currents propagating at the ground-atmosphere interface. Among them we select those where dynamics are mainly characterized by the gas-particles interaction (i.e. PDCs and snow avalanches).

The internal structure of these currents is stratified, where a dense basal layer is underlying a dilute and turbulent region of suspended particles, which often represent the most voluminous and mobile portion of the current [3].

The leading edge of these flows forms a typical front zone where a characteristic head, deeper than the following flow, is usually formed. This raised head is a zone of breaking waves and intense mixing and plays an important part in the control of the following current.

When a relevant amount of water is contained in the mixture, such as in the case of debris flows or lahars, the behavior dramatically changes as the dynamics become controlled by water-particles interaction. By remaining channelized, these flows do not develop a rising head or a dilute suspended turbulent part.

In what follows we report a detailed description for the different types of phenomena investigated in this work.

1.1.1 Pyroclastic density currents

Pyroclastic density currents (PDCs) are highly destructive products of the volcanic activity. They are high-speed, gravity-driven flows of hot (up to $\sim 600 - 800^\circ\text{C}$) gas-particle mixtures, ranging widely in nature from expanded, turbulent suspension currents, formed by the collapse of eruptive column or lateral blasts, to highly concentrated avalanches generated from the gravitational collapse of lava domes [4].

Individual currents can change concentration during its evolution in response to transport, entrainment, and interactions with topography. Regardless of their particle concentration almost all pyroclastic density currents have some component of dilute flow. The suspended particles in this highly turbulent region of the current are fine grained and well coupled in velocity with the gas phase.

In the dilute limit, the suspended load of a pyroclastic density current shows features analogous to other turbulent dilute particle-laden gravity currents, such as dust storms and turbidity currents [2]. The atmosphere is entrained in the current forming an elevated head with vigorous mixing followed by the body of the current and shaped by Kelvin-Helmholtz billows that occur when shear overcomes the stable density stratification of the current. In addition to entrainment, this dilute region also grows as a result of buoyancy as volcanic gases and the heated entrained gas expand, often representing the most voluminous and mobile portion of the current.

Although dominant in volume, the suspended load region of the current comprises only a portion of the overall mass and momentum of many currents [5]. As particles sediment out of the dilute regions of the current, they accumulate in a concentrated bed-load region in which the particle-particle interaction become important.

In very dilute and energetic currents, a bed-load region is not able to form a significant thickness, and the particles will quickly move from suspension to deposition. However, a relatively concentrated bed-load region likely develops in many pyroclastic density currents.

PDCs have typical volumes of $\sim 10^4 - 10^8 \text{ m}^3$ and can form deposits ranging in volume from much less than 1 km^3 to thousands of cubic kilometers [4, 3]. The hazards that these highly mobile flows pose to human



FIGURE 1.1: *Volcán de Fuego erupted violently about 44 kilometers west of Guatemala City on June 3, 2018, a large pyroclastic flows developed killing tens of people. Credit: Orlando Estrada/AFP/Getty Images.*

populations are significant also due to their ability to travel over distances of several kilometers to tens of kilometers.

1.1.2 Snow avalanches

Snow avalanches are a gravity current involving large amount of detached snow rapidly flowing down a hill or mountainside. This type of events occur in alpine regions as well as all the snow covered mountain areas throughout the world, often causing many casualties and damages.

The movement of a dry snow avalanche differs from that of an avalanche consisting of compacted and moist snow.

Powder-snow avalanches (involving dry snow) develop a stratified structure composed by a dense flow layer at the bottom of the avalanche [6], characterized by a high snow density (200 kg/m^3 to 400 kg/m^3), and by an upper snow "dust" cloud with small particles suspended by turbulent eddies of air generated by the entrainment of ambient air.

Such dynamics, characterizing this type of turbulent gravity current, are mainly similar to those described in the previous section for the PDCs.

On the other hand, wet avalanches usually occur when water percolates through the snowpack decreasing the strength of the snow, changing its mechanical properties.

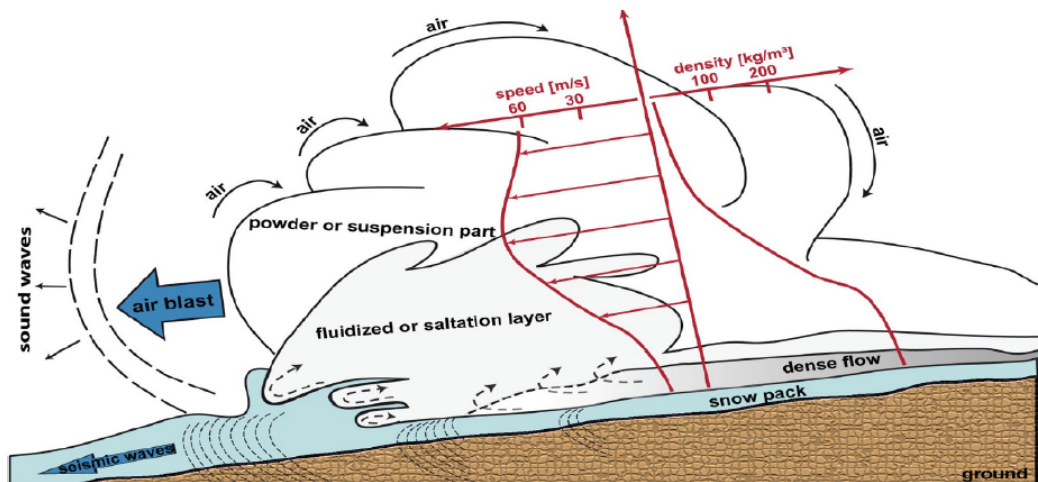


FIGURE 1.2: Sketch of a snow avalanche structure from [7].

The large amount of water contained in these flows significantly change their dynamics, in fact, no turbulent dust cloud of suspended material is formed during wet snow avalanche motion. This results in a completely different flow-atmosphere interaction compared to the PDCs and mixed-dry snow avalanches behaviour.

1.1.3 Rock and debris avalanches

Rock avalanches are large mass of mostly dry rock debris that can move for several kilometers down a valley slope or along the valley floor with a

velocity of several tens meters per second. They originate from the collapse of a slope or a cliff and may represent a potential risk for infrastructure and population.

Small rockfalls consist of one or more falling blocks descending with little fragmentation, while rock avalanches, involving larger volumes of material, can efficiently form cloud of finer material vigorously convected rising as coherent plumes for 300 – 1000 m.

Sudden catastrophic collapses generating debris avalanches can also occur in volcanic environments. On volcanoes, actively generated rock avalanches often evolve into pyroclastic flows which differentiate from typical rock avalanches by their larger size, longer runouts, greater production of fine ash and appreciable buoyant hot ash clouds [8].



FIGURE 1.3: *Example of rock avalanche.*

1.2 Acoustic monitoring of surficial mass movements

The pyroclastic flows movement down the flanks of the volcano excites seismic and infrasonic waves.

The seismic signal is thought to be mainly generated by interaction of the flow with the terrain while infrasound is interpreted as primarily caused by the turbulent motion of particles and air at the moving front, but nowadays we still lack a clear source model.

Infrasonic signals related to PDCs activity are characterized by typical cigar-shaped waveform (e.g. [9]) typical of most gravity current signals. Several hypothesis have been made to explain such gradually increasing signals, which imply a source that gradually builds up in time, growing momentum and size. Recent studies have demonstrated how infrasonic records, in particular provided from installation of infrasonic arrays at local and regional scale, can effectively enhance the monitoring capabilities of all geophysical phenomena occurring at the ground-atmosphere interface. The use of arrays, instead of single sensors, has in fact significantly improved the efficiency in detection of such events providing, at the same time, information about location and velocities of these moving sources [10, 11]. In spite of its potential, infrasound technology is relatively young and still at the beginning of its development. Hence, major basic questions still abound. In particular, the source mechanism for infrasound from mass movements is still unknown. In particular, retrieving quantitative information, such as flow volumes and event magnitude, from infrasound (as well as seismic) alone is currently not yet feasible. Advancing in the theoretical understanding of the acoustic source associated to density currents dynamics will be crucial in order to relate the seismo-acoustic signals to the source parameters. Numerical simulations, which proved to be a powerful tool to investigate a broad spectrum of natural phenomena, may probably help to tackle this issue. This would require joint numerical modeling of density current dynamics and their radiated acoustic wavefield.

1.3 Aims and objectives

Infrasound is increasingly used to detect and locate gravity currents, tracking their position in real time with the array technique. However, we are not able yet to derive quantitative information, such as the size of the current, from the infrasonic signal (nor seismic) alone. This is primarily due to the

lack of a source model describing the acoustic wavefield generated by density current dynamics. Improving our knowledge of these complex source mechanisms is an interesting scientific objective and it could be crucial for the correct assessment of the risk, to get information in real time from the infrasonic signal.

We present an integrated approach that uses a computational model to simulate together the density current dynamics and the corresponding acoustic wavefield.

Our main objective is first to understand the interaction between the turbulent dilute part of density currents and the atmosphere and second to find the relationship between the gravity-driven current and the associated acoustic signal. The ambition is to derive a general source model to explain the origin of infrasound related to density current and thus to move the use of infrasound toward a more effective application to the monitoring of surficial mass movements.

1.4 Outline of the work

The backbone of this thesis funded on three papers, here adapted to form an organic work. An additional one, still at preliminary stage, and describing the long-range propagation of infrasound produced during the Askja landslide in 2014 is also included.

In this first chapter, we introduce the thematic of the research with a brief anamnesis of the state of the art. In particular different types of density current phenomena, such as snow or debris avalanches and pyroclastic flows are described along with the main techniques used for their monitoring.

Chapters two, three and four, forms together a sort of case-study section, where field records of the geophysical signals produced by gravity current are presented and discussed. For each chapter a different type of phenomena is explored.

The second chapter is focused on the analysis of infrasound data produced by the large intracrater Askja landslide, occurred on the 21 July 2014, which is here used to introduce and discuss the promising perspectives and limits of the infrasonic monitoring for sub-aerial density current events. This

event was in fact registered from relatively large distances (> 200 km) evidencing how the data analysis requires, under these circumstances to account for the atmospheric specifications.

The third chapter is introducing the main topic of investigation: the pyroclastic density currents. Here geophysical observations are reported and discussed, with particular emphasis on infrasound data and its contributions in the understanding of the complex dynamic of these phenomena. The comparison with other turbulent multi-phase flows, such as snow and debris avalanches, is also introduced to better confine the main topic of this work, focusing on the well-developed turbulent flow dynamics.

The fourth chapter extends the observations to a different type of density current, proposing the case of debris-flows-related signals recorded at Illgraben (CH) site. The infrasound monitoring of these flows, strongly characterized by the water-particles interaction, probably represents one of the next challenges in this field.

The numerical modeling which represents a key part of this thesis, is fully explored in the fifth chapter. Numerical modeling offered in fact an efficient way to investigate the interaction between a well-developed turbulent flow front and the atmosphere, which is inferred to represent the main source of infrasound for flows with dilute PDC-like behavior. After a short background introduction, the ASHEE code is presented and the adopted strategy is motivated in details. Simulations and their numerical results are then shown and discussed. The relationship between the acoustic frequency and the typical source dimension concludes the chapter.

The two main results of this work are discussed in depth in the sixth chapter, organized in two sections: the first on the quantitative use of the infrasound to get information about the source dynamics and the second one, dealing with the possible source model to explain the acoustic wavefield.

We conclude summarizing the main results and future perspectives.

1.5 Scientific outcomes

Part of the scientific outcomes discussed in this thesis have been presented in a number of national and international conferences and documented through the international publications listed below.

- Preiswerk L. E., Walter F., Anandakrishnan S., **Barfucci G.**, et al., (2016). Monitoring unstable parts in the ice-covered Weissmies northwest face, interpraevent 2016, Conference Proceedings, pp.434-443.
- Ripepe M., **Barfucci G.**, De Angelis S., Lacanna G., Delle Donne D., Marchetti E., Modeling Volcanic Eruption Parameters by Near–Source Internal Gravity Waves. *Sci. Rep.* 6, 36727; doi:10.1038/srep36727 (2016).
- **Barfucci G.** and Ripepe, M. (2018). Dome collapse interaction with the atmosphere. *Geophysical Research Letters*, 45, 8923–8930.
- Marchetti M., Walter F., **Barfucci G.**, Genco R., et al., (2018) Seismo - acoustic observations of debris flow activity and implication for early warning, *Journal of Geophysical Research: Earth Surface*, 124.
- **Barfucci G.**, Ripepe M., Marchetti M., Lacanna G., Jónsdóttir K., Barsotti S. and Vogfjord K. S. (2018) An infrasonic arrays network for volcano monitoring in Iceland: analysis of the giant landslide event at Askja volcano, in preparation.
- **Barfucci G.**, Cerminara M., Ripepe M. (2018) A simple magnitude scale for turbulent gravity currents based on sound emission, in preparation.

All the research work about the modeling of the acoustic emission by density current dynamics (Chapter 5 and Chapter 6), as well as part of the geophysical observation originally appear in the present document.

Chapter 2

Geophysical observations: Long range acoustic propagation, the 21 July 2014 Askja landslide

Contents

2.1	Introduction	18
2.2	Infrasound Monitoring in Iceland	20
2.3	Askja landslide event and Infrasound detection	22
2.4	Modelling of in the infrasonic propagation	23

It is well known that infrasound can be successfully used to detect and locate energetic events from large distances. However when the source-receiver distance exceeds few to tens of kilometers, propagation effect may affect significantly acoustic signals. Moreover the atmospheric structure determine a "shadow zone", at a certain distance from the source, where acoustic records are not expected. In order to successfully analyze and interpret the infrasound data collected at large distances is hence mandatory to account for the atmospheric specifications. While propagation modeling seems to offer a key to disclose new perspective for the long-range infrasound monitoring, nowadays the acoustic records produced by density current events are still primary used for detection and location purposes. In this section we report the analysis of the infrasonic signal produced by large intracrater Askja landslide, occurred on the 21 July 2014, and recorded by an acoustic arrays network in Iceland, about 200 km far. This case-study allow

us to introduce and discuss the issues concerning the long-range propagation of acoustic waves in the atmosphere applied to gravity-current-generated signals. In the next chapters we'll move closer to the source, where atmospheric influence can be neglected, to better investigate the current dynamics.

Results presented in this chapter are extracted from an in-preparation work in collaboration with the Icelandic Meteorological Office (IMO).

2.1 Introduction

The challenge posed by volcano monitoring in order to effectively quantify and assess related hazard concerns not only forecasting issues but also our ability to follow the eruptive style evolution in real-time and to promptly get the volcanic activity changes during a crisis.

In order to face the challenge volcano observatories are increasingly operating multiparametric networks trying to combine many different techniques including seismic and acoustic observations, ground deformation measurements, satellite images, gas sampling, and others. It has been proved how multiparametric local networks highly enhance the ability to deal with the heterogeneous nature of the volcanic phenomena, from the volcanic flows, such as pyroclastic density currents, lava flows and lahars, up to the atmospheric dispersion of a large amount of volcanic ash [12]. In detecting volcanic plumes, able to spread ashes from local to global distances, more than about others volcanic risks an early warning can be crucial for flight safety and for air traffic management. Recent studies have demonstrated how infrasonic waves, and in particular local and regional installations of infrasonic arrays in volcanic areas, can be used to detect, locate and characterize eruptive sequences, and to send an early warning notification of potential ash dispersal in the atmosphere.

Unlike seismology, infrasound generated by the explosive release of fluid into the atmosphere during volcanic eruptions, is closely related to the magma fragmentation and volume outflow dynamics, thus making it a robust indicator of eruption occurrence and able to rapidly evidence variations of the explosive activity [12]. Any phenomenon well coupled with the atmosphere

and able to produce a rapid air displacement when it occurs potentially radiates infrasound. This is the case of natural events such as geophysical flows as pyroclastic density currents, snow avalanches and debris flows, huge landslide, glacier calving and collapses, severe weather conditions and so on. Infrasound technology can be thus efficiently used to monitor a wide spectrum of extreme event and ongoing study focused primarily on early detection and source localization of such events are promising [1].

Incorporated in multiparametric networks infrasound complements other monitoring technologies. In particular an integrated analysis of the infrasonic and seismic signal may effectively enhance monitoring capabilities and hazard assessment related to geophysical phenomena occurring at the ground-atmosphere interface, robustly detecting and characterizing surface activity [13].

In spite its potential for volcanic and environmental monitoring, infrasound technology is relatively new and still at the beginning of its development, thus observatories and facilities implementing infrasound for operative purposes are not so common. In 2013, within the framework of the FUTUREVOLC European project, an infrasound arrays network, mainly focused on volcano monitoring, has been integrated within the national Icelandic monitoring network operated by the Icelandic Meteorological Office (IMO).

The July 21st, 2014 a huge landslide occurred at Askja volcano was recorded by the Icelandic monitoring network. The landslide had a complex evolution triggering a large tsunami into the almost 4 km width crater lake. Landslides are common processes at active volcanoes and represent a major source of hazard for people and infrastructures. Due to the flank instability of the volcanic edifices or volcanic domes, landslides at active volcanoes can trigger major eruptions, as during the 1980 eruption of Mount St. Helens [14], or produce tsunami waves, when the material enters the seawater or the volcanic lakes.

A proper hazard assessment for volcanic landslides requires identification of the event occurrence and estimation of the collapsed volume. This is generally obtained a-posteriori from topographic/bathymetric analysis of the collapse or might be obtained from the modelling of the long-period

seismic wave radiated, were the landslide source is represented by a simple single horizontal single force mechanism [15], or as a simple scheme of accelerating and decelerating mass moving down a slope [16, 17].

Landslide and tsunami events while generating seismic waves in the ground are also able to generate infrasound waves propagating in the atmosphere, as the non-stationary movement of a solid body in air causes air compression/rarefaction that propagates as sound wave. Large volume landslides can produce infrasound able to propagate hundreds of km and detectable at regional distances. On September, 14th, 2005 a massive (~ 50 million of m^3) ice and rock landslide on Mount Steller was recorded at a distance of 540 km from the I53US infrasound array of the CTBTO IMS monitoring network. The infrasound signal was recorded with a peak to peak amplitude of 1 Pa and three wave packets for a total duration of approximately 10 minutes produced as a consequence of multiple propagation paths in the atmosphere. Similarly, on April 2013 a massive landslide (55 Million m^3) at Bingham Canyon copper mine, in Utah produced infrasound which was recorded by 5 infrasound arrays at distances up to 400 km [18].

We present the analysis of the Askja landslide event as recorded by the first infrasound array network installed in Iceland. We provide a detailed description of the long-range detection of this extreme event, modeling the acoustic waves propagation and accounting for wind effects and atmospheric specification along the whole section from the source to the different arrays.

2.2 Infrasound Monitoring in Iceland

Infrasound monitoring in Iceland was started recently with a first small-aperture infrasound array installed during the 2010 eruption of volcano Eyjafjallajökull [19]. Since then three additional infrasound arrays have been installed in the country in the framework of the FUTUREVOLC FP7 European project, which aims at improving volcano monitoring in Iceland for volcanic risk mitigation in Europe, figure 2.1. The four infrasound arrays are now included in the national monitoring system with infrasound data transmitted to the Icelandic Meteorological Office in Reykjavik for real-time monitoring and processing.

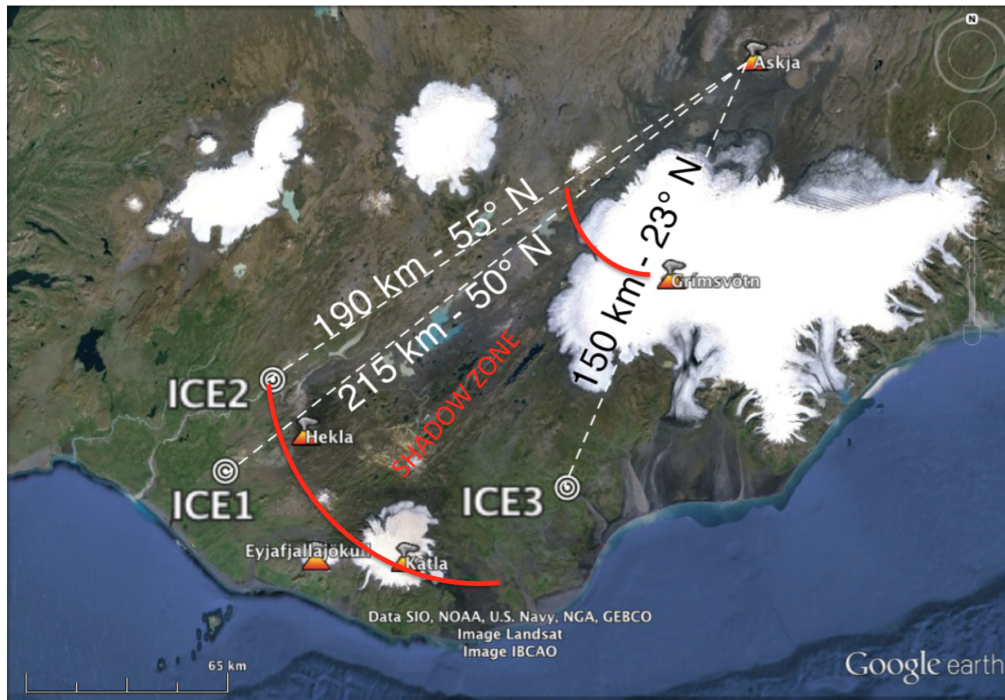


FIGURE 2.1: Map of Iceland showing the position of the 4 small aperture permanent infrasound arrays and of active volcanoes. In red we reported the extension of the shadow zone as modeled.

The infrasound arrays are all equipped with 4 differential pressure transducers deployed typically with a triangular geometry and with maximum aperture of ~ 180 m. Single elements of each arrays are connected by using copper or fibre optic cables to a central digitiser, where data from the 4 channels is collected at 50 Hz and GPS time stamped. The differential pressure transducers have a dynamic range of ~ 70 dB, with a sensitivity of 0.025 mV/Pa in the pressure range of 200 Pa peak-to-peak and are characterized by a noise level of ~ -50 dB relative to $1 \text{ Pa}^2/\text{Hz}$. The sensor frequency response is flat between ~ 0.01 Hz and > 300 Hz, with the Nyquist frequency of 25 Hz representing the upper limit of the system.

The array geometry and aperture were chosen to optimize array response for infrasound with peak frequency between 1 and 3 Hz. The response function of the array as well as the frequency response and dynamic range of the differential pressure transducers are optimal for volcano monitoring at local ($< \text{few tens of km}$) and regional ranges (few hundreds of km) thus allowing monitoring infrasound from volcanic eruption propagating directly to the

receiver or ducted in the stratospheric waveguide.

The arrays position was chosen to improve regional monitoring of active volcanoes especially in the Southern Volcanic Zone and Central Volcanic Zone (Fig. 2.1). Complement the monitoring network with infrasound observations permits discrimination of surface from subsurface seismicity.

This could be extremely useful in Iceland where almost all of the active volcanoes are ice cap covered to have a reliable estimation of the time when the eruptive activity stops to be subglacial contacting the atmosphere. This information about the onset time for possible ash dispersion in atmosphere could be used to constrain input for ash dispersion models and may be used as trigger for other monitoring instrument.

The analysis of the Askja landslide reported in this work gave us the opportunity to evaluate the extension of the shadow zone for propagation of acoustic wave in Iceland that is crucial to evaluate the infrasonic network sensitivity for volcano early warning and to discuss possible improvements.

2.3 Askja landslide event and Infrasound detection

On July 21, 2014 a giant landslide occurred in Askja volcano (65.01° N, -16.75° E), with the rock mass being released south east margin of the inner caldera triggering a large tsunami into the lake [20]. The Askja caldera formed following the 1875 eruption and is now hosting a lake with diameter of approximately 4 km and depth of ~ 200 m. The tsunami wave inundated the shores all around the lake, reaching up to 40 m elevation above the lake level. Seismic waves produced by the landslide were recorded by the whole seismic network in Iceland and allowed to evaluate the onset time around 23:24 UTC. The release area of the landslide was approximately 800 m wide and was approximately 350 m above the crater lake. A total volume of the landslide between 20 and 50 million m^3 was estimated from field survey. Whether or not a volcanic eruption occurred is still debated as well as the possible relation with the landslide. No visual observation of the event is available and event reconstruction is based only on field survey of the effects as well as on distal geophysical records.

Infrasound from the Askja landslide was recorded at the ICE1 array, figure 2.2, deployed at a source to receiver distance of ~ 210 km from Askja volcano. The event was recorded as a long-lasting infrasound wave packet with a duration of approximately 200 seconds, between 23:36:30 and 23:39:00, with stable back-azimuth of 51° N, pointing directly to Askja volcano, and an apparent velocity of sound wave propagation within the array of ~ 350 m/s. Late coherent signal is detected about 1 minute later around 23:40 UTC.

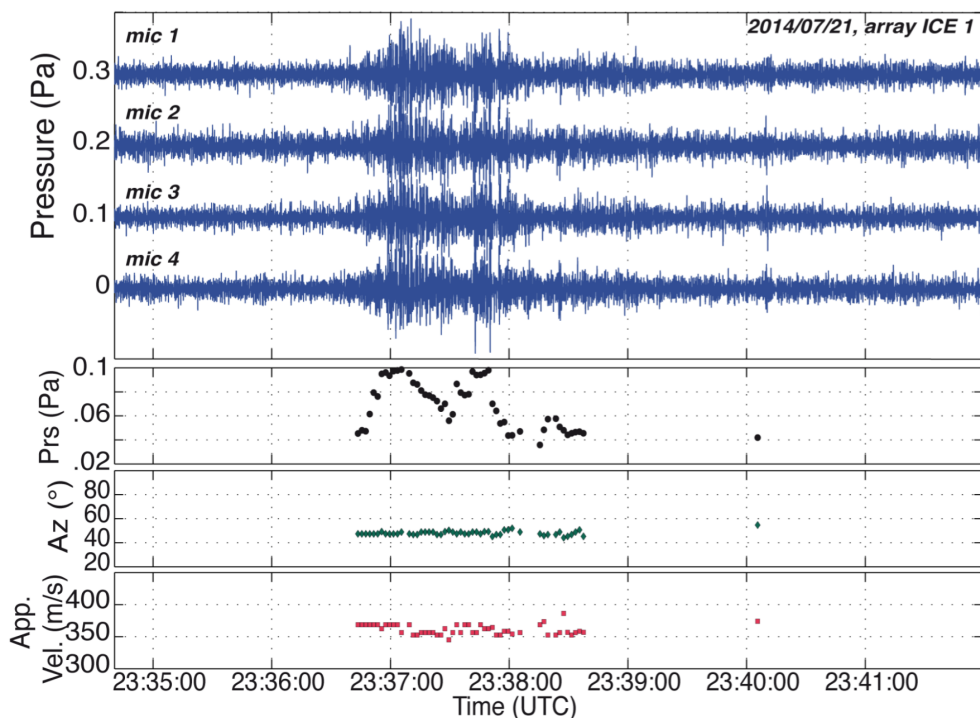


FIGURE 2.2: *Infrasound record (top) of the 4 elements of the ICE1 array, installed in southern Iceland, at a source to receiver distance of ~ 220 km from Askja volcano. Results of infrasound array processing (bottom) showing peak pressure back-azimuth and apparent velocity of all infrasound detections.*

2.4 Modelling of in the infrasonic propagation

Infrasound signal radiated from Askja landslide was not recorded by ICE2 array (at ~ 190 km from the source) and by ICE3 array (at ~ 130 km from the source) while it was clearly recorded at ICE1 array, the farthest station

positioned at a source-to-receiver distance of 210 km from Askja volcano, figure 2.2. Infrasound long-range propagation is determined by the temperature and wind structure of the atmosphere. In order to account for acoustic waves propagation effects we considered atmospheric wind, temperature and density from the ground up to an elevation of 70 km by interpolating ECMWF High-Resolution atmospheric model (HRES) analysis at 91 mean pressure levels up to 0.01 hPa (L91) for the time of occurrence of the event and for the whole area of analysis with a spatial resolution of 0.1 degree in latitude and longitude. Figure 2.3 shows the vertical atmospheric specification above Askja volcano at the time of occurrence of the event obtained from ECMWF HRES analysis. It shows wind inversion between the tropopause and the stratopause, which results into an increased effective sound speed, which is the adiabatic sound speed summed to the longitudinal wind vector, thus enhancing stratospheric ducted arrival. The effective sound speed was calculated for propagation directions consistent with the 3 infrasound arrays.

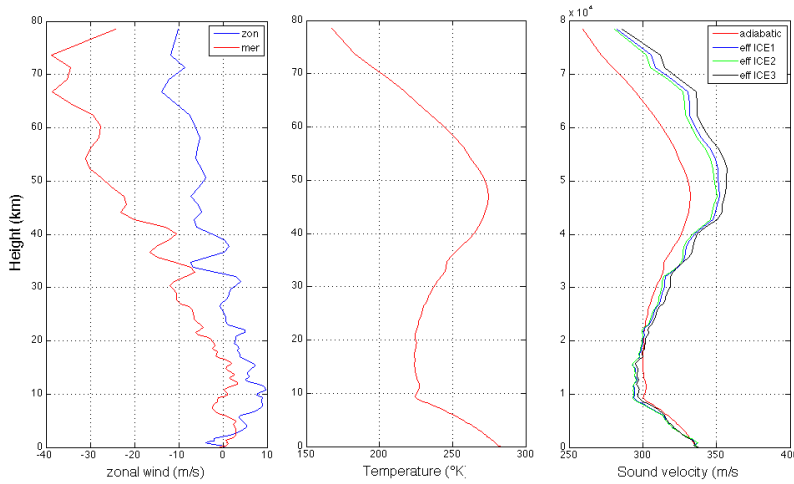


FIGURE 2.3: ECMWF atmospheric specification above Askja volcano as a function of height at the time of occurrence of the event. Zonal and meridional winds, atmospheric temperature, adiabatic and effective sound speed.

Ray-tracing simulation is performed assuming a source at the ground surface and launching 200 rays equally spaced between 0 and 40°. For ICE1 array (215 km at 233° N) simulations predict stratospheric arrivals for rays propagating up to a maximum altitude of ~ 42 km and refracted down to

the ground at a minimum source-to-receiver distance for ~ 210 km. A propagation time of 741 seconds is predicted corresponding to a mean celerity of 293 m/s. For ICE2 array (180 km at 238° N) the first stratospheric arrivals are expected at larger source-to-receiver distances (220 km), resulting in the array being within the shadow zone of infrasound propagation. Also ICE3 array (145 km at 205° N) results within the shadow zone of infrasound propagation being the first stratospheric arrival predicted at a source to receive distance of 208 km.

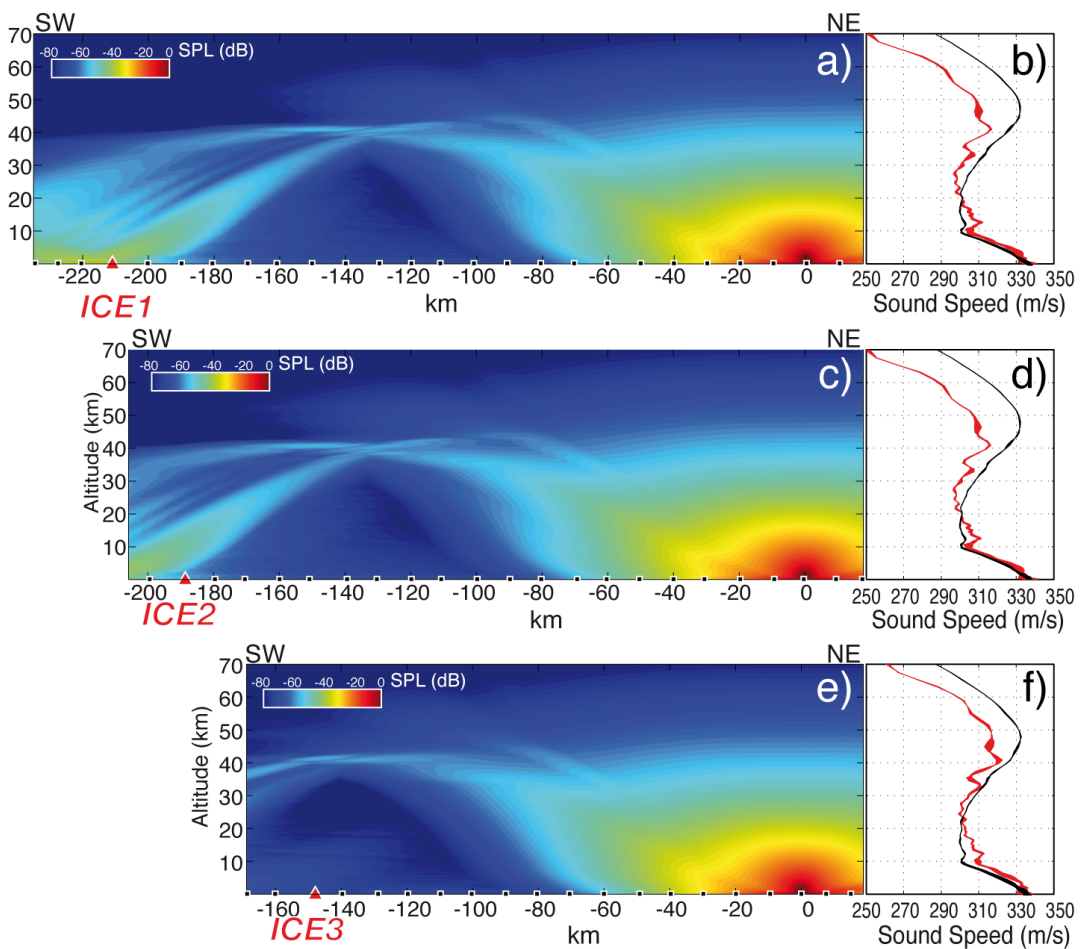


FIGURE 2.4: Sound pressure level maps for infrasonic waves radiated from a source located at Askja volcano and propagating towards the three infrasound arrays.

The infrasound signal from the Askja landslide was recorded only at ICE1 array, being ICE2 and ICE3 arrays positioned in the shadow zone for

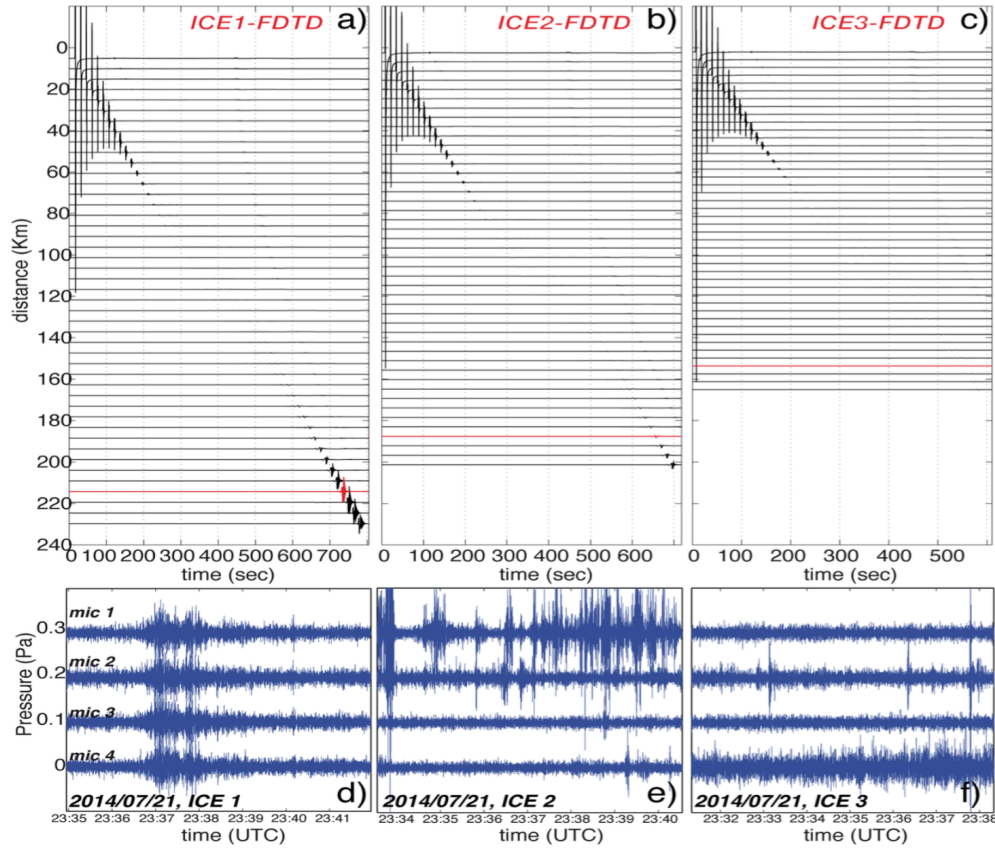


FIGURE 2.5: Synthetic waveforms evaluated with 2D FDTD modelling as a function of distance and real ECMWF atmospheric specifications.

infrasound propagation. The predicted propagation time of 741 seconds allows to estimate an onset time of the event at 23:24:15 being the first infrasound detection at the array at 23:36:36 UT. This is in quite a good agreement with the onset time inferred from seismic observations. The seismic waves produced by the landslide were recorded by the whole seismic network in Iceland and allowed to evaluate the onset time around 23:24 UTC.

Additionally, we performed 2D FDTD modelling of the pressure wave propagation in the atmosphere [21, 22], in order to account for wind effects and atmospheric specification along the whole section from the source to the different arrays. Sound pressure level maps figure 2.4 evaluated for infrasound propagation towards the different arrays confirm ray-tracing simulation with signal detection expected at ICE1 array (-30 dB) but not at ICE2 (-50 dB) and ICE3 (< -60 dB) arrays. The extension of the shadow zones is

confirmed too.

A Gaussian-shaped pulse with a frequency of 0.2 Hz was used as the source time function for the 2D FDTD modeling and a lattice grid size of 25 m was applied with a time discretization of 0.0156 seconds, which satisfies the stability conditions of the FDTD. Here, the travel-time to the array and infrasonic synthetic waveform is calculated as a function of distance every 5 km along each section, figure 2.5. A travel time of 740 seconds is evaluated for the stratospheric arrival at ICE1 array. This is in very good agreement with the travel-time evaluated from ray-tracing and agrees with the onset time of the event.

Chapter 3

Geophysical observations: Dome collapse activity and PDCs production

Contents

3.1 Geophysical analysis of the collapse event and the following explosive phase	30
3.1.1 Abstract	30
3.1.2 Introduction	30
3.1.3 Instrumentation and Data Acquisition	32
3.1.4 Geophysical Observation of the Dome Collapse . .	32
3.1.5 Gravitational Dome Instability and the Materials Failure Law	35
3.1.6 Atmospheric Gravity Waves of PDC	37
3.1.7 Eruptive Source Parameters of Vulcanian Explosion	38
3.1.8 Discussion and Conclusions	41
3.2 Snow and Rock avalanche events	42

This chapter is composed by two sections. In the first section we present geophysical observations referred to the powerful PDCs activity during the 11 February 2010 dome collapse event, at Soufrière Hills Volcano, Montserrat. The second section is a brief comparison with infrasonic signals produced from turbulent density currents, in non-volcanic environments, such

as snow and rock avalanches, as recorded by the LGS-UNIFI instrumentation. The analysis of these valuable data-sets, which allow us to infer possible relations between the main features of the infrasonic signals and flow dynamics, is the starting point for the deeper investigation conducted via numerical modeling in chapter five.

3.1 Geophysical analysis of the collapse event and the following explosive phase

[Published as:] Barfucci G. and Ripepe, M. (2018). Dome collapse interaction with the atmosphere. *Geophysical Research Letters*, 45, 8923–8930. doi: 10.1029/2018GL078243

3.1.1 Abstract

Dome collapse is a dramatic volcanic process which dynamics evolution still presents open questions. Observational data are rare and this limits our ability to interpret the evolution of this phenomenon in terms of risk assessment. We show how the partial dome collapse of Soufrière Hills Volcano on 2010 evolved in less than 45 minutes and was characterized by five main different episode of dome failure process. Time and amplitude of seismic and infrasonic records associated with successive pyroclastic density currents show a nearly quadratic temporal trend suggesting a self-accelerating process increasing in intensity up to the failure limit. Each episode generated gravity waves in the atmosphere, representing the first evidence of internal waves formed due to propagation of density currents in stratified fluids. Finally, we use gravity waves to estimate the total erupted mass and the plume height of the Vulcanian explosions triggered by the decompression induced by the collapse.

3.1.2 Introduction

Dome collapse episodes involve the mobilization of a great amount of juvenile material, due to gravitational instability or internal excess pressure

within the dome itself. A dome collapse is always associated with pyroclastic density currents (PDCs) that move down the flanks of the volcano posing serious risks to local population. The large amount of ash dispersed in the atmosphere during the propagation of the PDC make direct visual observations of the collapse dynamics quite rare and, to date, poorly understood. Our ability to promptly assess the risk relies entirely on the correct interpretation of the data collected during the collapse and on our ability to understand whether or not the collapse is mainly driven by gravitational instability of dome faces or triggered by the increase of the internal magma pressurization [23]. Unfortunately there are not many multiparametric networks which have recorded signals from dome collapse events. The initial phase of most of the dome collapse is generally associated to intense seismicity, which is mainly related to large rockfalls and PDC activity [24]. Frequency content of seismic waves excited by this initial phase was, at Unzen volcano, explained in terms of different stages in PDC formation [25]. Sequential dome collapses at Merapi volcano show an interesting relation between seismic-amplitude envelopes area with the collapsing volumes [26]. This large movement of mass along the steep slopes of the volcano generates also infrasound (e.g. [9, 27, 28]) which has proved to be effective in detecting and tracking the evolution of PDC run out in real time [29, 11]. Nevertheless, a detailed analysis of the infrasonic signal related to sustained PDCs production and dome collapse episode is still lacking. The 11 February 2010 partial dome collapse at Soufrière Hills Volcano (SHV) was one of the largest since the eruption began in 1995 and produced approximately $5 \times 10^7 \text{ m}^3$ of collapsed material from a total dome volume of $\sim 25 \times 10^7 \text{ m}^3$ [30]. The collapse occurred after a period of rapid lava extrusion and dome growth during January and February 2010, that generated block-and-ash flows, PDC events and a series of five Vulcanian explosions [31]. The 11 February collapse event produced pyroclastic flows and high-energy surges followed by a strong Vulcanian explosive phase with a plume reaching $\sim 12 \text{ km}$ of elevation [30]. Here, we present a detailed analysis of infrasonic and seismic records, which when integrated with images of the thermal camera, show how this dataset can be used to derive the evolution of the dome collapse. Infrasound and seismic amplitude grow with time following a

quadratic trend, which nicely fits the material failure law and allows forecasting the final stage of the collapse. Infrasound shows how the interaction between dome collapse and atmosphere generates an unprecedented record of gravity waves induced by PDCs activity. In addition, gravity waves are also clearly associated with the Vulcanian eruption and can be modeled to evaluate the total amount of volcanic ash injected into the atmosphere.

3.1.3 Instrumentation and Data Acquisition

The 11 February 2010 dome collapse at SHV has been recorded by seismic, infrasonic stations and thermal camera installed in cooperation with the Montserrat Volcano Observatory (MVO). A GURALP CMG-40T broadband, three component seismometer, with eigenperiod of 30 s, was located at St. George's Hill (SGH) site at about 3 km from the active dome. The thermal camera and the infrasonic sensor were co-located at the Montserrat Volcano Observatory (MVO) at a distance of approximately 5.6 km from SHV. The camera is a FLIR A20 model equipped with $34^\circ \times 25^\circ$ optical lens of 9.2 mm and a maximum thermal resolution of 0.1°C in the $7.5 - 13 \mu\text{m}$ wavelength interval. The camera field of view (FOV) above SHV is approximately 3.5×2.5 km. The infrasonic sensor is a PRS100 (by iTEM) differential pressure transducer, with a sensitivity of 10 mV/Pa at 1 Hz, 250 Pa of full-scale range, a flat instrument response in the frequency band of 0.01 – 100 Hz, and a background noise level of 10–2 Pa. Seismic and infrasonic records have been corrected for each instrument response function.

3.1.4 Geophysical Observation of the Dome Collapse

The activity of Soufrière Hills Volcano on Montserrat, in the West Indies, is characterized by dome building phases of lava extrusion and episodes of partial or total dome collapses interspersed by Vulcanian explosions. Such explosive phases typically result from sudden decompression of the shallow magmatic system due to the lava dome disruption. Seismic and infrasonic stations on February 11, 2010 at 16:50 GMT recorded the beginning of a period of intense activity. Thermal imagery indicates that this activity coincides with a sequence of pyroclastic flows that released large quantities of ash in the atmosphere quickly covering the whole field of view (Figure

3.1). Thermal radiation, calculated by the integration of the temperature measured in the camera field of view (FOV) of each single frame, shows at 16:55 GMT a decay in the thermal intensity (Figure 3.1,a). This thermal decay marks the beginning of a relative “cold” period, which follows the onset of the seismic and acoustic activity and is evidence of the beginning of an intense PDC phase. The quantity of ash dispersed in the atmosphere was large enough to make difficult the visual observation of the dome thus shielding the hot volcanic dome and reducing the total temperature in the camera field of view. During this “cold” thermal period seismic and acoustic signals are characterized by comparable cigar-shape waveforms with the gradual increase-decrease of the amplitude (Figure 3.1 d, e). The similarity between seismic and infrasonic waveforms is compatible with a source moving at the interface between the ground and the atmosphere typical of mass movements such as density currents [32, 29]. Despite the strong similarity in the waveforms, seismic and infrasonic signals have a different frequency content, whereas seismic signal shows a broad frequency content above 0.1 Hz, infrasound shows a remarkably wide spectrum ranging from 1 mHz up to a few hertz (Figure 3.2,b). However, above 0.1 Hz, seismic signal reaches the maximum amplitude at around 1-4 Hz, typical of PDC [25, 32] whereas infrasound is characterized by a much lower frequency content around 0.4 Hz. In spite of the similar cigar-shape waveform, this different frequency content indicates that the energy during the propagation of the PDCs is differently partitioned. While seismic waves are driven by the friction of the sliding source with the ground, infrasound is associated to the displacement of the atmosphere during the movement. This activity indicate that the gravitational process of the unstable dome collapse is characterized by a sequence of at least five major PDC episodes with peak amplitude at 16:56, 17:06, 17:10, 17:14, 17:16 GMT. At the end of this period, at 17:20:15, strong impulsive signals in the seismic and acoustic record coincide with two high temperature impulses in thermal radiation (Figure 3.1), and mark the onset of two large Vulcanian explosions. At 17:35:00, only 45 minute after the beginning of a dome collapse, all the geophysical parameters drop back to a pre-activity level marking the end of the dome collapse.

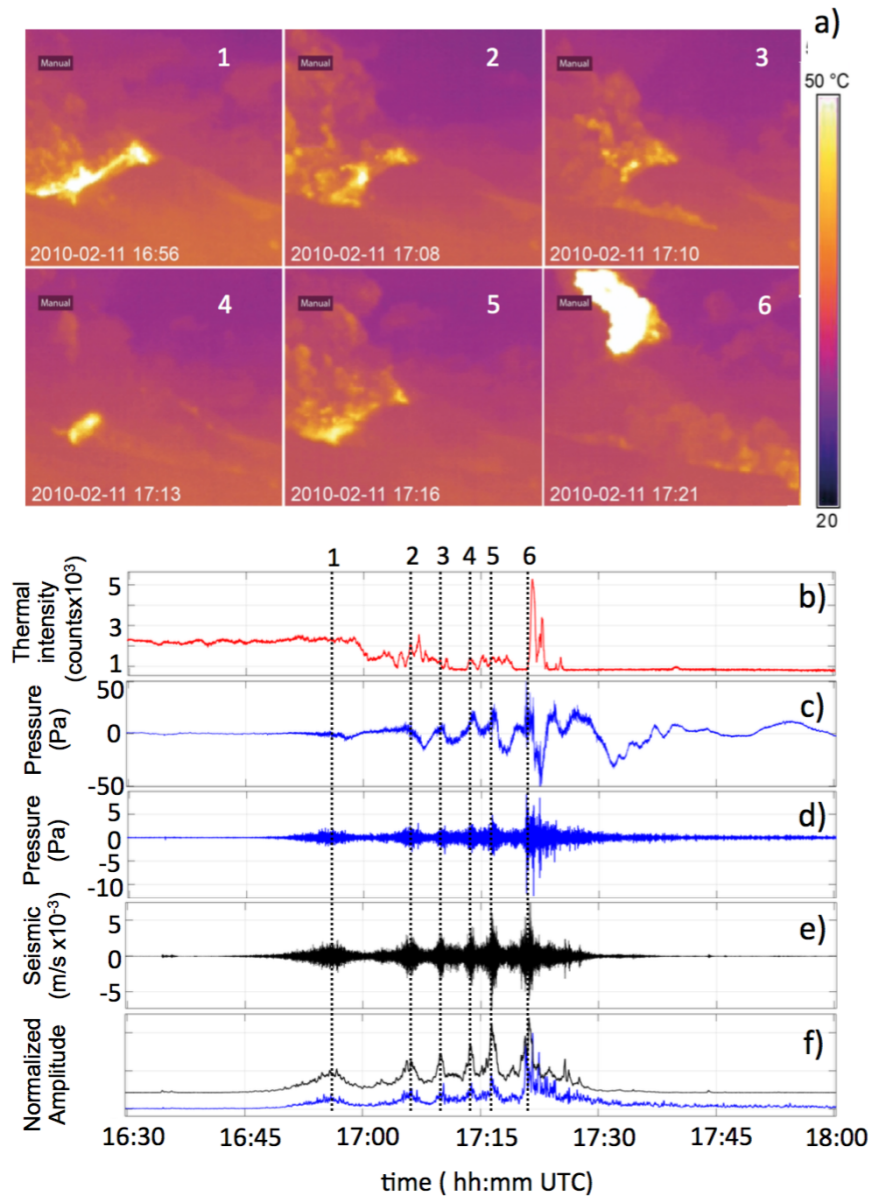


FIGURE 3.1: Synoptic view of the geophysical dataset collected during the dome collapse. (a) Frames showing the six different phases of the collapse; (b) number of pixels above the temperature threshold of 30° is used as proxy of the frame-by-frame thermal intensity detected in the camera field of view; (c) acoustic record raw and (d) high-pass filtered 0.1 Hz; (e) seismic ground velocity and (f) envelope of seismic (black) and infrasonic (blue) amplitude. Infrasonic and seismic signals show five major steps of the collapse. These steps (from 1 to 5) correspond to the PDC episodes, with seismic and infrasonic increasing amplitude with time. The last step (6) indicates the onset of the vulcanian explosions occurred at 17:20:15 GMT at the end of the dome collapse.

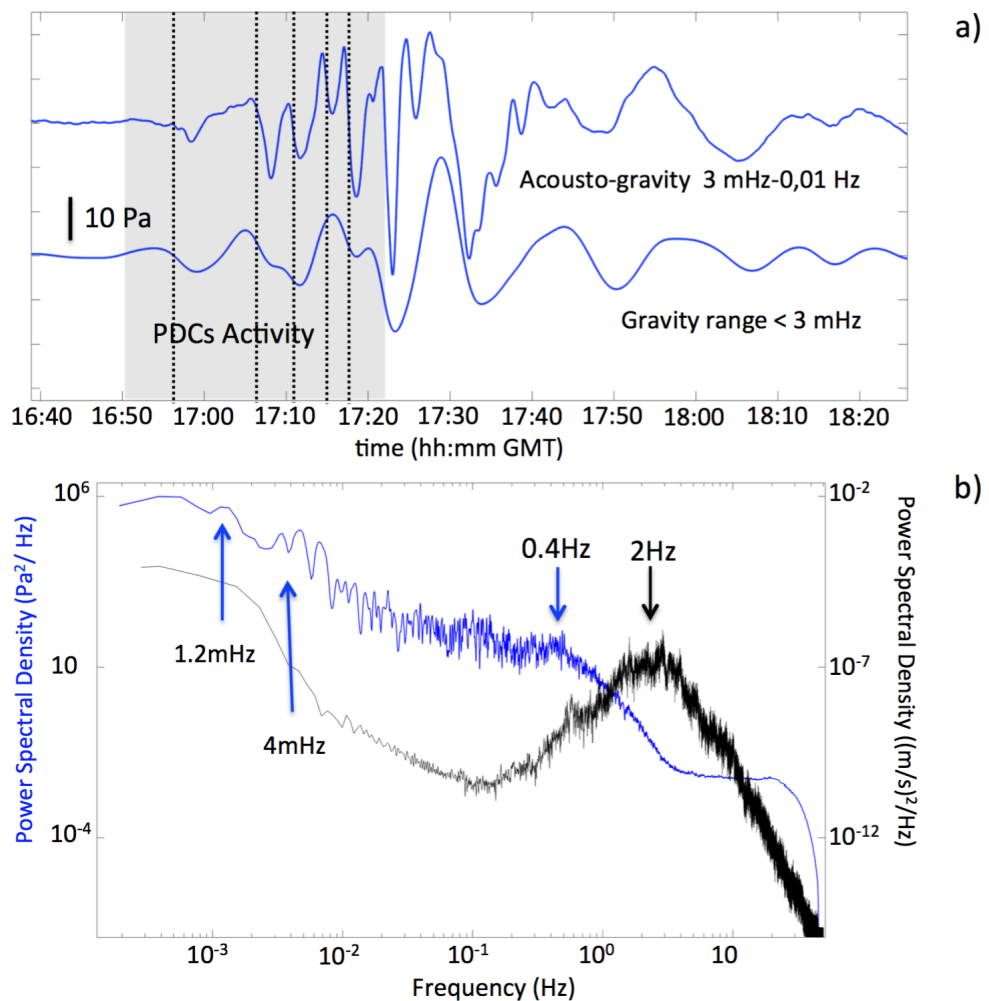


FIGURE 3.2: (a) Acoustic record once corrected for the instrument response function is filtered (up) in the acousto-gravity range between 3mHz and 0.01 Hz and is low-pass filtered (down) in the gravity waves band below 3 mHz. Dashed lines indicate the occurrence of the five PDC episodes of Figure 1; (b) Power Density Spectra of seismic (black line) and infrasonic (blue line) signals show that the energy released during the PDC events is differently partitioned between seismic and acoustic waves.

3.1.5 Gravitational Dome Instability and the Materials Failure Law

Signal amplitude associated with the five PDC episodes increases with time (Figure 3.1 and 3.3), both in the infrasound (from 2.5 to 8 Pa recorded at 5.6 km from the source and high-pass filtered > 0.1 Hz) and in the seismic

(from 2×10^3 to 5.7×10^3 m/s). These indicate that the collapse evolved through 5 major steps of incrementally larger episodes of flank instability (Figure 3.1) over a period of half an hour (from 16:50 to 17:20). While the duration of each event decreases from ± 300 s to ± 60 s, the rate of occurrence is increasing with time (Figure 3.3). This pattern in amplitude and PDCs rate suggests a self-accelerating process that increases in intensity up to a critical point (Figure 3.3). Similar behavior has been originally observed with regard to materials in terminal stages of failure [33] and it was then successfully extended also to the eruption processes at volcanoes as an analytical basis for eruption prediction [34]. The empirical relation driving the mechanics of failure reads as:

$$\ddot{\omega} = C\dot{\omega}^\alpha \quad (3.1)$$

where C and α are two empirical constants and ω is the observed geophysical quantity. Concerning eruption processes, behaviour of some of the observable parameters, preceding a volcanic eruption, can be described by this physical law ([34]; [35]). The material failure forecast method has been applied to the observed pattern of seismic energy released before the eruption and to the deformation of the summit at Merapi volcano and it proved to be able to forecast the eruption time with good accuracy [36]. In all these studies, the empirical constant α is found to be frequently nearly 2. Integrating equation 3.2 for $\alpha > 1$ and with boundary condition $\dot{\omega}(t_f) = \dot{\omega}_f$, where t_f is the time of failure (see [34], for details), we derive the following expression for the rate $\dot{\omega}$ of the observed geophysical quantity:

$$\dot{\omega}_i = \left[C(\alpha - 1)(t_f - t_i) + \dot{\omega}_f^{1-\alpha} \right]^{\frac{1}{1-\alpha}} \quad (3.2)$$

which for $\alpha = 2$ becomes:

$$\dot{\omega}_i^{-1} - \dot{\omega}_f^{-1} = C(t_f - t_i) \quad (3.3)$$

where the inverse rate of the observed geophysical quantity $\dot{\omega}^{-1}$ decreases linearly with time. In our case we set $\dot{\omega}_i^{-1} = \frac{T_i - T_{i-1}}{A_i - A_{i-1}}$ as the inverse rate of the amplitude increase of the seismic (Figure 3.3,a) and infrasonic (Figure 3.3,b) signals related to the five PDCs, as predicted by the failure law (equation (3)), the observed trends show an inverse linear rate with time (Figure 3).

In analogy with the failure time of materials, a *critical time* for the observed process can be estimated as the time the inverse rate goes to zero [34]. In our case we estimate that the *critical time*, t_c , will occur between 17:16:24 and 17:16:50, with a best fit of $R^2 = 0.98$ and only ~ 3.5 minutes before the onset of the vulcanian explosion occurred at 17:20:15 (Figure 3.3). Considering 95% confidence intervals, these critical times t_c can have a variability of no more than ± 3 min for both the seismic and infrasonic amplitude variation. The use of the failure law allows evaluating when the dome collapse will end and for how long it will last.

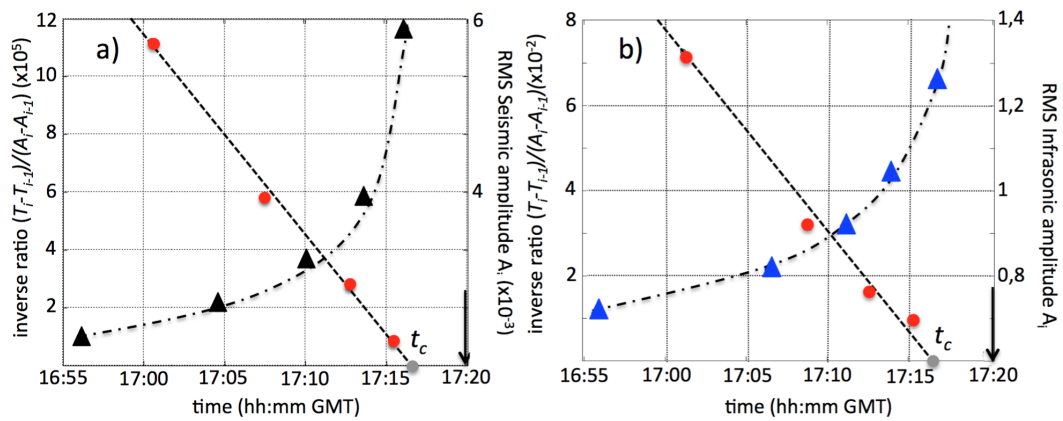


FIGURE 3.3: RMS of (a) seismic and (b) infrasonic amplitude and their inverse rate of the amplitude increase (red circles). Inverse rate of the amplitude is decreasing following a linear fit (dashed line) of, $R^2 = 0.98$, both for the seismic and infrasonic data. The gray dots indicate the critical time, t_c , and the arrows the onset of the vulcanian explosions.

3.1.6 Atmospheric Gravity Waves of PDC

Pressure signals recorded during the dome collapse are characterized by large, long-period, oscillations, visible also in the raw data (Figure 3.1). Spectral analysis reveals these oscillations have broad frequency content, ranging from 0.01 Hz to 1 mHz (Figure 3.2,b). A significant proportion of the acoustic energy is thus concentrated below the typical frequency content of infrasound ($> 0.1\text{Hz}$) and it is breaking the limit (3.0 mHz for a standard atmosphere) of the propagation of acoustic waves. Below the acoustic cut-off frequency, pressure oscillations are dominated by the gravity term, and pressure propagates as gravity wave, while just above, wave propagation is

controlled by the elastic properties of the atmosphere. Acoustic and gravity waves are commonly observed in the ocean where they are decoupled, but both waves can propagate as coupled acousto-gravity waves in the atmosphere [37]. Pressure signal filtered above the cut-off frequency shows oscillations peaking at around 4 mHz frequency content, typical of acousto-gravity waves, which present shared features between pure acoustic waves, dominated by elasticity of the atmosphere, and gravity waves controlled by buoyancy effects. Gravity waves (Figure 3.2,a) become clear by filtering below the cut-off frequency and are characterized by oscillations of increasing amplitude, from 3 to 9 Pa while approaching the explosive phase at 17:20:15. It is worth noting that both acousto-gravity and gravity waves, only appear after the emplacement of the first PDC at 16:50 GMT. Besides, these waves appear well phased with the amplitude modulation of the seismic and infrasonic signal produced by the five PDC episodes (Figure 3.1,c-e). We thus infer that these oscillations may represent the reaction of the atmosphere to the air displacement that each current produces by propagating along the flanks of the volcano. Gravity waves induced by propagation of a density current in a stratified medium have been studied in relation to small-scale laboratory experiment and are predicted by numerical modeling [2]. However, observations, and records, of these waves induced by density currents in nature are to date rare, and this is the first record of gravity waves associated with strong PDCs activity and dome collapse.

3.1.7 Eruptive Source Parameters of Vulcanian Explosion

Thermal camera, seismic and infrasonic records show (Figure 3.1) that gravitational instability of the dome ends at $\sim 17 : 20$ interrupted by a violent Vulcanian explosion. Relative thermal intensity calculated by integrating the camera field of view above the 30°C threshold (Figure 3.1) indicates at least two clear thermal pulses at $17 : 20 : 14$ and $17 : 21 : 40$, lasting 74 and 42 seconds, respectively, which seems associated with two acoustic peaks at 41 and 28 Pa, respectively. Evidence of at least two pulses during the explosive phase were also reported by Cole et al., in 2015, on the base of thermal recordings. The explosive injection of mass and thermal energy into the atmosphere have triggered gravity waves which amplitude increases to

higher values (up to 22 Pa, Figure 3.2,a) with respect to those observed during the PDCs activity (Figure 3.2). In case on volcanic eruptions, duration and frequency content of gravity waves are in general better explained by the addition of mass than of thermal energy in the atmosphere [38]. Therefore, we assume a point source located in the atmosphere above the ground to model gravity waves as the convolution $P(x, t) = \dot{q}(t)h(x, t)$ between the oscillation of the free atmosphere $h(x, t)$ and the first derivative of the mass flow rate $\dot{q}(t)$ [39]. Here, the oscillation of the atmosphere, $h(x, t)$, is calculated as the response of the atmosphere in m^{-1} to the unitary step of the mass flow rate recorded at a distance x from the source [39] and for a given atmospheric profile at the time of the eruption (e.g. [40]). Location of the source represents the elevation at which the transition between the gas thrust (momentum) and the buoyancy regime in the plume dynamics occurs. We assume here that the source time function is described by the exponential source function generally used to represent the mass flow rate, $q(t)$, [41, 39, 40], (Figure 4):

$$q(t) = Q_0 \frac{t}{\tau} \left(1 - \frac{t}{\tau} \right) \quad (3.4)$$

where Q_0 is the maximum mass eruption rate and τ is the rise time of the source in seconds. The best fit of $R^2 = 0.85$ with the observed pressure wave is calculated considering all the possible elevation of the source between the sea level and 9000 m, and a rise time (τ) changing in the $2 \sim 400$ s range (Figure 4). Considering all the solutions with $R^2 > 0.8$ the source is located at an elevation of 4650 ± 300 m a.s.l., has a rise time, τ , of 21.6 ± 0.9 s a, (Figure 4c) and a total duration of the mass pulse of ~ 120 s, which is in agreement with the duration of ~ 130 seconds of the two thermal pulses (~ 80 and ~ 50 seconds each). Our modeling shows that amplitude of the gravity waves is compatible with a maximum mass eruption rate Q_0 of $1.2 \pm 0.3 \times 10^8$ kg/s, which integrated over the source time function gives a total erupted mass of $5.7 \pm 0.5 \times 10^9$ kg. Total erupted mass can be converted into plume height, using the relationship for the Earth's standard atmosphere $H = 0.042M^{\frac{1}{4}}$ where M is the total mass of solids and gas ejected and H is the plume height in kilometers which in our case is 11.5 ± 0.3 km. Gravity waves generated during the five PDCs episodes probably were still exciting oscillations in the

atmosphere when vulcanian explosion occurred. This means that the gravity waves we modeled could have been contaminated by oscillation of the atmosphere started before the explosive onset. The two gravity wavefields, before and after the explosion (Figure 4a), have very similar frequency content and thus the contribution of the PDC-induced gravity waves can not be easily separated from the vulcanian-related ones, with non quantified effects on our modeling. However, the good fit of $R^2 = 0.85$ between observation and model seems suggesting that if there was a contamination this would have been probably very low.

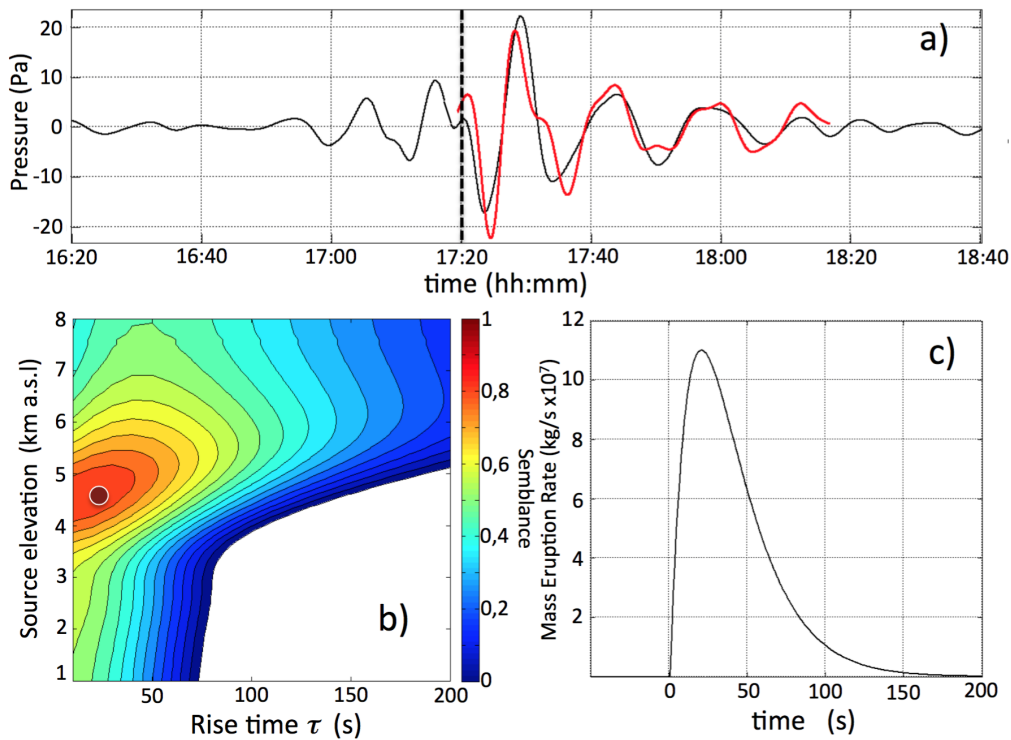


FIGURE 3.4: (a) Gravity waves recorded (black line) and calculated (red line) using the point mass injection source model. Dashed line represents the onset of the Vulcanian explosion and the onset of the modeling. (b) Close up of the semblance map between the measured and the modeled gravity waves for different source elevations and rise times. Red dot indicates the best solution of $R^2 = 0.85$. (c) Mass eruption rate associated with the best fit and relative to the gravity waves (red line) shown in panel (a).

3.1.8 Discussion and Conclusions

Dome collapse is a rare and dramatic event in the dynamic evolution of volcanic activity. In Montserrat the 1995 collapse of the SHV dome had a large impact on the economy and life of the island causing the complete destruction of the capital Plymouth, the commercial harbor and the international airport. Besides the high risk related to the collapse, there are still open questions regarding the evolution of these phenomena also because observational data are still rare. Data presented in this work represent an almost unique geophysical dataset, used here to identify the major steps leading to the collapse of the SHV dome that occurred on February 11, 2010. The collapse was characterized by five large PDC episodes, each of them associated to different steps in the progressive failure of the dome. Waveforms of seismic and infrasonic signals are consistent with a moving source differently coupled with the ground and the atmosphere. We show how while the amplitude of seismic and infrasonic signal is increasing, the temporal separation of the PDCs episodes decreases following a nearly quadratic trend. This is remarkably well-explained by the material failure law ([33]; [42]) indicating that the collapse was controlled by the progressive self-accelerating gravitational instability. More observations might clarify whether and how mechanisms underlying dome collapse may be described by deterministic models. However, our results indicate that seismic and infrasonic amplitude in case of gravitational instability of the dome may follow a well-defined pattern, which can be used to forecast the final stage of the dome collapse. The possibility to estimate the duration of the ongoing collapse would represent an important parameter to evaluate the risk exposure of human lives and/or goods to PDCs activity, with immediate impact on the risk management. Besides, while seismic waves do not show any significant change in the frequency content, infrasound shows that pyroclastic episodes are characterized by a peak frequency content around 0.4 Hz. Frequency content of PDC is lower than what previously observed for PDC activity at SHV (1 – 2 Hz, see [29]). Considering that these events are bigger than those analyzed in 2008 this seem suggesting that a relationship between the frequency of the acoustic signal and the size of the PDC might exist. The large volume of material displaced is responsible for unprecedented observation of gravity

waves ($< 0.003Hz$) and acousto-gravity waves associated with dome failure and/or the large quantity of thermal heat released during the intense pyroclastic flow activity. Our observations indicate for the first time that the PDCs activity is able to perturb the atmosphere inducing gravity waves. Numerical simulation and experimental studies also at smaller scale indicate that internal waves can be formed due to propagation of density currents in stratified ambient ([43]; [44]) and have proved that such waves can heavily affect the kinematic parameters of the current [45]. However observations and records of these waves induced by density currents in natural environments are still rare. Continuous records of such waves may provide new insight on the interaction of gravitational instability phenomenon with the atmosphere and may represent a starting point for future works on density currents propagating in stratified fluids in comparison with experimental studies and computational models. The 30 minutes long gravitational instability steps of the dome collapse has most probably induced a magma decompression responsible for two violent vulcanian explosions reaching ~ 12 km of height. The response of the atmosphere to the injection of the volcanic mass generated one hour long gravity waves. Modeling of these gravity waves ([39]; [40]) is compatible with a point mass injection source located at 4600 *m* a.s.l. lasting 120 seconds. The best misfit between data and model ($R^2 = 0.85$) is achieved for a total DRE ejected mass of $5.7 \pm 0.5 \times 10^9$ kg, which corresponds to a plume height of 11.5 km. At the end, the total duration of the collapse lasted 45 minutes inducing decompression on the magmatic system only after 30 minutes and generating gravity perturbation in the atmosphere.

3.2 Snow and Rock avalanche events

In the paper reported in the Section above, we show how acoustic and seismic signals can be used to obtain important information to study the pyroclastic flows activity during a dome collapse event followed by a Vulcanian explosive phase.

In order to go further and reach new insight on the interpretation of acoustic signal related to the PDC dynamics, we focus our attention on the

inferred relation between the acoustic signal frequency and the estimated size of the flow.

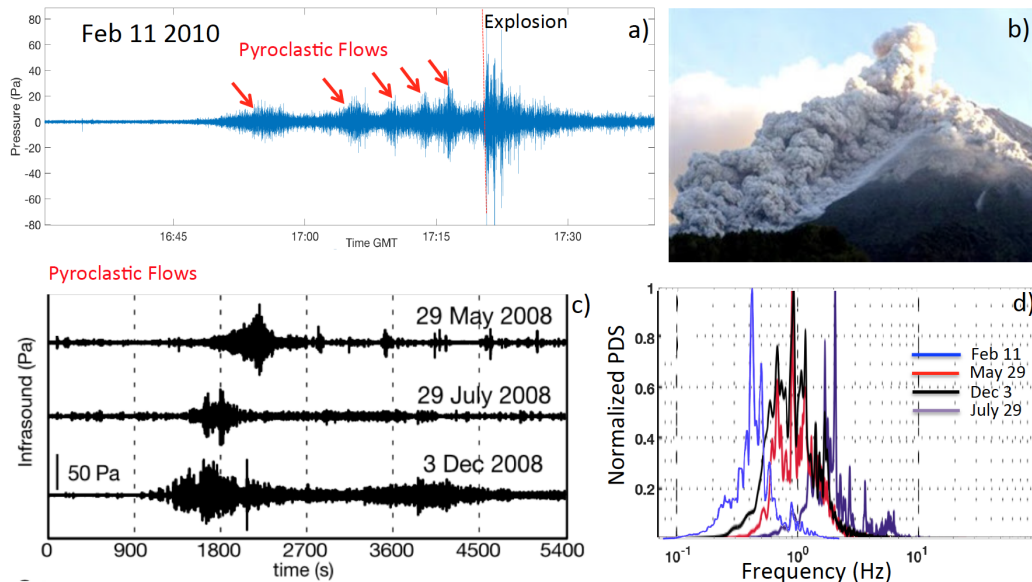


FIGURE 3.5: (a) Infrasonic record of the 11 February 2010 dome collapse event. We can see five main episodes of PDCs followed by a large Vulcanian explosion. (c) PDC events reported in Ripepe et al., 2010. (d) corresponding spectra.

Starting from the field observations of PDCs activity at Soufrière Hills volcano, in Montserrat, we extend our analysis to infrasonic signals produced by different types of gravity current events, such as snow and rock avalanches. As discussed in the introduction all these turbulent multiphase flows share similar dynamics. Data were provided by the laboratory of experimental geophysics (LGS) of the University of Florence.

Among all the recorded events we select those for which field estimation of the deposited volume of materials was available, providing a small dataset of six events.

Given the difficulty to find quantitative field observations for events associated to the available infrasonic records, we include in the dataset also events for which only a rough volumes estimation was available, reporting such data as order of magnitude. In consequence of this errors can be large.

In addition to the observations of PDCs events at Soufrière Hills Volcano reported by [29] and by [13] (see also [31], [46] for field observations), our

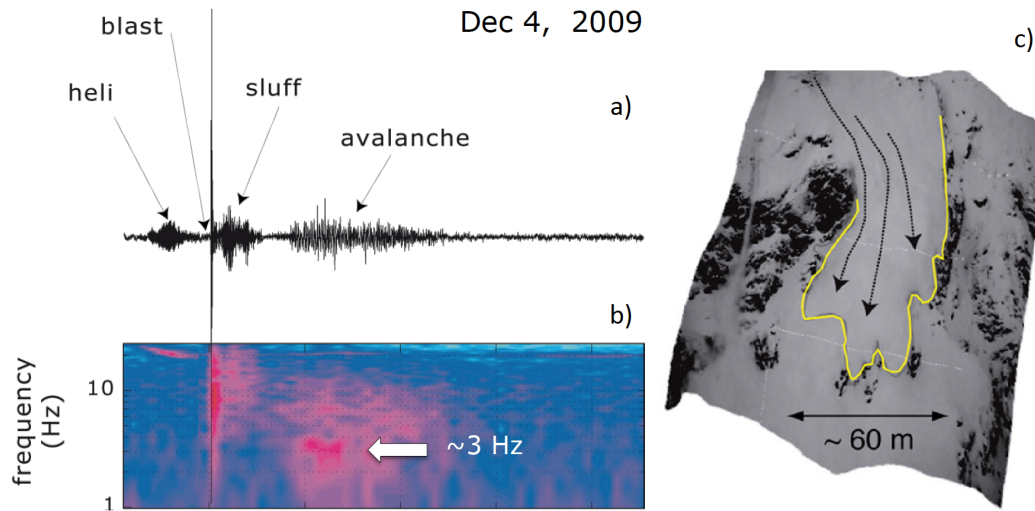


FIGURE 3.6: (a) Infrasonic record of the small to medium sized snow avalanche recorded in Gressoney. (b) Spectrogram of the infrasonic signal. (c) Deposits related to the avalanche event.

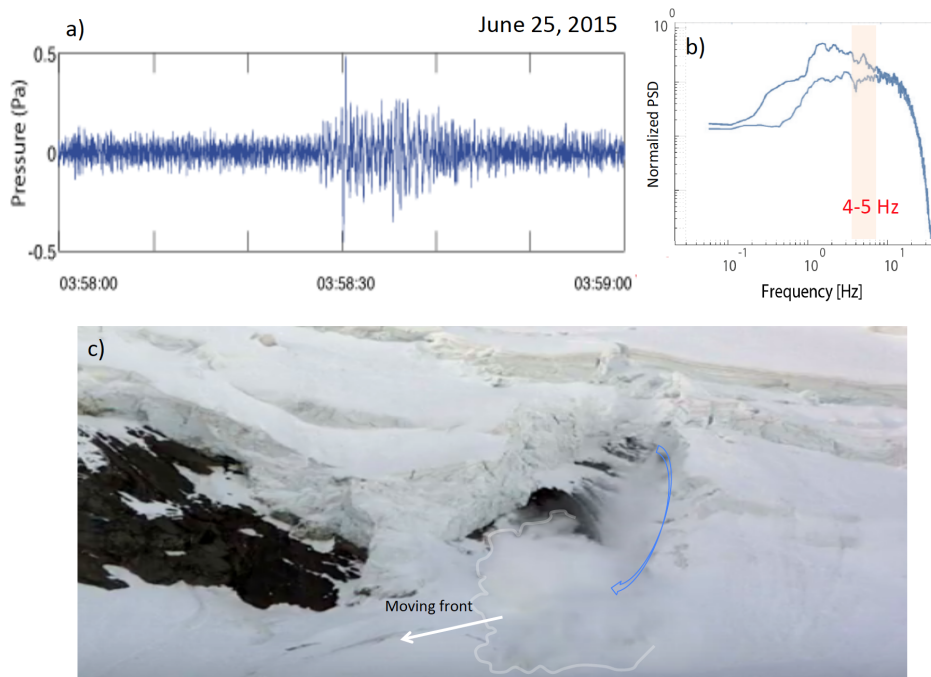


FIGURE 3.7: (a-b) Infrasonic record and related spectral content associated to the small break-off even at the glacierized northwest face of Weissmies in the Saas valley (Switzerland). (c) Visual observation.

dataset comprises infrasonic signals produced by a large rock avalanche, one small-to-medium size snow avalanche and a small ice fall event.

The huge collapse of the north-east face of Pizzo Cengalo occurred on 23 August 2017, involved about 4 million cubic meters of rock detached from 3000 m of altitude originating a large rock and debris avalanche. Three different infrasonic arrays (installed by LGS to study and monitoring snow avalanches activity) recorded this event at large distance (~ 150 km) from the source.

The snow avalanche event was classified as small to medium sized (deposited volume between $10^3 - 10^4$ m³) powder avalanche and it was recorded by an infrasonic array located in Gressoney, about 2.2 km distant from the source [47].

A small break-off even at the glacierized northwest face of Weissmies in the Saas valley (Switzerland), was detected during a monitoring campaign (July 2015) exploiting interferometric, Doppler radar, optical imaging and GPS sensors as well as infrasound and seismic arrays [48].

The detached ice volume was estimated to be few thousand of cubic meters and the related infrasonic signal was recorded at 2.5 km from the unstable glacier tongue.

Analysing the infrasonic signals produced by the events listed above, we notice that all the events present the typical spindle-shaped waveform already observed for PDCs event and snow avalanches. In Figure 3.9 we report field observation as estimated solid volumes and the peak frequency of the related infrasonic signals.

From the spectral analysis we consider the main spectral peak as reference values assigning an error proportional to the peak width. Due to the large error affecting the field observation (in some cases only orders of magnitude were available), we assign to each event a range of possible values. We observe how this semi-quantitative relation suggests a dependence of the acoustic signals frequency on the magnitude of the event. Given the difficulty to find joint infrasonic and field observation of natural flows, in Chapter 5 we resort to numerical modeling technique to further explore this dependence.

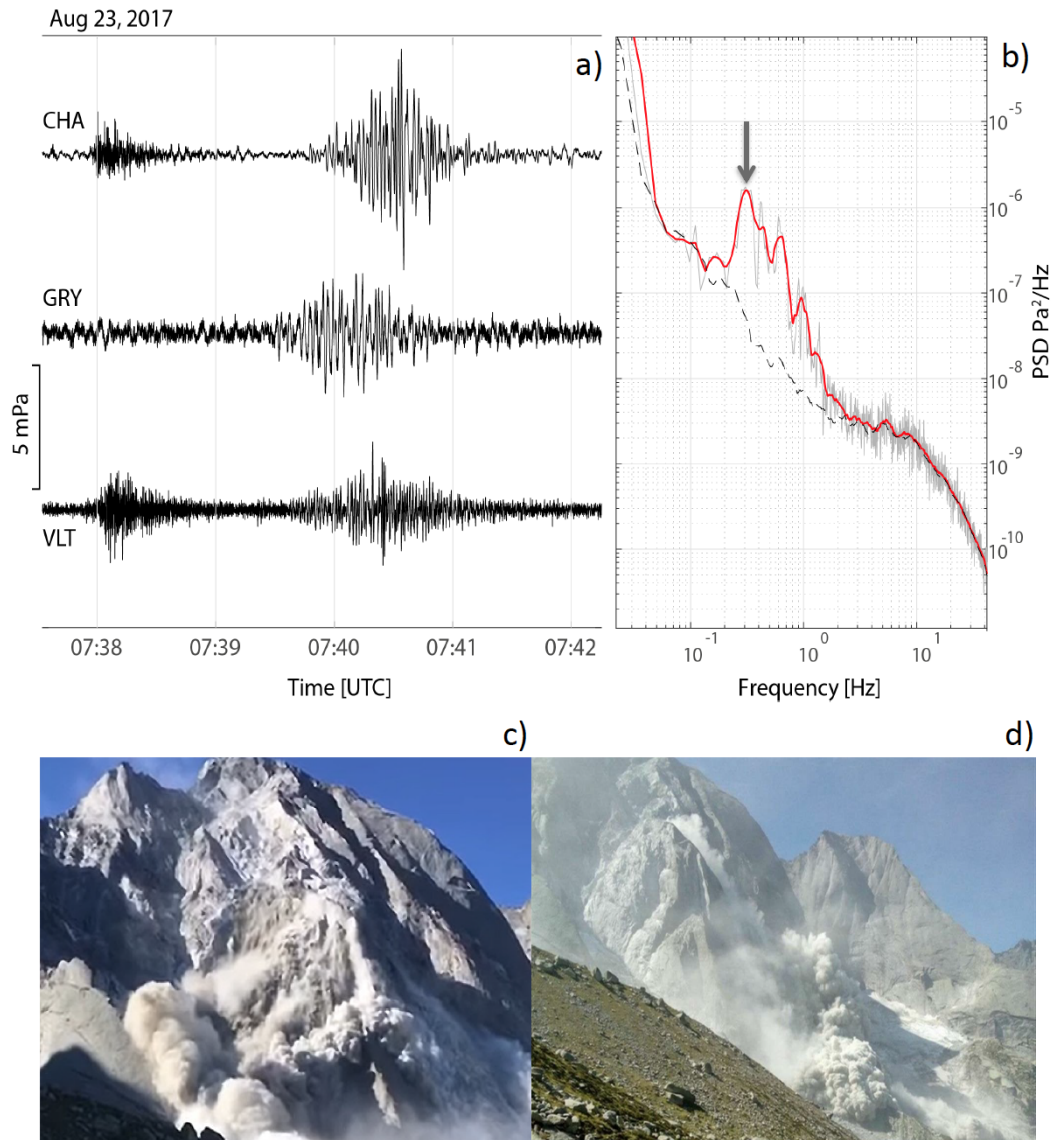


FIGURE 3.8: Avalanche of rock and debris detached from the north-east face of Pizzo Cengalo occurred on 23 August 2017 (c-d). (a) The acoustic signals produced by this event was recorded, at large distance from the source (~ 150 km), by three different infrasonic arrays located at Champoluc, Gressoney and Valtournenche with interdistances of about 10 km. (b) Corresponding spectral content.

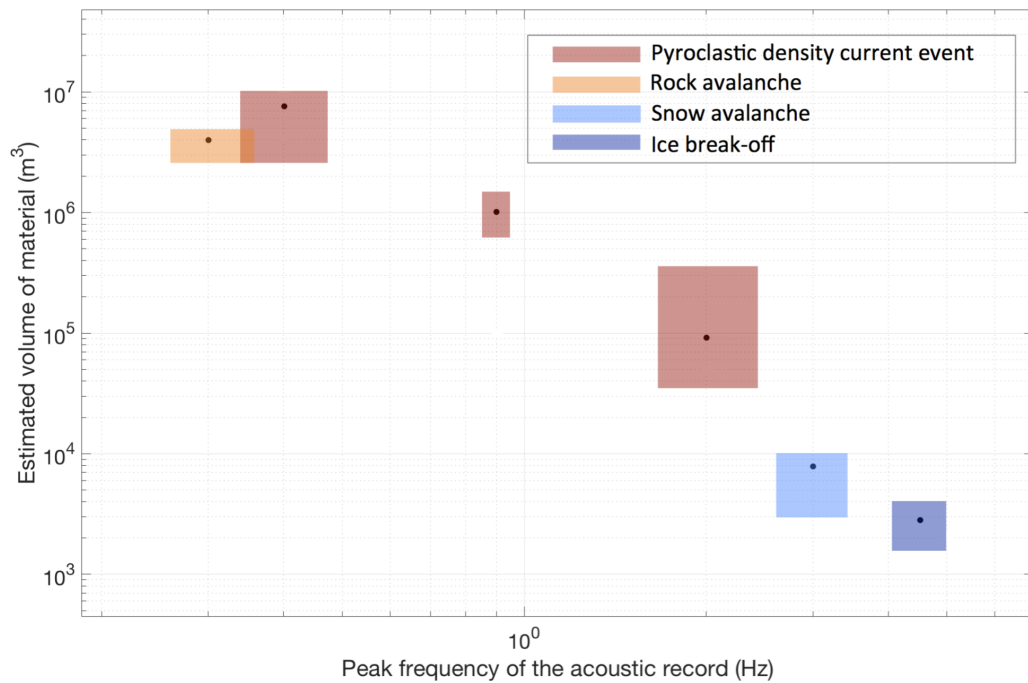


FIGURE 3.9: *Estimated volumes of deposits versus the peak frequency of the recorded acoustic signal for the six analyzed events. A large error on volumes is reported due to the uncertainties affecting available estimations.*

Chapter 4

Geophysical observations: Debris flows activity, the Illgraben case study

Contents

4.1	Abstract	50
4.2	Introduction	51
4.3	Study site	53
4.4	Instrumental setup	54
4.5	Debris flow events	56
4.5.1	Infrasound array analysis of debris-flows	59
4.5.2	Spectral analysis of debris-flows	64
4.6	Discussion	65
4.6.1	Mechanisms of infrasound radiation by debris flow at Illgraben	65
4.6.2	Seismo-acoustic coupling of radiated elastic energy	70
4.6.3	Use of infrasound monitoring as an early warning system for debris-flows	72
4.7	Conclusions	74

The following chapter reports results from the elaboration of infrasound data recorded at Illgraben (CH) site during several debris-flow events. A debris flow is a rapidly moving mass of sediment, large particles, water and air that travels down a slope under the influence of gravity. Due to their

water content, debris-flow dynamics differ significantly from other diluted turbulent flows such as PDCs, which represent the main topic of the thesis. According to the variable water content they show a type of flow behaviour intermediate between dry rock avalanches and water floods.

The comparison of infrasound data produced by these type of events evidences how the differences observed may reflect the differences in flow dynamics.

[Published as:] Marchetti M., Walter F., Barfucci G., Genco R., et al., (2018) Seismo - acoustic observations of debris flow activity and implication for early warning, submitted to Journal of Geophysical Research: Earth Surface, 124. <https://doi.org/10.1029/2018JF004785>

4.1 Abstract

Debris flows constitute a severe natural hazard and studies are performed to investigate triggering mechanisms and to identify and evaluate early warning systems. We present a seismo-acoustic analysis of debris flow activity at Illgraben, Switzerland, with infrasound data collected with a small aperture array. Events are recorded as emergent signals of long duration, with seismic and infrasound amplitudes scaling with the flow discharge. The spectral content appears on the contrary quite stable and peaking at 8 Hz for the seismic and ≈ 5 Hz for the infrasound that suggests two separate processes of elastic energy radiation, most likely bed-load transport for the seismic and waves at the free surface for the infrasound. Although amplitude and frequency content of the infrasound signal radiated by the debris flow are well within the processing limits, most of the signal is not showing any correlation among the array elements. We suggest that this is a consequence of the contribution of multiple sources of infrasound acting with variable amplitude and phase along the surface of the debris flow. At Illgraben, coherent infrasound is recorded only from fixed sources, corresponding to check dams within the channel. Here infrasound radiation is increased and the dams turn into predominant sources of energy. This allows to un-ambiguously identify the occurrence of debris-flow at Illgraben

with the infrasound array, from a remote and safe position and with a timing that is similar to the early warning system based on in-channel sensors. This clearly shows how infrasound arrays could be used as an efficient early warning systems.

4.2 Introduction

Debris flows are mobilized water/sediment mixtures in steep mountain torrents and constitute a severe natural hazard for downstream communities. Glacier lake outburst floods, natural dam failures or landslides may initiate debris flows in a much less predictable way than more common precipitation-triggered events. Debris flow events have been investigated extensively through seismic and acoustic observations (see e.g.[49, 50, 51, 52, 53, 54, 55, 1]), both to investigate the process and evaluate the potentials for remote monitoring.

Theoretical and experimental studies of seismic energy radiation by debris-flow suggest a strong analogy with rivers [53, 55], with seismic energy most likely radiated by the collisions within the boulder snout. [55] developed a mechanistic physical model for seismic energy radiation by debris-flow starting from the bed load transport model proposed for rivers [50, 56, 57] and showed how frequency depends only on the source-to-receiver distance while amplitude of seismic ground shaking is proportional to boulder size and flow velocity as well as boulder snout extension. This was confirmed by direct seismic observations of the January 9, 2018 Montecito debris flow [55] that also suggested the existence of additional sources radiating energy within different frequency bands, possibly related to water flow interaction with channel bed and banks and standing waves [58].

Among the others, waves at the water free surface are considered the most efficient mechanism of infrasound energy radiation by rivers [58]. However, experimental observation showed that infrasound is mostly generated in fixed position, whenever waterfalls are present [59]. In particular, [60] suggest that infrasound is produced at dams for water falling into the absorption pool that triggers waves radiating infrasound as a dipole source. Therefore, it is expected to have multiple sources of infrasound from rivers according to flow dynamics and channel geometry.

This existing discrepancy between the availability of models and studies focusing on seismic energy radiation from rivers as well as debris flows (see e.g. [50, 56, 57, 53, 55]), compared to infrasound [58], partly explains why the mechanism of infrasound radiation by debris flow hasn't been really investigated yet in depth. Most of the studies available [61, 51] up to now mostly focused on event detectability for monitoring purposes.

The wide range of monitoring and detection approaches (see [49] for a review) reflects the technical challenges inherent to debris flow early warning. On one hand, debris flows typically move at moderate velocities of less than 10 m/s [62] and thus early warning for downstream communities is possible if flows are detected quickly upon formation. On the other hand, high mountain torrents are difficult to access and subject to frequent rock falls, landslides and other mass movements. Consequently, instrumentation in lower catchment reaches is often preferable yet comes at the cost of reduced early warning time.

Among existing monitoring techniques, infrasound measurements have recently received particular attention, because in principle they do not require installations within or near a torrent. Instead, infrasound signals are detectable at distances up to hundreds of kilometers (see e.g. [63]). The infrasound signal is generated as moving particles collide with atmosphere molecules and generate elastic air waves. Depending on flow rheology and attenuation in the air, the infrasound signal's frequency content of debris flows concentrates in a band below 40 Hz [64].

Though suited for remote detection, infrasound measurements of debris flows face key challenges: infrasonic debris flow signals have emergent envelopes and lack impulsive, easily detectable phases. Moreover, torrent-related noise sources such as rock-falls, water flow and above all wind can have amplitudes comparable to the debris flow signal [65, 66]. Importantly, apart from a high noise floor, topographic barriers (e.g. mountain ridges, hills) between source and sensor also reduce the signal-to-noise ratio [67, 22, 51].

In order to tackle these challenges, realtime trigger algorithms process debris flow signals in frequency space rather than time space to discriminate them from noise signals [66, 68]. Detection reliability can be increased with concurrent recordings of ground motion using geophones co-located with

the infrasound microphone [61, 68].

Array techniques further improve detectability of infrasound sources. The technique enhances signal-to-noise ratios and distinguishes signal from noise in terms of source back-azimuth and apparent infrasonic velocity. Array techniques are widespread in infrasound (see e.g. [69]) and seismic (see e.g.[70]) monitoring. They have been used for the detection and monitoring of different kinds of gravity currents such as snow avalanches [71, 47, 72], pyroclastic flows [29, 13] and lahars [73] but have yet to be applied to debris flows.

Here we use an infrasound antenna to study the infrasound radiation mechanism of debris flows at Illgraben, one of Switzerland's most debris-flow-prone torrents. We combine seismic and infrasound observations to further investigate seismic-acoustic coupling and constrain the existence of multiple processes of elastic energy radiation in the ground and the atmosphere by the debris flow. Eventually we investigate the efficiency of infrasound array monitoring to provide an early detection of the debris-flow events with remote observations and investigate its potential as an early warning system compared to in situ observations.

4.3 Study site

Illgraben is a steep torrent in southern Switzerland's Canton Valais and feeds directly into the Rhone River (Figure 4.1). It is about 5 km long draining a catchment area of 10 km^2 . Debris flows with volumes of several tens of thousands of m^3 occur on average 3-5 times per year and are a significant and sometimes dominant sediment supply mechanism from Illgraben to the Rhone River [74]. The upper catchment has steep slopes of 40 degrees or above producing frequent rockfalls or landslides [75]. The largest landslide in recent decades occurred in 1961 and deposited 3,500,000 m^3 of material in the torrent. The main source of sediment generating debris flows at Illgraben is from the numerous landslides originating predominantly from steep slopes at the southern part of the catchment [76]. Debris flows typically occur in summer months when heavy precipitation mobilizes sediments in the channel or in steep gullies within lateral slopes [77]. A series of check dams (CD), most of which are situated on the inhabited debris fan

in the Rhone valley (Figure 4.1) stabilizes the channel against erosion. As a result, most debris flows no longer overtop the channel bank and significant damage last occurred in 1961 when a road bridge was destroyed [74].

The Swiss Federal Institute for Forest, Snow and Landscape Research WSL installed a scientific observatory [78] and maintains an early warning system based on in-torrent debris flow detections [74]. The arrival times of the debris flow front are detected with geophones installed behind steel plates at CD 1, 27 and 29 (Figure 4.1). The geophones provide voltage impulses induced by vertical vibrations as debris moves across their steel plates and debris flow front arrival is defined when this signal exceeds a threshold voltage of 0.2 V. To calculate debris flow velocities near the Illgraben mouth, we use differences of the flow front's arrival time at CD 27 and 29 (Figure 4.1). Furthermore, we measure flow stage using a laser altimeter suspended from a bridge across the channel at CD 29. From flow stage and flow velocity, we calculate discharge and total debris flow volume.

4.4 Instrumental setup

The infrasound array was deployed north of the Illgraben in a flat forested area at an elevation of 750 m and at a distance of ≈ 0.6 km from Illgraben mouth (Figure 4.1). We used a FIBRA infrasound array (www.item-geophysics.it) that is designed to operate with fiber optic connection among up to 5 different array elements. Analogue pressure data are converted to digital at each array element at 50 Hz and 16 bits, and are transmitted through fiber optic to a central unit where data is synchronized, GPS time stamped, locally recorded and made available through TCP/IP for data transmission. Power requirement is ≈ 1 W for the central unit and as low as ≈ 0.1 W for the array element. The use of an array with fiber optic allows to increase significantly the signal to noise ratio and prevents the risk of damages related to lightning or electric discharges. Each array element is equipped with a differential pressure transducer with a sensitivity of 400 mV/Pa in the pressure range of ± 12.5 Pa and frequency response between 0.01 and 200 Hz. For this study we used 4 out of the 5 available channels and deployed the sensors with a triangular geometry in order to have the best azimuthal resolution. Array

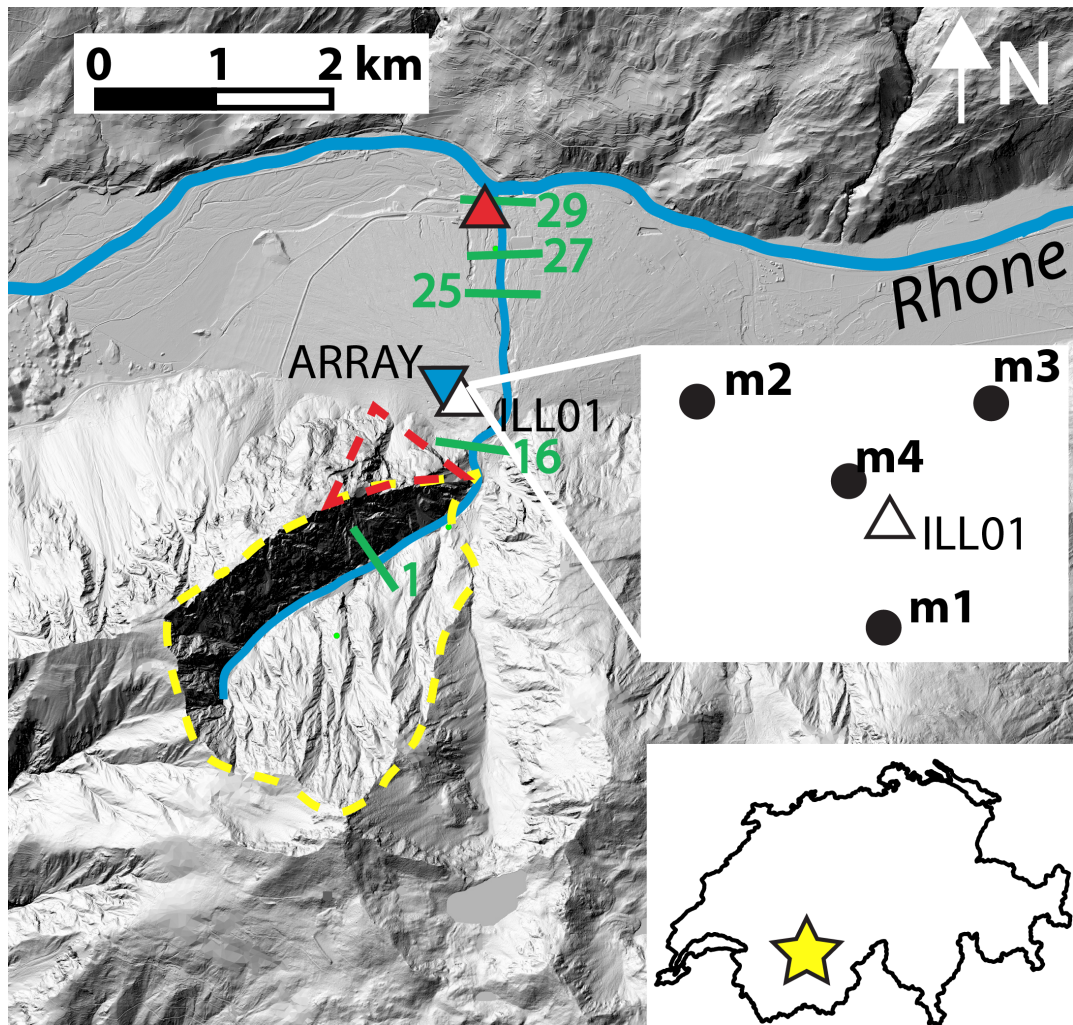


FIGURE 4.1: Illgraben catchment and Rhone valley in Switzerland's Canton Valais. Seismic sensor ILL01 is indicated by white triangle, infrasound array by blue upside-down triangle and automatic camera by a red triangle. Upper inset shows positions of four individual microphones (black filled circles) making up the infrasound array. Lower inset shows Switzerland and location of Illgraben (star). Locations of selected CD are presented by green bars with numerical labels. Dashed yellow line outlines an area which we refer to as upper catchment, while dashed red line marks the ridge between the array and CD1.

aperture (maximum distance between 2 array elements) is 160 m and is optimized to analyze infrasound signals in the frequency band between 1 and 10 Hz. The array was deployed on May 15, 2017 and operated continuously until June 18, 2017.

We installed a Lennartz LE3D 1s seismometer (ILL01 in Figure 4.1) recording all three dimensions of ground velocity with a flat response between the sensor's natural frequency of 1 Hz and 80 Hz. The sensor was placed into a 30 cm deep pit, which was subsequently filled up with sand. Ground motion was recorded with a Nanometrics Centaur digitizer at 100 Hz and continuously telemetered to the Swiss Seismological Service. The seismic sensor was co-located with the infrasound array north of the Illgraben in an easily accessible area.

For the present analysis, in addition to infrasound array and seismic data, we consider information on flow evolution provided by in-channel sensors installed at CD1 and CD25 as well as the position of CD16 (Figure 4.1, Table 1). CD1, built at an elevation of 1090 m inside the Illgraben and with a height of ≈ 45 m, is positioned at a distance of 1600 m from the array and has a corresponding back-azimuth (direction from the dam to the array) of 200°N . The dam is not visible from the array being masked by the northern ridge of the Illgraben (dashed red line in Figure 4.1). Considering a straight line from the dam to the array along topography, the ridge reaches a maximum altitude of ≈ 1200 m (450 m higher than the elevation of the array). CD16 is on the contrary almost line of sight to the array (Figure 4.1), being positioned at an elevation of ≈ 850 m, a distance of ≈ 750 m from the array and with a back-azimuth of 155°N . The distance between CD1 and CD16 along the channel of the Illgraben is ≈ 1400 m with an elevation difference of ≈ 200 m (mean slope of 15%) from the base of the CD1. CD25 is positioned at an elevation of ≈ 700 m and a distance of ≈ 900 m from the array. The corresponding back-azimuth is 35°N . The along-channel distance between CD16 and CD25 is ≈ 1500 and the minimum distance between the Illgraben channel and the array of ≈ 500 m is approximately half the way between CD16 and CD25 (Figure 4.1). CD1 and CD25 are equipped with geophones providing the exact timing of the debris flow passage.

4.5 Debris flow events

Our study focuses on three debris flows (Fig. 4.2), which occurred in 2017 (Table 1). All three events were large compared to typical debris flows at Illgraben [74] and the largest one (May 29, 2017) had a volume of 70.000 m^3 ,

TABLE 4.1: Parameter estimations for the three largest 2017 debris flows at Illgraben discussed in this study.

Date	Flow stage (m)	Vel. (m/s)	Vol. (m^3)	Disch. (m^3/s)	CD 1 (UTC)	Infrasound (UTC)
29 May 2017	4.8	6.7	70,000	270	16:58:31	16:58:50
3 June 2017	3.3	4.3	24,000	150	23:27:38	23:27:28
14 June 2017	3.5	7.2	33,000	150	19:30:48	19:30:27

which is close to the mean annual supply of sediment ($100.000 m^3$) from Illgraben to the Rhone River [75]. The event on June 14, 2017 was furthermore exceptionally large moving at a velocity of $7.2 m/s$ between CD27 and CD29.



FIGURE 4.2: Picture of the front arrival of a debris flow at Illgrabenn (July 1, 2018) taken from an automated camera (red triangle in Fig.4.1) operated by the WSL [77].

All events are recorded as emergent seismic and infrasonic signals of long duration (30-40 minutes), with peak infrasonic amplitude for the long lasting emergent phase of $0.5 Pa$ and peak seismic amplitude of $\approx 2.5 \mu m/s$ (Figure 4.3). The May 29 event, in particular consists into two main flows, one after the other, with the second event slightly shorter (≈ 10 minutes) and of

smaller seismic ($1.5 \mu\text{m/s}$) and infrasonic (0.3 Pa) amplitude than the first event. From figure 4.3 it is evident how the June 4 and June 14 debris flows differ from the May 29 event for the presence of a faster increase of the seismic signal, while the rise phase of the May 29th event is more gentle.

The May 29 and June 14 events, are also characterized by high frequency transients that over-impose on the spindle shaped signals produced by the debris flow, that are much clearer and of larger amplitude ($\geq 1 \text{ Pa}$) in the infrasound record rather than in the seismic. These transients are produced by lightning and subsequent infrasound radiated by the thunder and propagating across the array (see Appendix B: Lightning Activity).

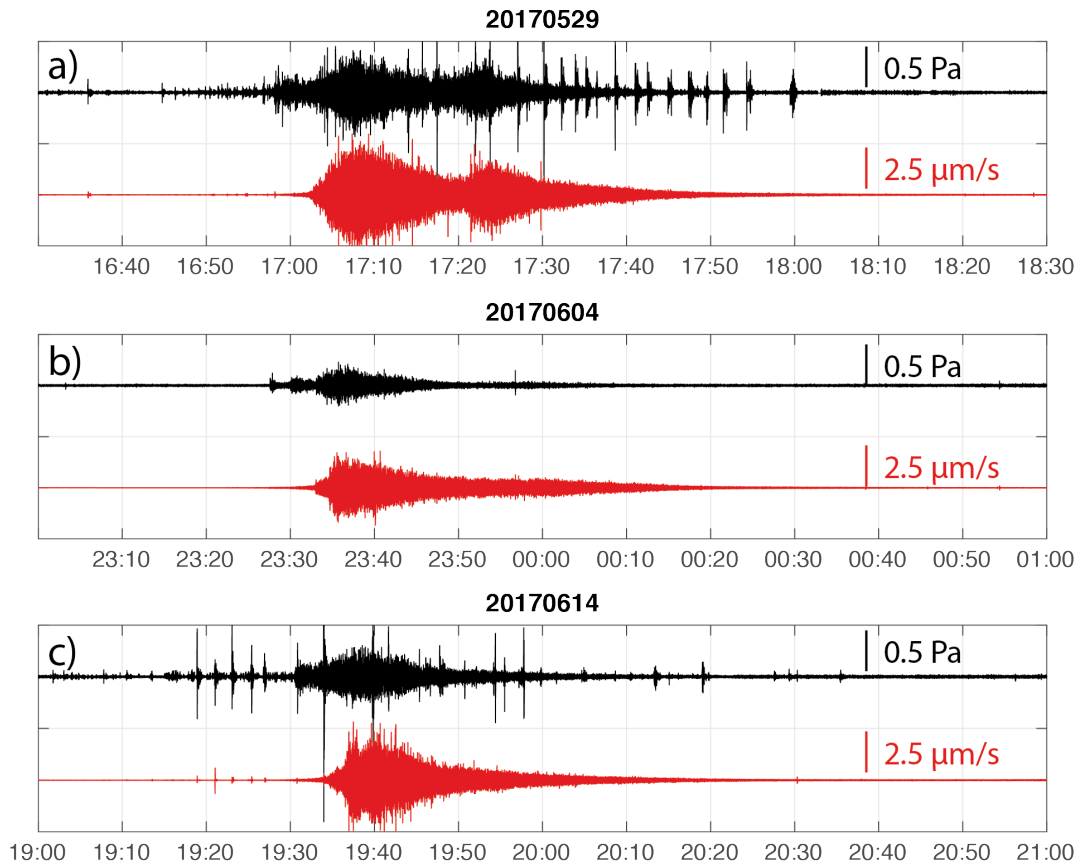


FIGURE 4.3: *Infrasound (black) and seismic (red) records of debris flows recorded in May 29 (a), June 4 (b) and June 14 (c), 2017. Infrasound waveforms are band-pass filtered between 1 and 5 Hz.*

4.5.1 Infrasound array analysis of debris-flows

An infrasound array consists on multiple infrasonic sensors deployed in the field and used as an antenna. It allows reducing the signal-to-noise ratio and identifying signal, which unlike noise is coherent across the elements of the array, in terms of back-azimuth (B_{az}) and apparent velocity (C_a). While the former identifies the direction of infrasound wave propagation, the latter corresponds to the velocity the wave would have if it was propagating in plane fitting the array and is defined as the real propagation velocity (c) divided by the sine of the take off angle ($C_a = c / \sin \gamma$).

The analysis of infrasound array data was performed by calculating to correlation between data recorded at the different elements of the array. For this study the analysis is applied over 10 second-long time windows with 5 seconds of overlap on infrasound data band-pass filtered between 1 and 10 Hz. For each time window of analysis a detection is identified whenever coherent data is recorded across the array, and time delay among array elements is used to calculate back-azimuth and apparent velocity of the infrasonic wave-field. Details about the infrasound array processing are provided in the Appendix A (Infrasound array analysis).

Array processing of infrasound records of the May 29, 2017 event (Fig. 4.4a) shows that coherent infrasound signal is recorded only during the initial part of the flow and highlights the existence of 3 phases characterized by stable values of back-azimuth and apparent velocity (Figure 4.4b, c). The first phase (1 in Figure 4.4b) starts around 16:45 UTC, \approx 15 minutes before the debris flow is observed at the CD1 (16:58:31 UTC). The signal is recorded with a back-azimuth of 200-220 °N and high values of apparent velocity (480 m/s) that suggests pressure waves produced inside the Illgraben and propagating across the ridge (dashed red line in Figure 4.1) to be eventually recorded at the array (Figure 4.5). Considering a propagation velocity of sound (c) around 340 m/s, the measured apparent velocity of 480 m/s is consistent with a take off angle (θ) of 45 degrees. This value is in quite a good agreement with a pressure wave produced inside the Illgraben and crossing the ridge, that is approximately 800 m far and 600 m higher than the array (Figure 4.5).

This first phase lasts approximately 15 minutes until 17:00 UTC, when the second phase (2 in Figure 4.4b, c) starts being characterized by lower

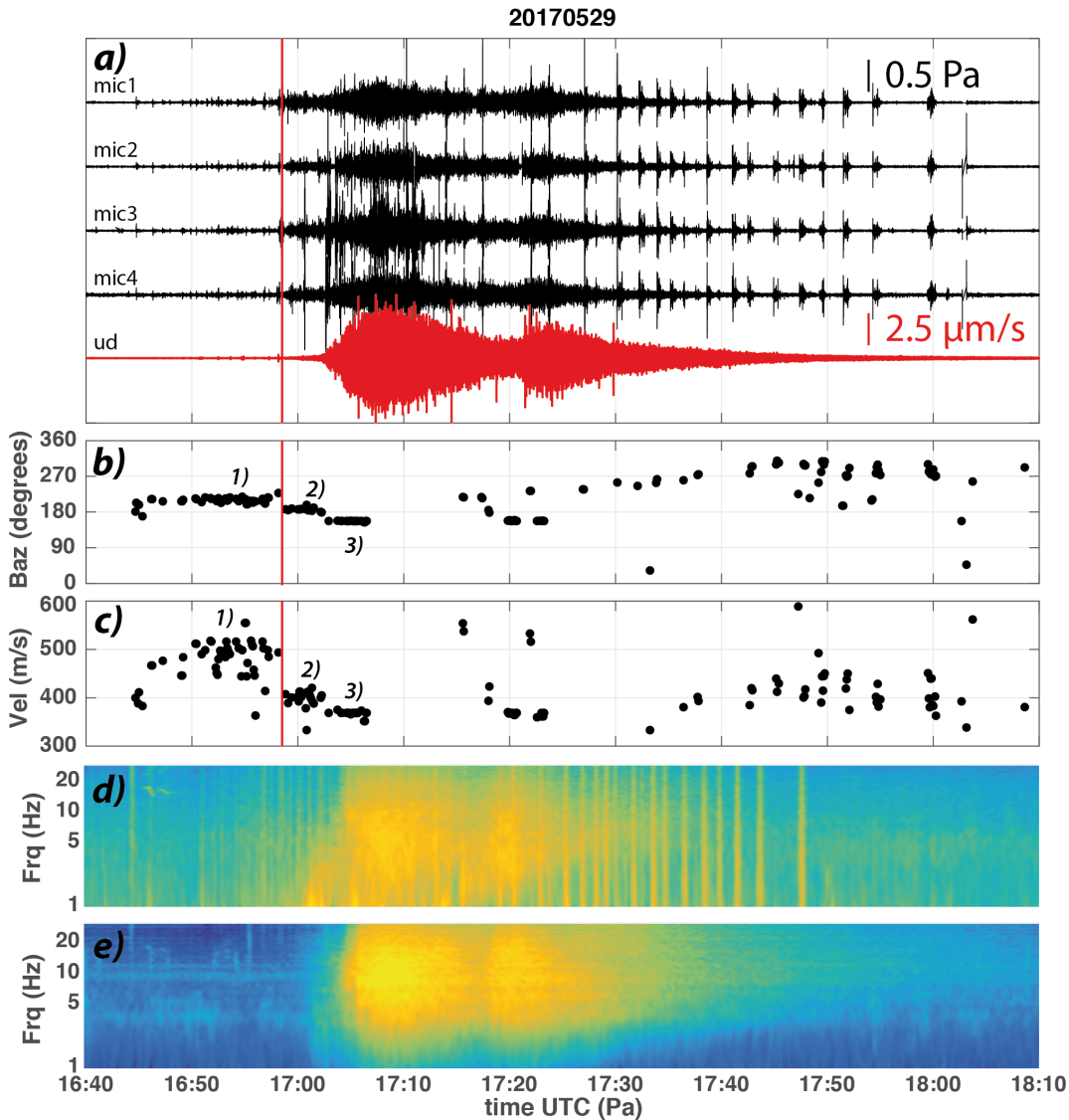


FIGURE 4.4: 1.5-hour-long sample of infrasound array (black) and seismic (red) records of the May, 29, 2017 debris flow event (a). Back-azimuth (b) and apparent velocity (c) of infrasound detections. Normalized PSD of infrasound (d) and seismic (e) records. The numbers in subplots b and c identify the different phases identified from infrasound array processing and discussed in the text. The red vertical line marks the arrival times at check dam 1 (CD1, Figure 4.1). Infrasound waveform in subplot a is band-pass filtered between 1 and 5 Hz.

values of back-azimuth ($\approx 190^\circ \text{N}$) as well as apparent velocity ($\approx 400 \text{ m/s}$) (Figure 4.4b, c). This direction of propagation matches with CD1, positioned within the Illgraben at a distance of $\approx 1600 \text{ m}$ from the array. Infrasound



FIGURE 4.5: *Google-earth projection of back-azimuth of the three phases identified from infrasound back-azimuth during the initiation of the May 29, 2017 event and highlighted in Figure 4.1.*

produced at the dam crosses the mountain ridge (dashed red line in Figure 4.1) to be eventually recorded at the array, after a propagation time of ≈ 5 seconds. The lower value of measured apparent velocity from phase 1 is consistent with the lower elevation of the ridge along the $\approx 190^\circ\text{N}$ back-azimuth direction from the array. While the debris flow is flowing downhill along the Illgraben, infrasound continues to be recorded persistently from $\approx 190^\circ\text{N}$, the 45 m waterfall at CD1 being the most energetic source of sound. This is in agreement with experimental and theoretical studies of infrasound produced at waterfalls and dams [59, 60].

Eventually when the flow exits the valley and reaches CD16 (Figure 4.1) infrasound starts abruptly to be recorded with a different back-azimuth (155°N) pointing directly to the dam (phase 3 in Figure 4.4b, c). For the specific case of the May 29 event, infrasound signal from this same back-azimuth is recorded also between 17:19 and 17:23 UTC, when a second flow reaches the dam. Similarly to what was inferred for phase 2 we suggest that the increased infrasound radiation produced by the waterfall [59, 60] at the dam is the most energetic source of infrasound, that is detected as a stable source

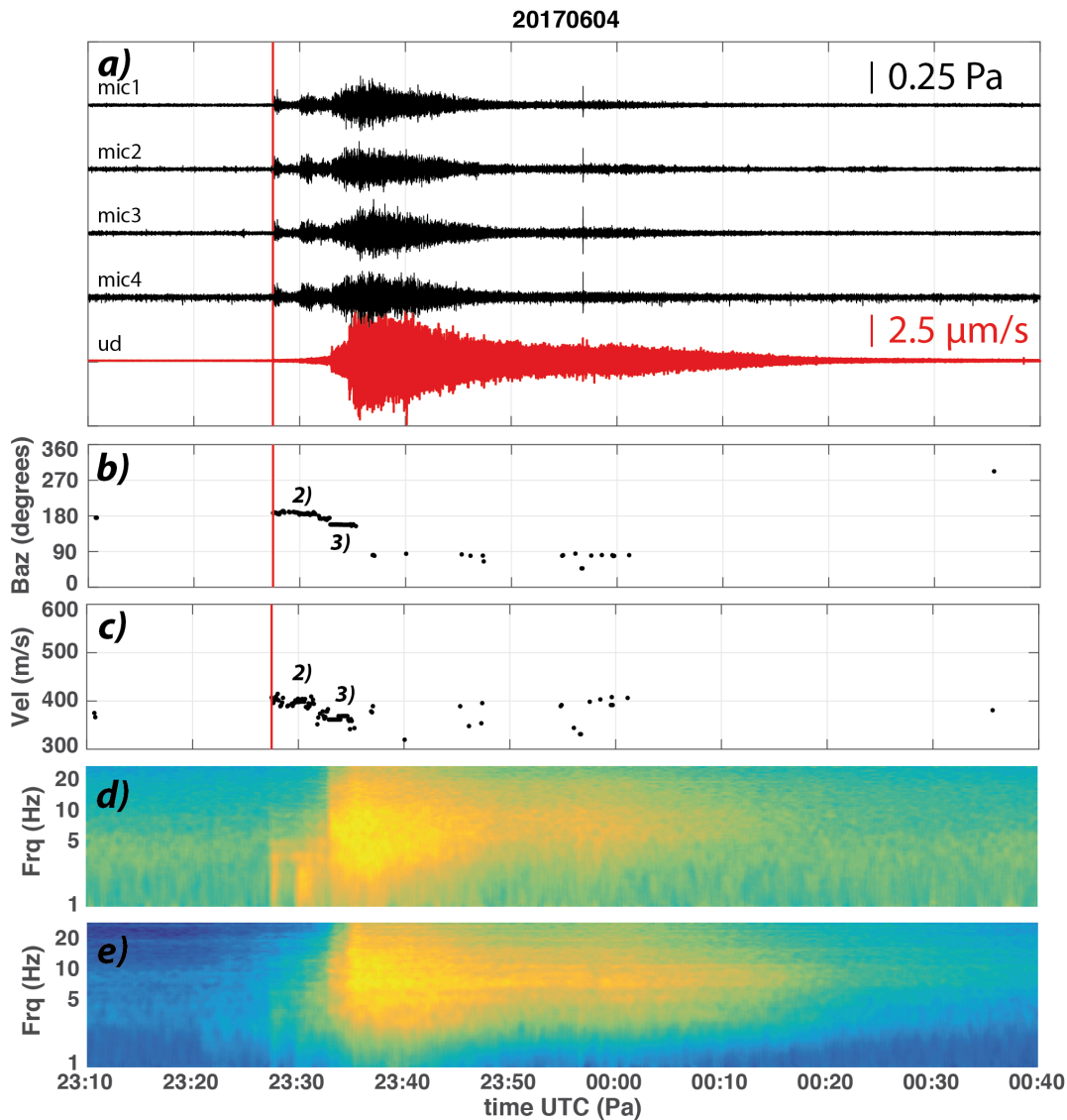


FIGURE 4.6: 1.5-hour-long sample of infrasound array (black) and seismic (red) records of the June 4, 2017 debris flow event (a). Back-azimuth (b) and apparent velocity (c) of infrasound detections. Normalized PSD of infrasound (d) and seismic (e) records. The numbers in subplots b and c identify the different phases identified from infrasound array processing and discussed in the text. The red vertical line marks the arrival times at check dam 1 (CD1, Figure 4.1). Infrasound waveform in subplot a is band-pass filtered between 1 and 5 Hz.

although the flow keeps moving downhill.

This peculiar variation of back-azimuth and apparent velocity is observed

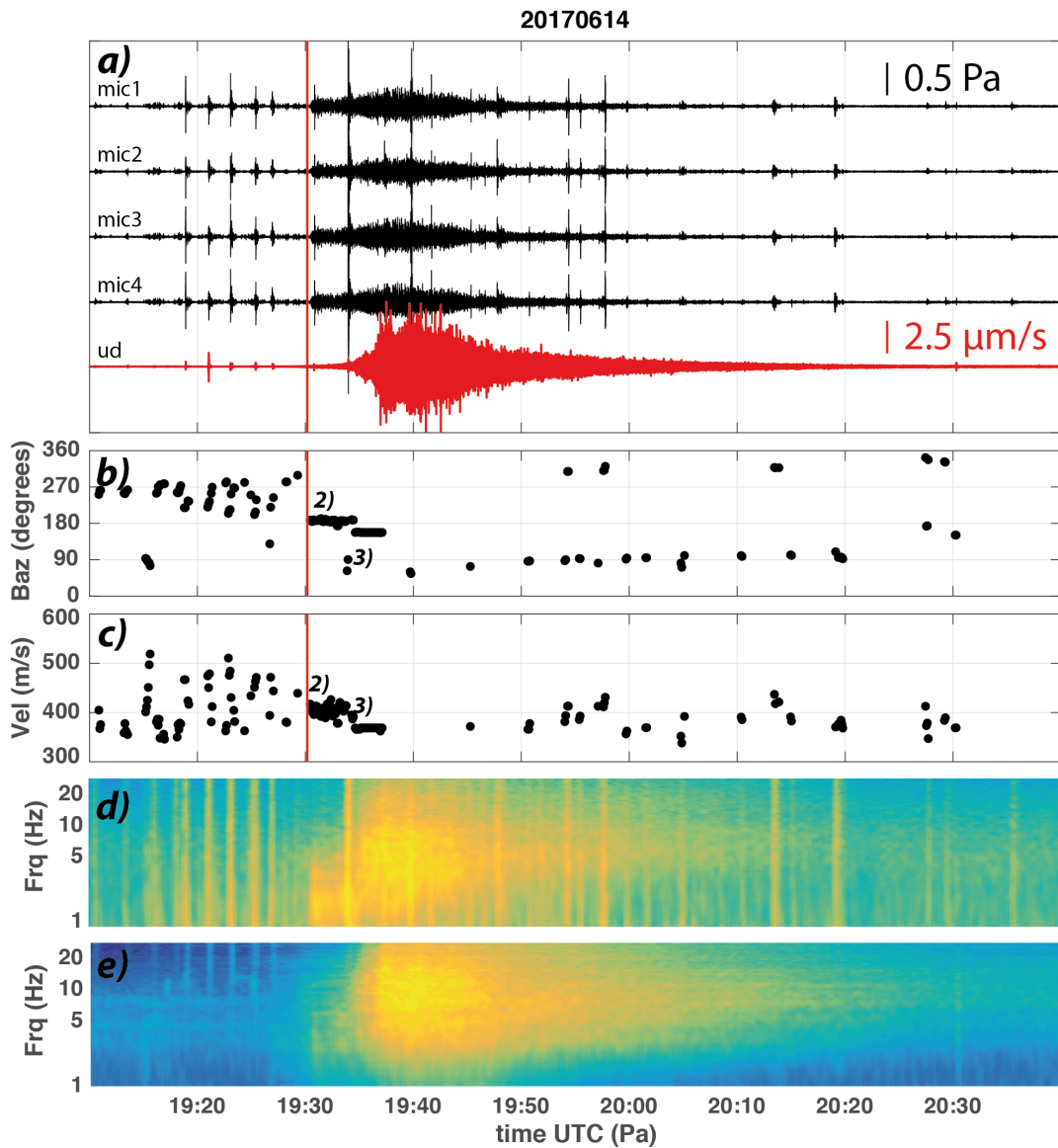


FIGURE 4.7: 1.5-hour-long sample of infrasound array (black) and seismic (red) records of the June, 14, 2017 debris flow event (a). Back-azimuth (b) and apparent velocity (c) of infrasound detections. Normalized PSD of infrasound (d) and seismic (e) records. The numbers in subplots b and c identify the different phases identified from infrasound array processing and discussed in the text. The red vertical line marks the arrival times at check dam 1 (CD1, Figure 4.1). Infrasound waveform in subplot a is band-pass filtered between 1 and 5 Hz.

for all recorded events (Figure 4.6, 4.7, 4.8), suggesting that a stable mechanism of infrasound radiation during the debris flow evolution at Illgraben exists. In particular all events are characterized by infrasound radiation from

stable sources during the initial phase of the event (phase 2 and 3), while no more detections of infrasound signal are observed despite the infrasound amplitude keeps increasing.

The precursory infrasound of phase 1 is observed only for the May 29 event. Based on wave parameters (back-azimuth and apparent velocity) we suggest that this phase possibly reflects debris flow initiation within the graben, able to radiate infrasound that is crossing the mountain ridge (dashed red line in Figure 4.1) and is recorded at the array (Figure 4.4b, c). However we cannot exclude that such signals might be radiated by small landslides occurring on the northern flank of the ridge, as the back-azimuth (200-220 °N, Figure 4.5) is indeed pointing to a sector of the ridge that is strongly eroded. Future observation will be required to further investigate this aspect.

4.5.2 Spectral analysis of debris-flows

Spectral analysis of seismic and infrasound records (subplots *d* and *f* of Figures 4.4, 4.6, 4.7) shows how the seismic signal of the debris flow is characterized by a broad spectrum from few Hz up to >25 Hz, and peaked around 8 Hz, without any obvious systematic variation in the spectral content through time. On the contrary, the infrasound spectrum shows a low frequency component (<2 Hz) at the beginning of the event, which increases through time, before a broad frequency content (between 2 and 10 Hz and peaked around 5 Hz) is recorded abruptly (Figure 4.4, 4.6, 4.7).

The comparison with the timing of infrasound detections helps clarifying the recorded spectrogram. The abrupt increase of the infrasound frequency content observed for all events corresponds indeed to the time of the first detections with back-azimuth of 155 °N, that marks the arrival of the debris flow at CD16 at the Illgraben mouth. The low frequency infrasound recorded before is thus produced by the flow while it is still flowing within the Illgraben and is recorded at the array after crossing the ridge (dashed red line in Figure 4.1), while signal recorded afterwards has line-of-sight propagation to the array. Consistently with modeling and observation of topography effects on short range infrasound records [67, 22] the ridge does

not prevent infrasound being recorded but strongly attenuates the high frequency component of the signal, while lower frequency component is much less affected.

4.6 Discussion

Results derived from array analysis of infrasound data and comparison of the spectral content of infrasound and seismic data, as presented in the previous section, suggest a complex mechanism of infrasound and seismic energy radiation by the debris flow. In this section we first investigate the mechanism of infrasound radiation, discuss the coupling of the seismic and infrasound sources and eventually discuss the possible use of infrasound array analysis as a remote early warning system for debris flows.

4.6.1 Mechanisms of infrasound radiation by debris flow at Illgraben

The infrasound array analysis, combined with the timing provided by the instrumented check-dams can be used to provide insights on the dynamics of the flow. Figure 4.8 shows the detail of the infrasound detections for all events, aligned according to the detection time at CD1 provided by the geophone. The figure clearly shows that all events share phases 2 and 3, while phase 1 is recorded only during the major event of May 29, 2017.

Stable detections characterizing phase 2 start exactly when the debris flow passes CD1 for all events (Figure 4.8b) and continues for a time period of 3-4 minutes even though the flow is moving downhill, until phase 3 starts. This is marked by an abrupt change in the back-azimuth and apparent velocity of infrasound detections and corresponds to the time the debris flow reaches CD16 (Figure 4.1). By that time it starts radiating infrasound from this fixed position that remains stable for several minutes even though the flow keeps moving downhill. This is consistent with theoretical and experimental studies of infrasound radiated at waterfalls and dams [59, 60].

Detecting a stable source position in case of moving sources is not unexpected and is a consequence of infrasound array analysis, that in case of multiple sources detects preferentially the most energetic one. Such a behavior

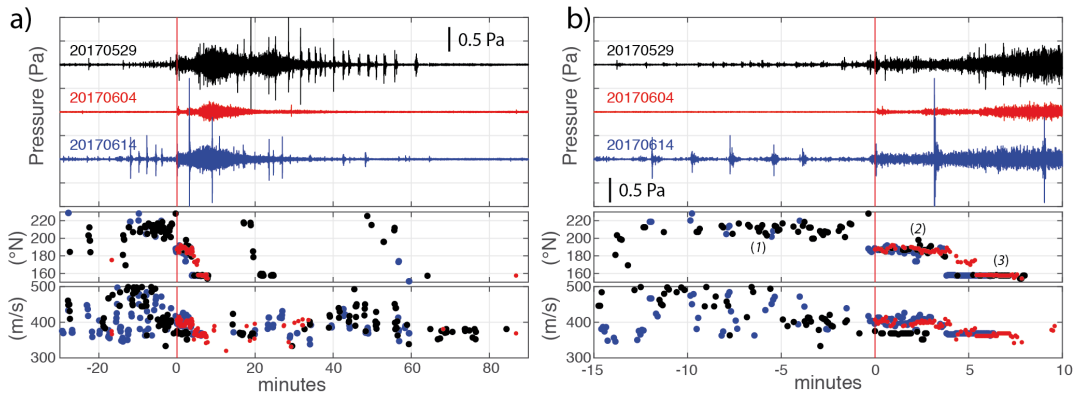


FIGURE 4.8: 90-minute-long example (a) and 25 min-long detail (b) of pressure records, back-azimuth and apparent velocity for the 3 debris flow events aligned according to the time of detection at CD1 (red vertical line).

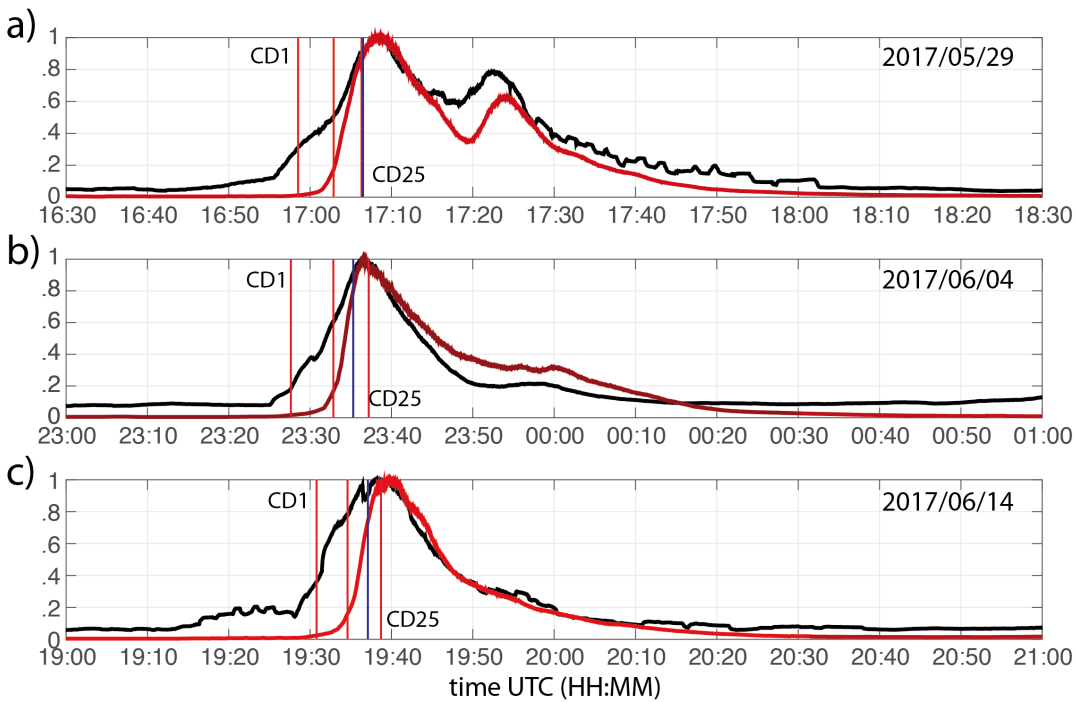


FIGURE 4.9: Normalized envelope of infrasound (black) and seismic (red) signals recorded by the 3 debris flows. Red vertical lines mark the timing of the debris flow at CD1, CD16 and CD25, with the timing at CD16 inferred from infrasound array analysis and timing at CD1 and CD25 measured directly at the dam with geophones. The blue vertical line marks the end time of phase 3 (Figure 8) of infrasound detections.

has been observed already for snow avalanches [72] and pyroclastic density currents [11] passing a discontinuity in the topography where infrasound energy radiation focuses in a stable position. However, snow avalanches and pyroclastic density currents produce a coherent infrasonic signal all along their downhill moving front and array analysis allows to clearly track their movement [11, 72].

For the debris flow events we observe that coherent infrasound is recorded only when the flow crosses the dams (Figure 4.8) while it is not detected by the array otherwise although the signal amplitude is high and the frequency content is relatively low (<10 Hz). This indicates a lack of coherence. Figure 4.9 shows the normalized envelope of the infrasonic (black) and seismic (red) signal compared to the timing of the flow at the different check dams (CD1, CD16, CD25, red lines) and the end time of phase 3 (blue line), that marks the end of coherent infrasound.

For all cases, infrasound starts increasing 10-20 minutes before the collocated seismic signal (Figure 4.9). A significant departure between the infrasonic and seismic envelope is observed already before the flow reaches CD1, suggesting that infrasound radiated by the flow is able to cross the mountain ridge (dashed red line in Figure 4.1) to be recorded at the array while no clear seismic signal is recorded at ILL01 station. After the flow reaches the CD16 and enters the Rhone valley, also the amplitude of the seismic signal recorded at ILL01 station starts increasing. This is consistent with previous observations performed by [61] and [51] who recorded infrasound and seismic signals after the flow entered the Rhone valley and suggested that earlier infrasound detections were possibly masked by topography effects.

When phase 3 ends (blue line in Figure 4.9), coherent infrasound at the array is no more detected (Figure 4.8) but the envelopes of seismic and infrasound signals keep rising through time clearly indicating that more and more elastic energy is radiated by the flow in the air and in the ground. However maximum amplitude is not recorded when the flow head reaches the minimum distance of the channel to the array (≈ 500 m), approximately half the way between CD16 and CD25, as would be expected in case of a simple moving point source. For all cases, when maximum amplitude is recorded, the flow has already reached CD25, ≈ 700 m more distant than the

minimum distance to the array. Only afterwards infrasound and seismic amplitude decrease following a similar trend.

Numerical simulation of infrasound radiated by an extended source.

The infrasound array analysis presented above points to a complex mechanism of infrasound radiation by the debris flow at Illgraben. Infrasound is indeed radiated at the dams, that appear as stable sources of energy, even though the flow keeps moving downhill. Yet the main part of the signal, despite being characterized by high amplitude and low frequency, shows low coherence and is thus not detected by the array processing.

In order to investigate the lack of coherent infrasound, and thus not detectable by array processing, we modeled the infrasound radiated by an extended linear source and investigated the array detectability. Infrasound from rivers is indeed believed to be produced by free waves at the water surface (e.g.[58]). Therefore, multiple sources will be active simultaneously and at different locations, when water is flowing in a river.

Figure 4.10 shows a sketch of the problem. We consider a linear source of length ($L=500$), formed by 50 different point sources of infrasound, positioned 10 meters apart from each other, and moving with a horizontal velocity (u) of 10 m/s. A spacing of 10 m between adjacent sources is consistent with observation of the free waves at the surface of debris flow. The head of the linear source of infrasound (black in Figure 4.10a) reaches the minimum distance to the array, that corresponds to 300 m from mic2 in Figure 4.10, at time $t=50$ sec and with corresponding back-azimuth to the array of 270° N.

Each source is assumed to produce a pressure wave in the atmosphere with an amplitude of 1 Pa and a peak frequency of 3 Hz, in accordance with observed spectra of infrasound radiated by debris flows at Illgraben (Figures 4.4, 4.6, 4.7). Random noise is added to the infrasound waveform radiated by each point source, and a random phase shift is allowed for the extended source. This assures that at the same given time, the different point sources of the extended source can radiate infrasound with the same amplitude and same frequency but with a different phase. The resulting infrasonic waveform at each element of the array is obtained considering the whole contribution for all sources through time, corrected for both propagation time and attenuation.

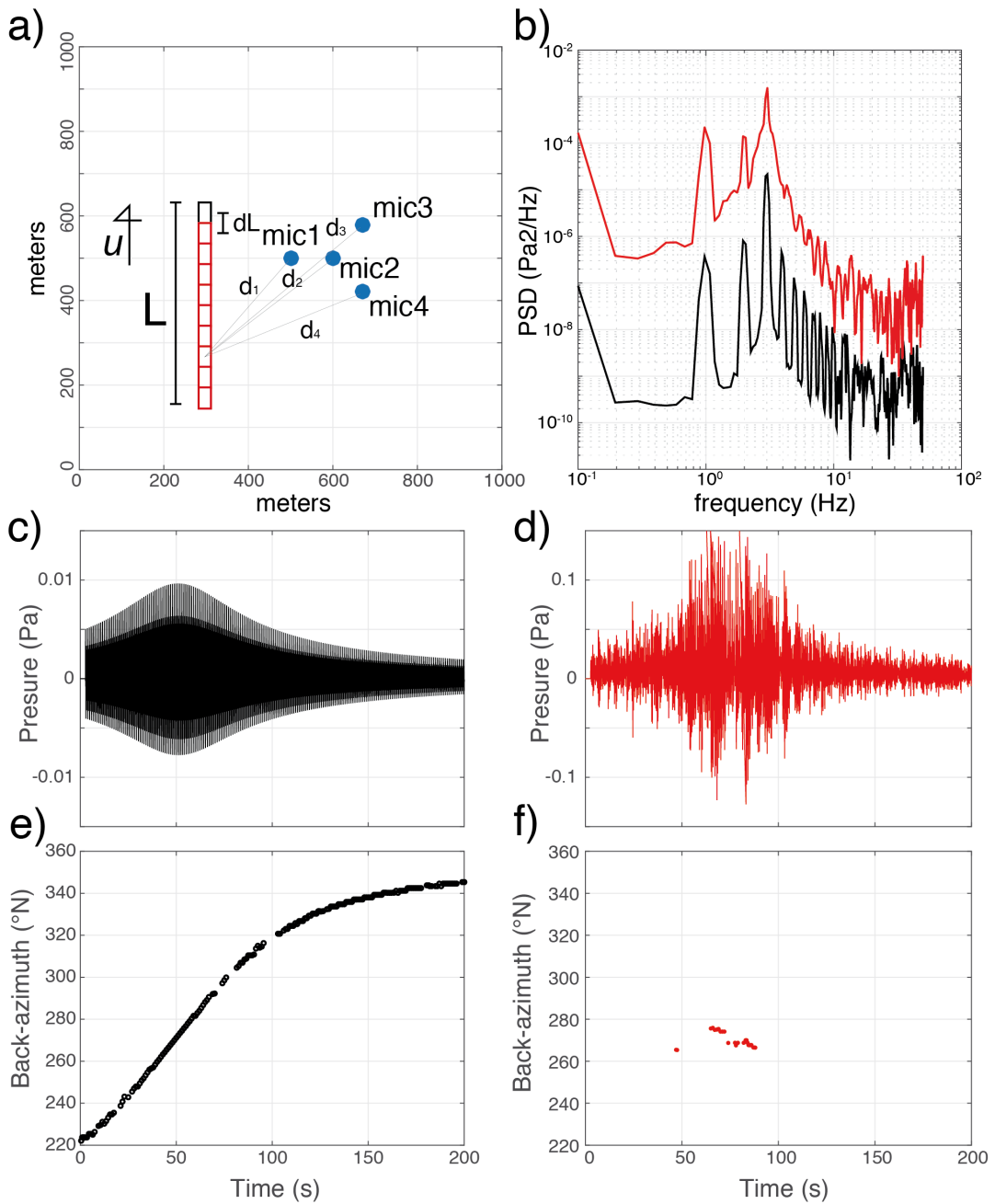


FIGURE 4.10: *a*) Sketch of an extended moving source simulating a flow and radiating infrasound recorded by an infrasound array. We assume elastic energy being radiated only at the head of the flow (black) or by the whole flow (black and red). Infrasound signals and detections at the array in case of elastic energy being radiated by the point source (c, e) or by the extended source (d, f) and corresponding power spectral density (b).

We first consider infrasound being produced only a single point source at the head of the flow (black in Figure 4.10a). The simulated infrasound signal recorded at mic1 of the array has a cigar shape envelope with the maximum amplitude recorded after 50 seconds (Figure 4.10c). The signal is highly coherent and infrasound array processing allows to easily track the movement of the source in terms of back-azimuth variation through time (Figure 4.10e).

The simulated infrasound signal recorded at mic1 considering the contribution of 50 point sources has a cigar shape envelope, similar to the point source, but its maximum amplitude is recorded after 75 seconds (Figure 4.10d). The delay of 25 seconds is required for the barycenter of the extended source to reach the minimum distance to the array (i.e. 250 m at 10 m/s). Moreover, the contribution of multiple sources, despite maintaining the amplitude, waveform characteristics (Figure 4.10c, d) and spectral content (Figure 4.10b) similar to a moving point source, results in a dramatic decrease of signal coherence that prevents the possibility to track the source with array processing (Figure 4.10f).

This simple example allows consolidating a model of infrasound radiation by debris flow, with free waves at the water surface along the entire flow length radiating elastic energy to the atmosphere, with variable phase. These contribute to a spindle shape signal, of amplitude exceeding 0.5 Pa at a distance of >500 m from the source but with low coherence. Therefore, array processing is not really useful to track and investigate the flow, unless discontinuity points of the topography, such as change of slopes or dams, result in stable sources of infrasound clearly detectable by the array. We suggest therefore that the mechanism of infrasound radiation by debris flow is different from other density currents like snow avalanches or pyroclastic density currents, where a turbulent head develops radiating elastic energy in the atmosphere, that allows to nicely track the flow evolution through time with an infrasound array (e.g.[Delle Donne:2014, 47, 72]).

4.6.2 Seismo-acoustic coupling of radiated elastic energy

Figure 4.11 shows the mean power spectral density of seismic and infrasound signals for the three debris flow events. This was calculated considering the entire waveforms of Figure 4.3 and by applying spectral analysis

over 10-seconds-long windows with a superposition of 50 %. The PSD of the seismic signals (Figure 4.11 b) is very stable for all events, peaking around 8 Hz, with a spectral amplitude that scales with the recorded discharge rate. The spectrum drops quickly both for low (<3Hz) and high (>20 Hz) frequencies. Based on the model proposed by [56], for seismic noise produced by bed load transport, the frequency content of the seismic spectrum is mostly dominated by the source-to-receiver distance. The observed peak around 8 Hz is in good agreement with the minimum distance of ≈ 500 m to the Illgraben torrent.

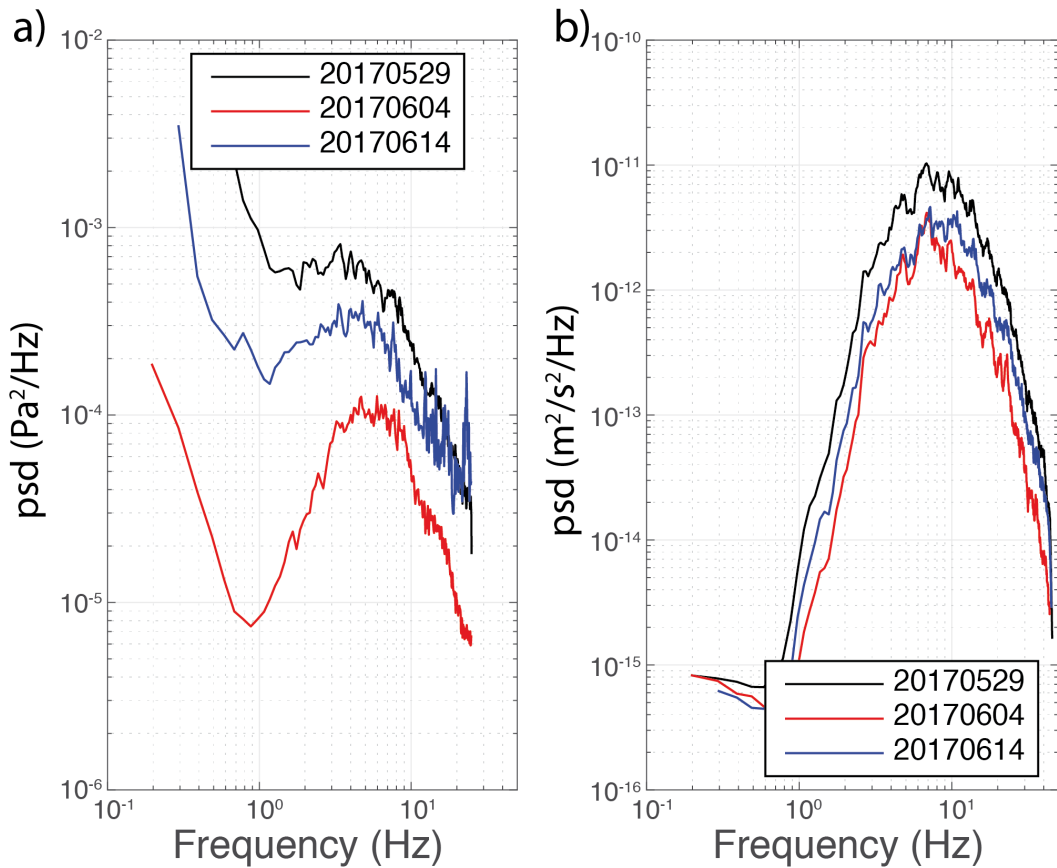


FIGURE 4.11: Power spectral density of infrasound (a) and seismic (b) records of the three debris flow events.

Similarly to what observed for seismic signal, the PSD of recorded infrasound is very stable for the three debris flow events, with a constant frequency content (peaking around 5 Hz) regardless the flow discharge but showing a spectral amplitude that appears to scale with the volume of the flows (Figure 4.11a). In agreement with the modeling of infrasound wave

radiation presented above and with what suggested by [58] for a controlled flow experiment at Grand Canyon, we suggest that the fluid-air interaction such as breaking waves is the most likely source mechanism of elastic energy around 5 Hz. However, unlike what was reported by [58], who observed a spectral coupling between seismic and infrasound records, in our case the seismic and infrasound signals seem to be decoupled.

Such a discrepancy might depend on the different source-to-received distances for the two experiments. In our case, infrasound and seismic data were indeed recorded at a much larger distance from the channel (≈ 500 m) than for the Grand Canyon experiment (≈ 35 m). At such distances, seismic energy produced by fluid-air interaction might indeed undergo a larger attenuation than infrasound. This might explain the lack of the spectral coupling between the two signals, with seismic data only affected by the spectral peak induced by bed-load transport.

4.6.3 Use of infrasound monitoring as an early warning system for debris-flows

Array analysis of continuous infrasound data recorded between May 24 and June 18, 2017, allows identifying the general infrasound activity around the array (Figure 4.12). During this one-month long period, the array processing identified >20000 detections, resulting in coherent infrasound recorded approximately 10 % of the time. This includes the 3 debris flow events as well as additional signals produced by natural and anthropogenic sources of variable strength and duration.

Infrasound excess pressure at the array is generally of low amplitude (<2 Pa), with maximum amplitude recorded during the May 29, debris flow event. Infrasound detections are typically characterized by low values of apparent velocity (>400 m/s), and highlight several persistent sources around the array. Figure 4.12b shows coherent, sustained, infrasound with back-azimuth of ≈ 25 (± 15), 174 (± 3) and 292 (± 2) $^\circ\text{N}$, suggesting the existence of repetitive sources through time. The first cluster of infrasound detections ($B_{az} \approx 25 \pm 15$ $^\circ\text{N}$) is likely related to signal produced within the town of Leuk, located northeast of the array at a distance of ≈ 2 km. Concerning the detections with back-azimuth centered around 174 $^\circ\text{N}$, we suggest they might be consistent with the activity within Illgraben, as it is

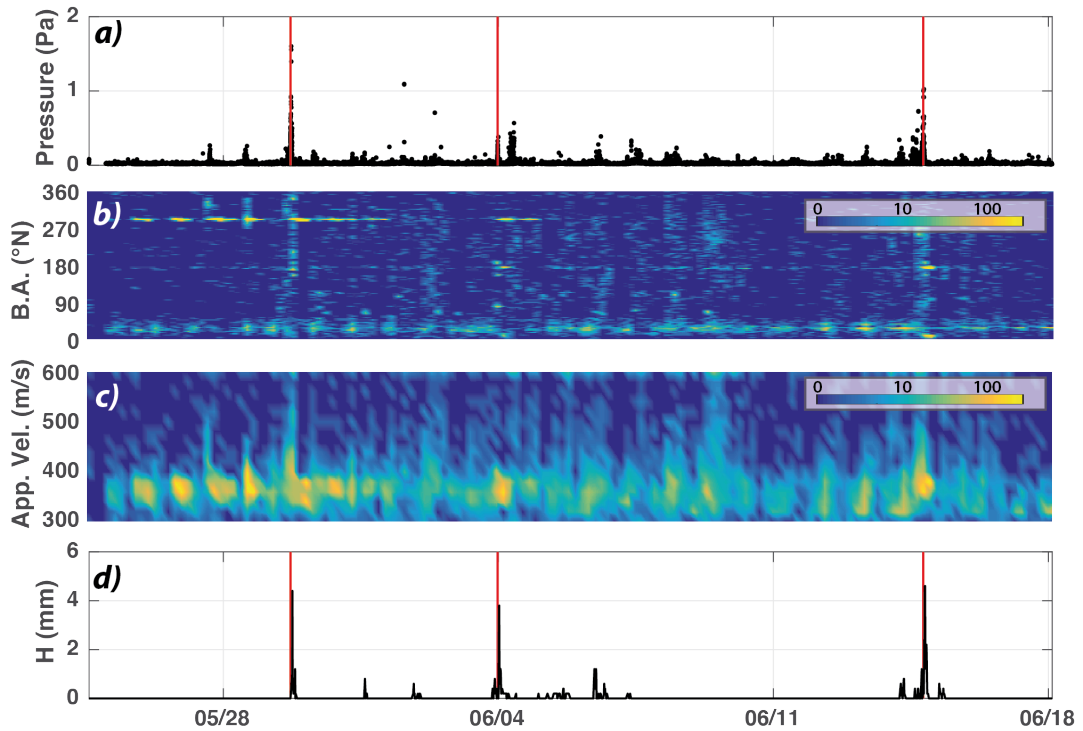


FIGURE 4.12: Results from infrasound array processing between May 24th and June 18th, 2017, showing excess pressure (a), back azimuth (b) and apparent velocity (c) of infrasound detections. Color bars indicate the number of detections every 4 hours. d) Cumulative precipitation (mm) over a time period of 10 minutes. Vertical red lines identify the timing of automatic detection of the debris flow event based on infrasound array analysis (Table 1).

pointing towards the mouth of Illgraben torrent entering the Rohne valley. The last cluster of detections characterized by a back-azimuth value centered at 292°N (Figure 12b) is pointing directly to the dam of the Tseuzier lake, positioned at a distance of 15 km from the array.

Going into the details of the sources driving the different clusters of infrasound detections is beyond the scope of the present work, but a general description of the sensitivity of the infrasound array is required to tune a possible procedure for automatic detection of debris flow events. From Figure 4.8 it is evident that all the debris flow events share a phase of stable detections from the back-azimuth of 155°N , that corresponds to CD16 right at the mouth of the Illgraben (phase 3 in Figure 4.8b). This is preceded by a phase of infrasound detections with a back-azimuth of $\approx 180\text{--}190^\circ\text{N}$ and an apparent velocity ($\approx 400\text{ m/s}$), that we showed reflects the flow at CD1

(phase 2 in Figure 4.8b).

All available infrasound detections obtained for the time period spanning from May 24 to June 18, 2017, have been analyzed looking for clusters of detections showing similar characteristics to the phase 2 and 3 of the debris flow (Figure 4.8b). Eventually only the three debris flow events have been identified without any false alerts during the period of investigation (Figure 4.12). The onset time of the infrasound detections (Table 1) is comparable to timing of the debris flow obtained from the sensors installed at CD1, inside the Illgraben. This is clearly showing that infrasound can be used to monitor and detect efficiently the occurrence of debris flow events at Illgraben torrent. By using infrasound array processing procedure, it is indeed possible to detect the occurrence of an event from a remote location, with a timing that is in quite a good agreement with the timing provided by instrumented CD1 inside the canyon, whose installation, operation and maintenance poses considerable technical challenges.

4.7 Conclusions

In this work we present a seismo-acoustic analysis of debris flow activity at Illgraben torrent, Canton Valais, Switzerland, focusing on 3 debris flow events that occurred in spring 2017 with total volume spanning from 24.000 to 700.000 m³. Infrasound data were collected with a small aperture array, deployed in a forested area on the Illgraben fan in the Rhone valley, easily accessible for deployment and maintenance. Debris flows are recorded as emergent signals of long duration both in the seismic and infrasound record.

Infrasound and seismic data show a stable frequency content peaking around 8 Hz for the seismic and between 3-5 Hz for the infrasound. In both cases, spectral amplitude scales with the flow discharge, with maximum amplitude recorded during the May 29, 2017 debris flow event. Based on the observed frequency content, we suggest that seismic and infrasound likely reflect two separate processes. Seismic is mostly affected by bed load sediment transport, with a constant peak frequency of ≈ 8 Hz mostly controlled by the minimum distance between the flow and recorder of 500 m. Infrasound is most likely produced by waves at the river free surface. Unlike what was observed for a controlled flood experiment at Grand Canyon [58]

we do not observe any significant coupling between seismic and infrasound data.

Infrasound array analysis showed that clear infrasound signal from Illgraben is detected shortly after the flow initiation phase, with infrasound wave parameters indicating a stable source that coincides with the first check dam (CD1), installed within the Illgraben valley at a distance of ≈ 1600 m from the array. Despite not being line-of-sight to the array, the infrasound signal is able to cross the mountain ridge (dashed red line in Figure 4.1) to be recorded at the array, with the effect of topography resulting in a low pass filter (Figures 4.4, 4.6, 4.7,d). A second phase of infrasound detections is recorded when the flow enters the Rhone valley. Again, the stable wave parameters (back-azimuth and apparent velocity) point to a fixed source corresponding to the first check dam immediately outside the Illgraben (CD16). Eventually, no more infrasound detections are recorded despite raising infrasound amplitude.

Based on the stable detections from fixed sources and the lack of detections during the peak amplitude phase of infrasound envelope, we present a model of infrasound radiation by debris flow, in terms of an extended source moving with constant velocity. A synthetic pressure wave is constructed assuming an extension of the flow of 500 m, moving at 10 m/s and radiating 3 Hz pressure wave with random phase from 50 discrete point sources along its length. Consistent with real data, the resulting signal has a spindle shape envelope, of long duration, whose maximum amplitude is recorded when the barycenter of the extended moving source reaches the minimum distance to the array. The variable phase of infrasound radiated by the multiple point sources, despite maintaining the frequency content of recorded signal and contributing to the amplitude, lacks coherence thus preventing infrasound array detections. Such a model appears consistent with the free waves at the water surface, typically showing random phase at the scale of the flow.

The proposed mechanism of infrasound radiation by debris flow is different from other density currents like snow avalanches or pyroclastic density currents. Here a turbulent head develops along the flow radiating elastic energy in the atmosphere, that allows tracking the flow evolution through time with an infrasound array (e.g.[47, 11, 72]).

Although the characteristics of the source prevents array detections, we

showed that discontinuity points of the topography, such as change of slopes or dams, result in stable sources of infrasound clearly detectable by the array. For the specific case of Illgraben torrent, the infrasound array proved to be able to efficiently detect infrasound produced at CD1 (Figure 4.1), without any false alarms. Using the persistent characteristics of recorded wave parameters we showed how the infrasound array could be used to identify remotely, from an accessible location, the occurrence of the flow as early as at CD1, thus representing a valuable system for automatic alarm for debris flow events. For the May 29 event, an even longer precursory phase is clearly identified (phase 1, Figure 4.4), that might extend even more the pre-alert for the flow. The corresponding infrasound wave parameters (back-azimuth and apparent velocity) suggest that it might possibly be produced by the initiation phase of the flow before it reaches CD1, but additional data will be required to further analyze this aspect.

Chapter 5

Modeling the infrasonic sources related to density currents

Contents

5.1	Background	78
5.1.1	Density currents and dam break configuration . . .	78
5.1.2	Box-model	81
5.1.3	Multiphase flow modeling	83
5.2	Numerical simulations	86
5.2.1	The ASHEE code	86
5.2.2	Simulations setup	92
5.2.3	Simulations strategy	95
5.3	Analysis of numerical results	96
5.3.1	Gravity current evolution	96
5.3.2	Generation and propagation of acoustic waves . . .	98
5.3.3	Comparison among different scales and initial condition	104
5.3.4	Dependence of the acoustic frequency from the typical source dimensions	107
5.3.5	Analysis of the numerical configuration	111
5.4	Chapter Conclusions	116

Starting from the geophysical observations reported in Chapter 2, here we explore the inferred relation between the volume of the density currents and the frequency content of the related infrasonic signals. Our main objective is first to understand the interaction between the turbulent dilute part of pyroclastic density currents and the atmosphere and second to find the relationship between the physical parameters of the current and the associated acoustic signal. Then, in this chapter we briefly introduce the commonly adopted theoretical models available in literature to describe the PDCs time evolution before to present the numerical model we used for our simulations as long as our simulation setup. Finally we present our analysis of the numerical results.

5.1 Background

In this section we provide a brief overview about commonly adopted theoretical models available in literature capturing the main features of gravity current phenomena, to which pyroclastic flows belong, and describing their time evolution. The dam-break configuration is examined as simple way to generate a density current and the related condition of validity is discussed. The box model theory is presented as we refer to this theoretical base to discuss our numerical results presented in Sec. 3.3. Then we summarize the principal approaches used to model gravity-driven multiphase flows and we briefly refer to previous studies about acoustic waves modelling for volcanological applications.

5.1.1 Density currents and dam break configuration

As discussed in the introduction (1) to this work, particle-driven gravity currents are important in many geological and environmental settings [2] receiving an increasingly wide attention due to their potentially significant socio-economic impact ([2]; [79]). PDCs are an example of these predominantly horizontal, gravity-driven flow. A typical gravity current has a stratified structure that is composed by a dense basal layer and by an upper dilute and turbulent layer. The leading edge of the gravity current consists of a raised mixing region, the head, intruding the current body into the lighter

ambient fluid. The head is followed by a shallower part, the tail, in which is concentrated the bulk of fluid as shown in the schematic representation of 5.1.

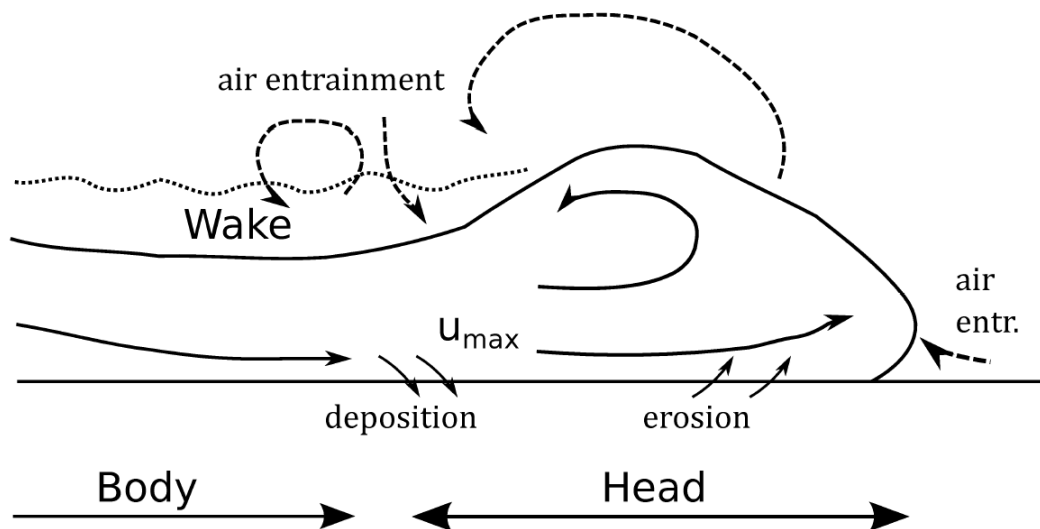


FIGURE 5.1: Schematic representation of the pyroclastic density current structure (modified from [80]).

The heavy fluid from the fore part of the head is rejected into large counter-clockwise vortex mixing with the lighter ambient fluid in a process referred to as "entrainment". These eddy structures are attributable to a Kelvin-Helmoltz instability at the upper interface between the fluids 5.1.



FIGURE 5.2: Evolution of an experimental gravity current from [81].

In order to study the spatio-temporal evolution of gravity currents, the paradigm of the so-called dam-break problem can be considered. We select this simplified configuration because we want to study the fundamental

acoustic behaviour of gravity currents. This prototype problem concerns the sudden release of a fixed volume of fluid from an enclosed lock into an ambient one (Fig. 5.3). It has been extensively investigated both theoretically and experimentally in the past (e.g. [43]; [82]; [83]). The experiment can be prepared both in the axisymmetric and planar configuration. We focus on the latter case, where the dynamics is mostly two-dimensional and a symmetry along the "y" axis (see Fig. 5.3) can be assumed.

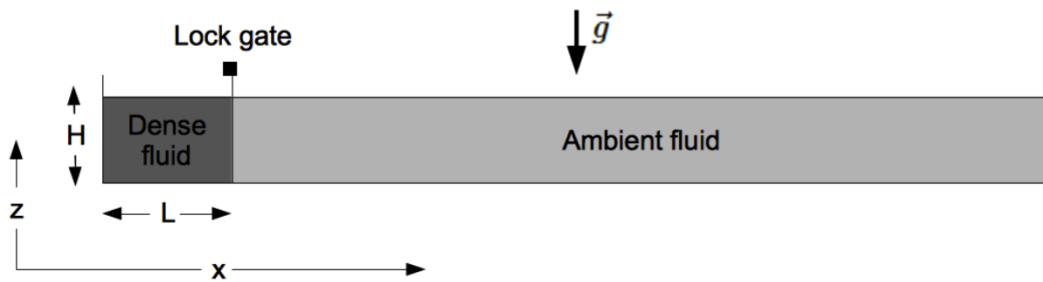


FIGURE 5.3: Initial condition of a dam-break setting.

The propagation of a gravity current initiated in a dam-break configuration shows three distinct flow regimes following the first collapse phase ([84]; [85]). These different regimes identified experimentally are characterized by different time dependence of the advance of the flow front (5.4) as described by [86]:

1. the initial *slumping phase*, controlled by the release conditions and geometry, in which the pressure gradient balances the fluid inertia such that

$$\frac{dx}{dt} \sim \text{const.} \quad (5.1)$$

2. In the second *inertial phase*, the flow dynamics are primarily controlled by the balance between inertia and buoyancy forces in the head. Velocity decreases in time in a way such that the Froude number is conserved (see Eq. (5.6) below), implying:

$$l \sim t^{\frac{2}{3}} \quad (5.2)$$

3. The final *viscous regime* is characterized by the effects of the viscous stress between the current and the bottom wall, controlling the last stage of the flow evolution as

$$l \propto t^{\frac{1}{5}} \quad (5.3)$$

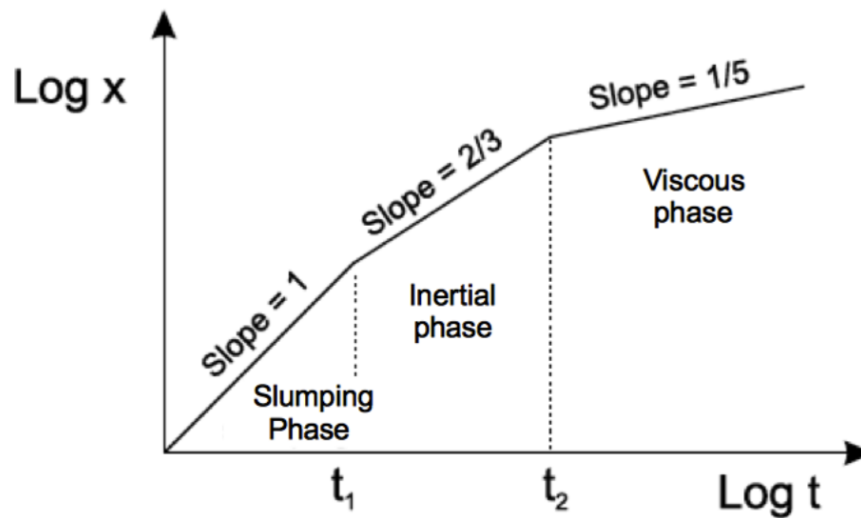


FIGURE 5.4: *Dynamical regimes of the current head evolution in an horizontal dam-break [86]*

Experimental studies show that the dam break initial condition generates a flow where the most of the turbulent kinetic energy is concentrated in the head of the flow. More complex initial condition can create a different dynamics, where energetic large eddies are present as pulses in all the current [87]. This is the typical natural behavior of pyroclastic density currents. However, even in the complex natural case, the head motion can be described as a first approximation by considering the Froude number of the head.

5.1.2 Box-model

The front dynamics and thus the dependence of its position, velocity and height on time, in the inertial phase of motion, is quite well described by a simplified system of ordinary differential equations usually referred to as *box-model*. The *box-model* ([88]; [89]; [84]; [2]) assumes that a gravity current is propagating as a consequence of the density contrast between the current and the surrounding fluid, keeping the Froude number approximately

constant. The density contrast is usually expressed introducing the reduced gravity, g' , defined as:

$$g' = g \frac{\rho_c - \rho_0}{\rho_{ref}} \quad (5.4)$$

where ρ_c is the density of the current, ρ_0 is the density of the ambient fluid and ρ_{ref} is the reference density to be chosen accordingly to the characteristics of the simulated flow and background. In this simplified theory the flow is assumed to be homogeneous and in the incompressible Boussinesq non-dissipative limit ($\rho_c - \rho_0 \ll \rho_0$). The density and the volume of the body are assumed constant, so that g' and A can be prescribed by the initial conditions. Here the volume of the current is prescribed by its area in the xz plane, $A = l \cdot h = l_0 \cdot h_0$, where $l(t)$ is the position of the head, $l(0)$ is its initial value, and $h(t)$ is the height of the body. The reduced gravity can be considered constant as long as particle settling is minor. Under these assumptions, the model writes:

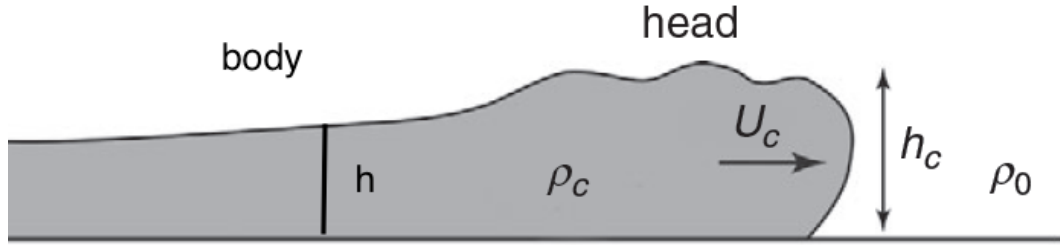
$$\begin{cases} u = \frac{dl}{dt} = Fr(g'h)^{\frac{1}{2}} \\ lh = l_0 h_0 = A \end{cases} \quad (5.5)$$

Where $l(t)$ represent the front position, u is the velocity of the body, A is the 2D volume of the current and Fr is the dimensionless quantity called Froude number, the ratio of inertial to buoyancy forces, defined as:

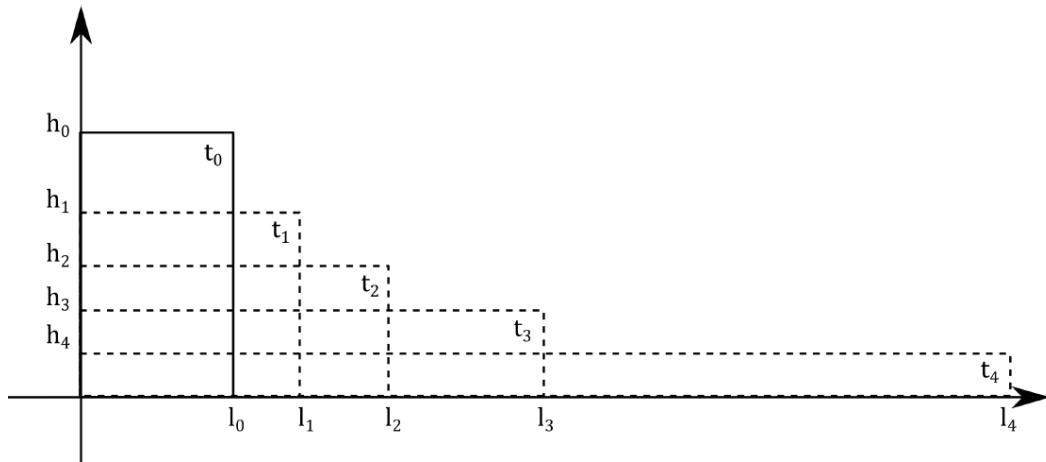
$$Fr = \frac{u}{(g'h)^{\frac{1}{2}}} \quad (5.6)$$

For a current flowing with no energy dissipation between the fluid layers Fr is a constant with the theoretical value of $\sqrt{2}$ ([88]; [89]). Experimental studies measured Fr number values ranging between ~ 1.2 and ~ 1.4 due to dissipative effects [84].

In the early slumping phase as in the final viscous stage of motion, the model is not a good approximation of a gravity current. Between these two phases the inertial regime holds with. This regime is controlled only by two parameters, g' and A . In such conditions, the system of Eq. (5.5) can be integrated from time $t = t_0$ (beginning of the inertial phase), obtaining the evolution of the front position and the current height in time.



(a)



(b)

FIGURE 5.5: Sketch of an inertial gravity current (Top). Box-model geometric assumption of volume conservation with time (bottom). Modified from [4].

$$l^{\frac{3}{2}} = l_0^{\frac{3}{2}} + \frac{3}{2} Fr (g' A)^{\frac{1}{2}} (t - t_0) \quad (5.7)$$

We can see from Eq. (5.7) that the front propagates in time as $l \sim t^{\frac{2}{3}}$, as observed in experiments. It is worth noting that the height of the body can be different from the height of the head. For example, in our experiments the shape of the current head has a nearly constant height, while that of the body decreases with time.

5.1.3 Multiphase flow modeling

Given their hazardous nature, numerous conceptual and numerical models of PDC exist in order to explore their internal dynamics and behaviour.

Each model formulation is a simplified description of the natural phenomena, and a large diversity of models and numerical simulations have been developed in last decades with the basic concept to solve conservation equations for mass, momentum, and energy. However, we can schematically categorize this PDC models in three main types (see [90]): (1) dilute, box model approaches, (2) depth-averaged, concentrated flow models, and (3) multiphase models (Fig. 5.6).

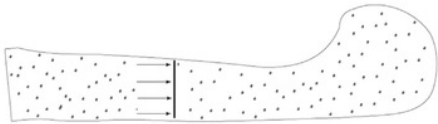
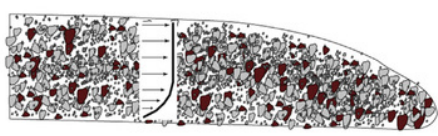
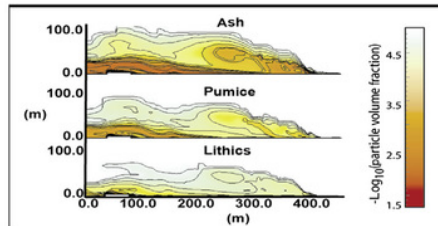
	<p>Dilute, 1D models</p> <ul style="list-style-type: none"> -Turbulent, homogeneous flows (particles suspended by turbulence) -Front condition given by constant Froude number
	<p>Depth-averaged coulomb models</p> <ul style="list-style-type: none"> -Thin, concentrated flows -Frictional interaction at the bed controls flow motion
	<p>Multiphase models</p> <ul style="list-style-type: none"> -Separate conservation equations for multiple particle types -Drag between the gas and particles transmits momentum between phases

FIGURE 5.6: Simplified classification of PDC models from [90].

Simplified integral models, such as the dilute, box model approach described in the previous section, represent detailed quantitative methods to describe the thickness and the kinematics of the pyroclastic density current head. This approach, even if used as reference for the tracking of the flow front progression in time respect to other models and numerical simulations, is oversimplified as it cannot take into account density variations, sedimentation, air ingestion as other internal dynamics characterizing real PDCs in nature. However, despite the large simplifications, this model reproduces well the evolution of the head position.

The depth-averaged models are obtained from depth-integrating the Navier-Stokes equations in the approximation that the flow depth is much smaller than the horizontal scale of motion. In the depth-averaged method, meshes

can be thought as columns and all the physical properties are vertically averaged and three-dimensional equations vertically integrated. These kind of models are widely used on complex topographies, to study how the invasion area of the flow is influenced by valleys and heights.

However, since PDCs are characterized by a multiphase nature, multiphase models, that do not require depth-averaging, have been developed thanks to the significant increases in computational power. These fully multiphase codes solve for separate dynamics equations for different particle phases describing mechanisms of particle interaction and resistance to flow motion during PDC transport more accurately [91, 92].

Limits to the use of this approach are placed by the large computational demands needed, while the integral and depth-averaged methods discussed above can generate results very rapidly. The speed of calculation acquires great importance for real-time hazard assessment, as the estimation of flow volumes, flow rates and initial velocity is generally very difficult during a volcanic crisis.

In this work we use a multiphase model for pyroclastic density currents able to capture the important features which characterize the flow dynamics (such as non-equilibrium dynamics of solid particles and turbulence). The model solves the compressible Navier Stokes equations, thus it is able to manage both the pressure fluctuations generated by the flow (acoustic source) and the propagation of these perturbations into multiphase mixtures (acoustic propagation).

Acoustic source models for PDCs are basically unknown and this is the first study which attempt to analyse the acoustic signal produced in numerical simulations of density currents propagation. Our aim is to improve infrasound technique by mean of the physical modelling finding relations between the direct geophysical measure and some important flow characteristic. Potentially, these kind of relations could be used for rapid evaluation of pyroclastic flow hazards.

5.2 Numerical simulations

In this section we describe the numerical approach adopted in order to efficiently simulate the dynamic evolution of the density current with time, the relations with the initial conditions and, at the same time, the generation and propagation of acoustic waves in atmosphere. Firstly we present the selected code ASHEE exploring the main assumptions behind the model and its strengths by reference to our aims and purposes. Then we describe our simulations setup discussing the numerical solutions adopted and the associated boundary conditions. Finally, we report the different variables and parameters to be changed in our numerical experiments in order to study the dependence of the acoustic signal from these controlling parameters.

5.2.1 The ASHEE code

A new fluid-dynamic model has been recently proposed in literature (see Cerminara et al., 2016 [92, 93, 94], for details) to numerically simulate the kinematic non-equilibrium dynamics of polydisperse gas-particle mixtures forming volcanic plumes and PDCs.

The new developed three-dimensional numerical code, which is called ASHEE (ASH Equilibrium Eulerian), is able to resolve the spatial and temporal scales of the interaction between gas and particle in turbulent regime. It generalizes the equilibrium–Eulerian model by [95] to the compressible two-way coupled regime. The equilibrium–Eulerian model is an extension of the dusty gas model written to take into account particle kinematic decoupling, retaining the numerical advantages and simplifications of dusty gas one. Assuming the multiphase mixture composed by a carrier fluid of i chemical components and by a dispersed phase of j classes of solid particles, the constitutive equations for the model write as follows

$$\partial_t \rho_m + \nabla \cdot (\rho_m \mathbf{u}_m) = 0 \quad (5.8)$$

$$\partial_t (\rho_m y_i) + \nabla \cdot (\rho_m \mathbf{u}_g y_i) = 0, i \in I \quad (5.9)$$

$$\partial_t (\rho_m y_j) + \nabla \cdot [\rho_m (\mathbf{u}_g + \mathbf{v}_j) y_j] = 0, j \in J \quad (5.10)$$

$$\partial_t(\rho_m \mathbf{u}_m) + \nabla \cdot (\rho_m \mathbf{u}_m \otimes \mathbf{u}_m + \rho_m \mathbb{T}_r) + \nabla p = \nabla \cdot \mathbb{T} + \rho_m \mathbf{g} \quad (5.11)$$

$$\begin{aligned} \partial_t(\rho_m h_m) + \nabla \cdot [\rho_m h_m (\mathbf{u}_m + \mathbf{v}_m)] = \partial_t p - \partial_t(\rho_m k_m) - \nabla \cdot [\rho_m k_m (\mathbf{u}_m + \mathbf{v}_K)] + \\ \nabla \cdot (\mathbb{T} \cdot \mathbf{u}_g - \mathbf{q}) + \rho_m (\mathbf{g} \cdot \mathbf{u}_m) \end{aligned} \quad (5.12)$$

Where the equations of conservation of momentum and energy consider respectively the velocity field of the mixture, \mathbf{u}_m , and the mixture temperature, T , while the mass balance law consider I equations for each gas phase, with all the gas phases move with the same velocity field (\mathbf{u}_g), and J equation for each particle class, where each solid phase has its velocity field (u_j). The model is driven by the assumption that the particle velocity field u_j can be seen as equal to the gas velocity plus a decoupling velocity, depending on the Stokes time, the carrier fluid acceleration and the gravity:

$$u_j = u_g + v_j \quad (5.13)$$

In this way, the model takes into account particle settling and preferential concentration. The mixture velocity field u_m is defined through the mass weighted average:

$$u_m = \sum_{i \in I} y_i u_g + \sum_{j \in J} y_j u_j \quad (5.14)$$

The two mass fractions y_i and y_j are defined as the ratio between i -th or j -th phase bulk density and the bulk density of the mixture: $y_i = \rho_i / \rho_m$, $y_j = \rho_j / \rho_m$. The mixture bulk density is defined as $\rho_m = \rho_g + \rho_s = \sum_i y_i \rho_i + \sum_j y_j \rho_j$ so that $y_g + y_s = \sum_i y_i + \sum_j y_j = 1$. In the set of balance equations above \mathbf{f}_j and \mathbf{q} are the drag force per unity of volume acting on the j th particle class and the fluid heat flux respectively, while \mathbb{T} represent the stress tensor field. \mathbb{T}_r is defined as $\mathbb{T}_r = \sum_{j \in J} (y_j \mathbf{v}_j \otimes \mathbf{v}_j) - \mathbf{u}_r \otimes \mathbf{u}_r$.

Turbulence is a multiscale physical phenomenon involving many different scales, from the large scale of the flow domain to the scale of the smallest

eddy of the turbulent cascade. Direct Numerical Simulations (DNSs) simulating the whole range of spatial and temporal scales in the turbulent flow are hardly computationally affordable, and just unaffordable for flows at geophysical scale. For this reason the PDEs of the ASHEE model have been filtered to reduce the range of time- and length-scales that are being solved, adopting the Large Eddy Simulation (LES) approach. Such a low-pass filtering effectively removes small-scale information from the numerical solution separating the large scales from the subgrid scales, preserving the characteristics of the energy cascade of turbulence. Indeed, non linearity causes the coupling between the large and the small scales, introducing subgrid-scale (SGS) terms that cannot in general be disregarded. To mimic the SGS effect on the large scales, reproducing correctly the resolved turbulent spectrum, SGS models take advantage of the universal character of turbulence at the smallest scales (Kolmogorov theory see e.g. [96, 97, 98]).

In particular, in our case, a series of dynamic SGS models have been selected in order to use the spectral information contained into the resolved fields to automatically quantify the constants appearing in the LES model. This model is actually the one which has been discretized following a strategy discussed later in this subsection.

Given the equations presented above, the main hypothesis behind the model may be summarized as follows:

- The particulate phase is dilute, i.e. $\epsilon_j < 10^3$. This means that particle–particle interactions can be disregarded.
- The stress terms are neglected in the solid phase in the approximation of dilute regime and the gas components are Newtonian fluids with dynamical viscosity either constant or described by the Sutherland law.
- particles are much more heavier than the carrier fluid ($\hat{\rho}_s \gg \hat{\rho}_g \gg 1$). The model enables the description of mixtures with a high mass load of solid particles (two-way coupling).
- Particles dimension is smaller than 1 mm, so that Stokes $St < 0.2$. Bigger particles could be considered using the Lagrangian method. The particle relative Reynolds number is smaller than 10^3 .

All the main hypothesis behind the model are verified in the turbulent dilute part of a density current. Additional details on the model formulation can be found in [92, 93, 94].

We select the ASHEE code to study via numerical simulations the interaction of the turbulent dilute part of pyroclastic density currents with the atmosphere and the related production of sound waves. The code enables to simulate directly the source of the atmospheric pressure disturbance, simulating the density current dynamic, and then to study the propagation in atmosphere of this disturbance as sound waves.

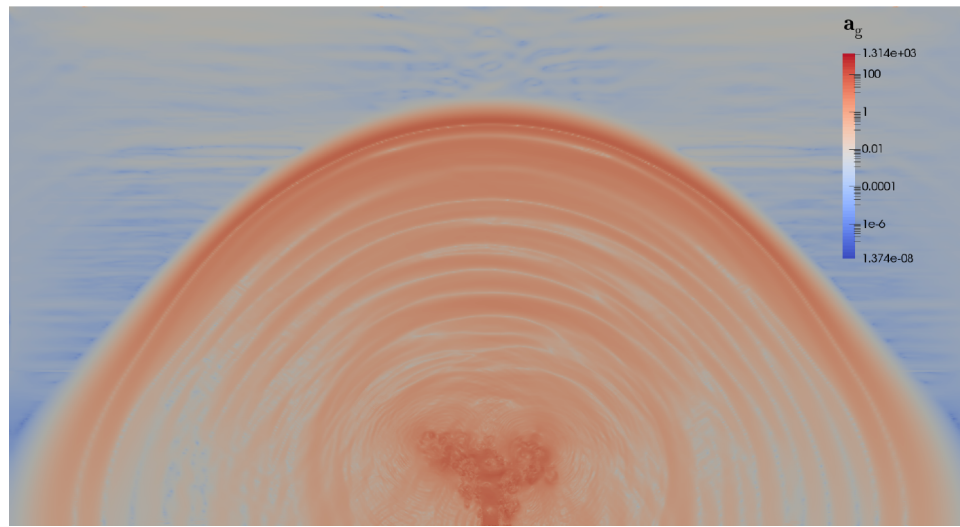
In fact, pressure perturbations are described from the equations of the model [94] with speed of sound:

$$c = \left(\frac{\partial p}{\partial \rho_m} \right)_{isoentropic}^{\frac{1}{2}} = \sqrt{\frac{\gamma_m P}{\rho_m}} \quad (5.15)$$

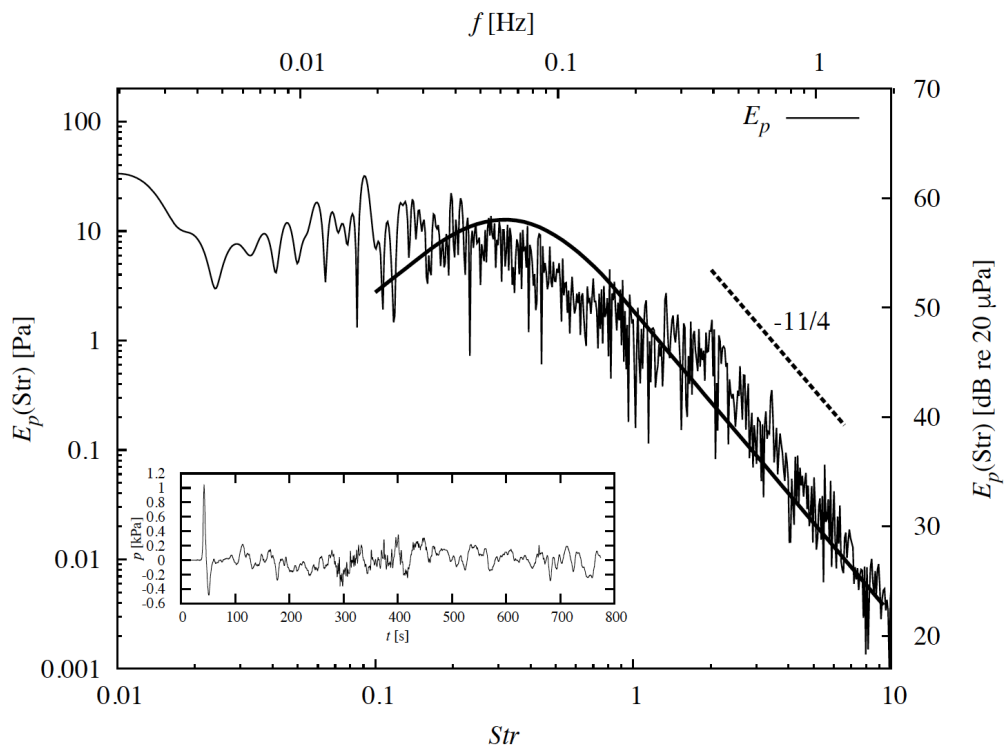
Where the speed of sound of a gas-particle mixture decreases with respect to that of the carrier gas phase (air in our case) because of the mixture density ρ_m increases and the ratio between the specific heat at constant pressure and constant volume, γ_m , decreases because of the presence of the solid particles.

The three-dimensional compressible equilibrium–Eulerian model is discretized and numerically solved to obtain a time-dependent description of all independent flow fields with prescribed initial and boundary conditions by using the unstructured, finite volume (FV) method based open source C++ library OpenFOAM. This numerical infrastructure released under the Gnu Public License (GPL) is well integrated with advanced tools for pre-processing (including meshing) and post-processing (including visualization) and a number of existing solvers can be modified in order to create new solvers (e.g., to solve a different set of equations) and/or to implement new numerical schemes. The new solver implemented by [92] is called **ASHEE**. In the FV method [99], the governing partial differential equations are integrated over a computational cell, and the Gauss theorem is applied to convert the volume integrals into surface integrals, involving surface fluxes.

Reconstruction of scalar and vector fields (which are defined in the cell centroid) on the cell interface is controlling both the accuracy and the stability properties of the numerical method. OpenFOAM implements a wide choice of discretization schemes. For our simulations we have used a second order scheme for spatial interpolation, in particular, we used a central bounded scheme with the Sweby [100] limiter applied to all terms in the two-dimensional simulations. When the simulation is three-dimensional, the nonlinear advection terms are not limited in order to minimise the numerical diffusion and reproduce the 3D turbulence spectrum of the largest eddies. Temporal discretization is based on the second-order Crank-Nicolson scheme as result of different tests with different schemes. We found that a first-order scheme is not enough to efficiently simulate the dynamic of generation and propagation of the acoustics waves. The inversion of the algebraic equations deriving from the discretization procedure is based on a segregated solution strategy, in which partial differential equations are solved sequentially and their coupling is resolved by iterating the solution procedure. In particular, for Eulerian fluid equations, momentum and continuity equation are solved by adopting the PISO (Pressure-Implicit with Splitting of Operators) algorithm. The PISO algorithm consists of one predictor step, where an intermediate velocity field is solved using pressure from the previous time-step, and of a number of PISO corrector steps, where intermediate and final velocity and pressure fields are obtained iteratively. The number of corrector steps used affects the solution accuracy and usually at least two steps are used. To conclude, after the general presentation of the the ASHEE code and solver we would like to highlight that the model has been tested verified and validated against a number of well understood benchmarks and experiments, demonstrating itself capable not only to capture the key phenomena involved in the dynamics of volcanic ash plumes and dilute density current, such as turbulence, mixing, heat transfer, compressibility, preferential concentration of particles, entrainment, but also to well reproduce the main features of the infrasonic signal related to these phenomena. In fig.5.7 is shown the sound produced by the turbulent eddies of a strong plume simulated with ASHEE and the spectrum of the related infrasonic signal probed at the ground level, 15 km far from the vent in the computational domain [94].



(a)



(b)

FIGURE 5.7: *a)* Infrasonic signal generated by the turbulent eddies. Here the infrasonic perturbation is visualized by using the magnitude of the field of acceleration a_g (m/s^2), in logarithmic colour scale, after 120 s since the eruption started (from [94]). *b)* The pressure fluctuation data probed at the ground level, 15 km far from the vent. The resulting spectrum is compared with the similarity spectrum generated by large-scale turbulence measured by Tam et al., 1996.

The resulting spectrum is compared with the similarity spectrum generated by large-scale turbulence measured by [101]. The fit is in satisfactory agreement and comparable with results obtained from direct volcanic observation [102]. Following on from what discussed above we selected and used the ASHEE code for the numerical simulation presented in this work.

5.2.2 Simulations setup

PDCs motion is mainly characterized by a regime where inertia and buoyancy forces are balanced and, in many cases, is approximately two-dimensional due to propagation on slopes (such that spreading of the current occurs predominantly in the downslope direction) or to confining topography such as valleys. In this section, we describe the setup for our numerical experiment, considering two-dimensional, inertially dominated gravity currents. The effect of the third dimension is explored beside a variety of different numerical and physical configurations. We report the results of this sensitivity analysis in section 3.3. Here we describe the general setup used for the simulations presented in this work and in particular we describe the mesh and collapsing volume dimension referring to the case we have chosen as standard (see Section 3.3).

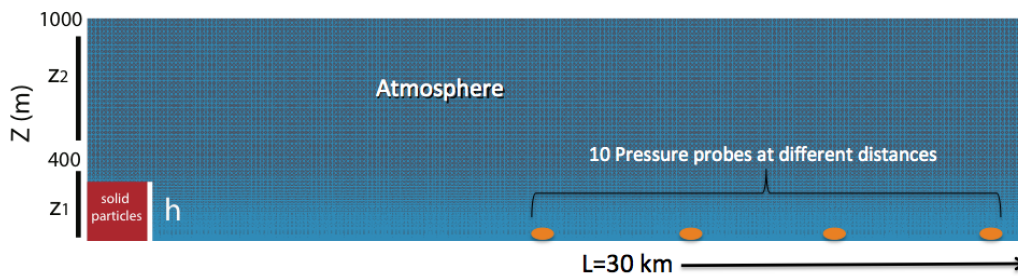


FIGURE 5.8: Configuration of the dam break problem and setup of the computational domain.

The configuration of the dam break problem is illustrated in Fig. 5.8. The width and the length of the computational domain are $Z = 1$ km and $L = 30$ km, respectively. The resolution of the computational domain has been chosen in order to well represent the dynamics of the density current and to fully resolve the typical wavelength, λ , of the related infrasonic signal. From what measured with acoustic sensors in the field, we know that the maximum frequency of the signal related to PDCs and snow avalanches events

is few Hertz. Thus we chose $\delta x = 20$ m and $\delta z = 3$ m resolution for the minimum cell of our mesh respectively in the X and Z direction. This resolution ensures to sample several times (> 10 , following the sampling theory) the wavelength of the expected signal along its propagation direction. We found that $\delta z = 3$ m is appropriate to well describe the dynamics of the head of the current and its main features.

The computational mesh is divided along the Z direction in two sections. The lower section, up to $z_1 = 400$ m, is at higher resolution with a grading applied to the mesh cells, which follows a geometric progression for the cell size. Within this section the cell size increases from 20×3 m close to the bottom of the mesh to a 20×20 m dimension reached at a height of 400 m. In order to reduce the computational cost, the second section along the Z direction, z_2 , has a lower resolution with a 20×20 m stable cell size from an height of 400 m to the end of the computational domain at 1000 m. Along the X direction, the cell size remains constant. The background fluid is set to be air and all the solid particles at the initial time $t = 0$ are enclosed in the $2D$ volume of 10^5 m², with aspect ratio of 1 and thus with an height, $h \simeq 316$ m.

Considering the computational domain described above, we applied the following boundary conditions. Along the **bottom wall** $Z = 0$, a no-slip boundary condition is used. As shown in Sec. 3.2.1, this boundary condition is enough to successfully capture the evolution of the gravity current head expected from experiments. The bottom wall is modeled with a zero heat flux boundary condition (thermal insulator). The **side patch** $X = 0$ is modeled as a symmetry plane. The most problematic edge is that along the **atmospheric boundary**, composed by the two planes $Z = Z_2$ and $X = L$. To reduce to the minimum reflections, keeping the boundary conditions relatively simple, we decided to use the Local One-Dimensional Inviscid (LODI) relations (see e.g. [103]). In particular, the pressure on the cell face p_f (with face normal versor pointing outside \mathbf{n}) is evaluated with a mixed Neumann-Dirichlet boundary condition

$$p_f = w p_{\text{ref}} + (1 - w) [p_c + \delta(\nabla p \cdot \mathbf{n})_{\text{ref}}] , \quad (5.16)$$

where p_{ref} is calculated using the LODI relations, p_c is the pressure on the cell center, δ is the face-to-cell distance, w is a fraction balancing the two types of

boundary conditions and $(\nabla p \cdot \mathbf{n})_{\text{ref}}$ is evaluated using the still condition

$$(\nabla p \cdot \mathbf{n})_{\text{ref}} = \rho_m(\mathbf{g} \cdot \mathbf{n}). \quad (5.17)$$

Defining \mathbf{u}_f the velocity on the face, the LODI relations reduce to the following advection equation

$$\partial_t p_{\text{ref}} + a \partial_\ell p_{\text{ref}} = 0, \quad (5.18)$$

where $a = c + \mathbf{u}_f \cdot \mathbf{n}$ is the sound speed with respect to the face. In this equation, the spatial gradient is evaluated using the assumption that the far field p_ℓ at distance ℓ from the face is barotropic with still atmospheric pressure p_{atmo} :

$$p_\ell = p_{\text{atmo}} - \frac{1}{2} \rho_m |\mathbf{u}_f|^2 \quad \text{if } \mathbf{u}_f \cdot \mathbf{n} < 0 \quad (5.19)$$

$$p_\ell = p_{\text{atmo}} \quad \text{if } \mathbf{u}_f \cdot \mathbf{n} \geq 0. \quad (5.20)$$

The value of the fraction w depends from the time discretization. Defining δ_t the time step, $k = a\delta_t/\ell$ and $\alpha = a\delta_t/\delta$ the parameters comparing the space travelled by the wave during one time step respectively with the length scale ℓ and with the face-to-cell distance δ , we use

$$w = \frac{1 + k}{1 + \alpha + k}. \quad (5.21)$$

The velocity field on the atmospheric boundary is evaluated from the pressure, while the temperature assumes the atmospheric value T_{atmo} in case of inflow and the zero-gradient condition in case of outflow. These non-reflecting relations are a generalization of the classical OpenFOAM *wave-transmissive* boundary condition to the case of a stratified atmosphere. This choice is good to deal with our complex dynamics but keeps some reflection depending from the curvature of wave approaching the edge. We have thus to take into account that some reflections can occur and find a way to recognize and filter them in the analysis of acoustic signal recorded from our pressure probes. Given the experimental setup described above, in the next subsection we describe the simulation strategy followed to select the variables to change for different sets of simulations.

5.2.3 Simulations strategy

We use the dam-break setup as it is a simple way extensively used to generate a density current both in laboratory and numerical experiments. Since we are interested in the analysis of the sound waves produced by a developed current, we discard the contribution of the initial collapse (*slumping phase* of motion), that is not properly describing the typical initial conditions of a pyroclastic flow. After this initial phase an inertial regime exists where the only variables in the problem are g' and A , where the Froude number is approximately constant and the shape of the current head has a nearly constant height. We record acoustic waves produced by the current dynamics at different distances along the current path and we explore the dependence of this infrasonic signal from the variables driving the current dynamic. Starting from the standard case described above with characteristic dimension A , firstly we check the ability of the model to reproduce the main features of the density current dynamic and to satisfactorily describe the acoustic signal at different distances. Then, we perform the first set of simulation changing the typical dimension of the current h and scaling the numerical experiments accordingly, to study the dependence of the acoustic signal from the dimension of the moving flow. Moreover, we explore the role of the concentration and of the flow velocity on the production of sound. For a given characteristic dimension we change the reduced gravity g' and thus the concentration of the and velocity of the density current. Finally, we perform a sensitivity analysis to give an estimation of the error due to the numerical assumptions. To resume and conclude, the real scenario is extremely complex and may depend from a number of different key parameters such as grain size (settling velocity), temperature, topographic effects and so on, that in the real case we cannot control. Thanks to the model we can start with the simplest case, controlling the dependence from each parameter and adding complexities step-by-step. Our work mainly considers the dependence of the acoustic signal produced by the density current from:

- Turbulence effects;
- Scaling effects (dependence from the typical dimension of the head of the current, h , and from the $2D$ volume);
- Concentration of the flow and velocity changes.

We report the results of our simulations in the next section.

5.3 Analysis of numerical results

Firstly we analyse the ability of the designed numerical experiment to describe the dynamic evolution of the current. We focus our analysis on the inertial phase of motion, when the current is fully developed, and it shares features with real pyroclastic density currents in nature. In order to test the ability of the model to reproduce the general features of the density current we compare the current run-out with the theoretical model predictions (described in Section 3.1). Then, we test the efficiency in simulating sound waves generation and propagation comparing signals recorded at probes located at different distances ahead the path of the current. In order to compare the dynamic evolution of the current at different scales, a non-dimensional form of the equation of motion is taken into account. Finally, the generation of the acoustic wavefield is explored by varying both numerical and initial conditions.

5.3.1 Gravity current evolution

Our main objective is to study the interaction between the turbulent dilute part of pyroclastic density currents and atmosphere.

We choose as standard case (see Fig. 5.19) an initial collapsing 2D volume of $A = 10^5 \text{ m}^2$ with an aspect ratio $h/l = 1$, which contains particles with diameter $250 \text{ }\mu\text{m}$, clast density 2400 kg/m^3 with initial concentration $\epsilon_s = 3 \cdot 10^{-3}$. These values fully satisfy the main hypothesis behind the model (see section 3.2.1). Presently, we choose to simulate very fine ash particles which thus remain basically in suspension during the analysed phase of motion discarding to evaluate the contribution of the particle settling to the current dynamics and to the production of sound.

Once the ideal membrane that contain all the mass in the initial volume is suddenly removed the particle-driven gravity current starts to propagate along the horizontal plane as shown in Fig. 5.10.

Figure 5.10 shows the time evolution of the simulated density current starting from the initial *slumping phase*. It is worth noting that this first

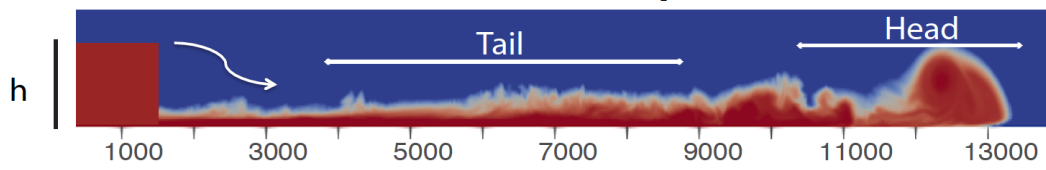


FIGURE 5.9: Schematic representation of the formation of a density current from an initial collapsing volume used in our simulations

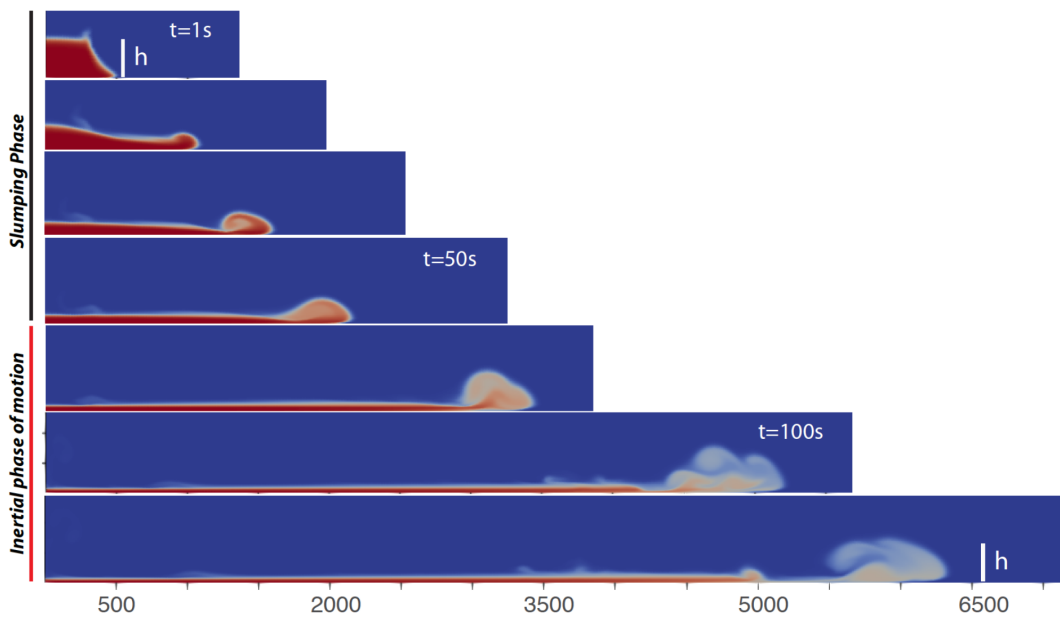


FIGURE 5.10: Time evolution of the simulated density current

phases of collapse and post-collapse slumping are not a good approximation of the pyroclastic flows generation in nature. However we use the dam break setup as it is a simple and extensively used way to generate a density current, both in laboratory and numerical experiments [45]. To avoid misleading interpretation of numerical results we discard from our analysis the initial slumping phase and the related sound waves production, focusing on the following phase when the current propagates inertially.

The current shows all the typical features of an horizontal dam-break front propagation: the head and the tail of the current are easily noticeable, the most advanced part of the front shows the typical nose structure due to the no-slip condition at the boundary, which enables the ambient fluid entrainment under the dense front. The turbulent nature of the current (Figure 5.11) is clearly visible as large counterclockwise vortex due to Kelvin-Helmoltz instabilities at the current-atmosphere interface. As a validation

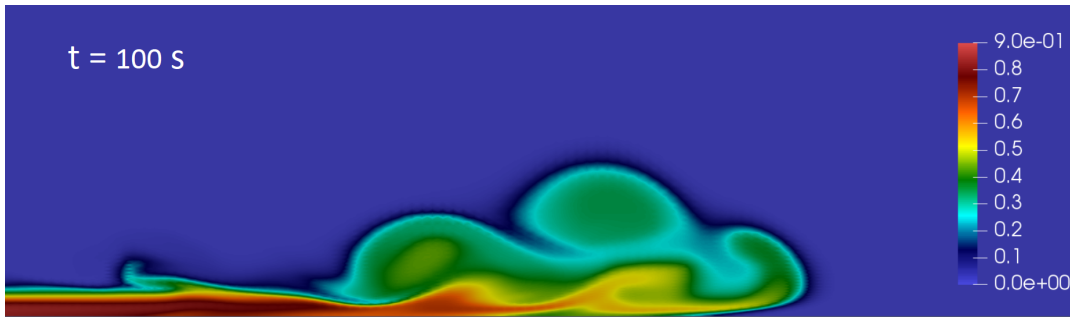


FIGURE 5.11: *Turbulent structure of the current head. The colorbar reports the solid particles mass fraction.*

of the used model, we compare the simulated current run out with the box-model theory prediction (box-model is further described in Section 3.1.2). As shown in fig. 5.12, the simulated flow correctly reproduce the expected linear trend for the front position, $X_f = l$, in the inertial phase.

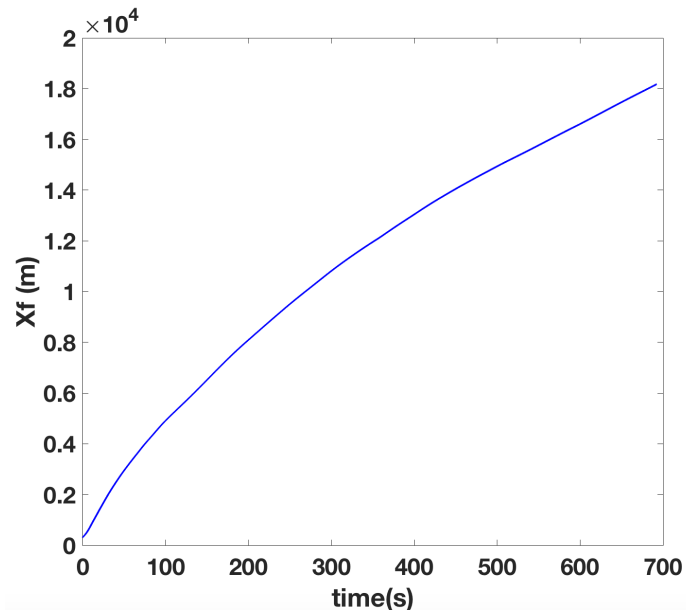
Figure 5.13 shows the shape of the head of the current at different times during its inertial phase of motion. We can see how in this phase the head has a nearly constant height, as expected from the theory (see Section 3.1.2), oscillating around the value of h , which is the height of the initial collapsing volume.

5.3.2 Generation and propagation of acoustic waves

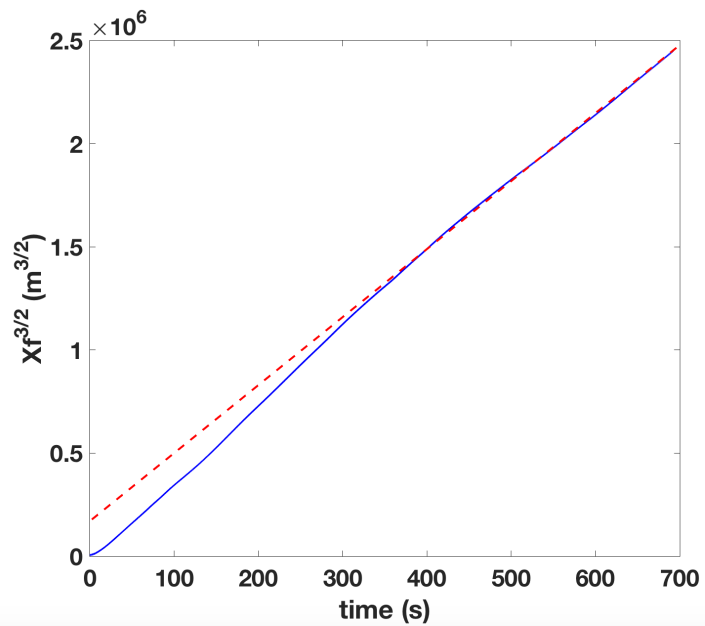
Concerning the analysis of pressure disturbance generated in the background fluid (air in our case) by the current dynamics, it would be useful to visualize the infrasonic perturbation in the whole computational domain, during the density current evolution, as variations of pressure field.

As we can see in Figure 5.14 the pressure disturbances propagate as acoustic waves in the atmosphere. At the beginning of the motion (t_1) large pressure disturbance at low frequencies originates from the collapsing dynamics. Then, once the current is fully developed, the turbulent head clearly becomes the major source of acoustic waves. Such waves, produced by the dynamics of propagating current, show a stable and characteristic higher frequency, compared with the one produced in the initial collapse and slumping phase.

Pressure fluctuation data are probed at the ground level at ten different distances (from 1 km to 29 km far) from the initial volume (Figure 5.15). In



(a)



(b)

FIGURE 5.12: *a) Time evolution of the front position. b) the evolution of $(\text{front position})^{3/2}$, blue curve, in the inertial phase of the current motion after 250 s attains a linear trend as predicted by the box-model theory.*

such configuration, we are able to record the sound emission from the simulated current dynamics in a way that reproduces what is usually done from



FIGURE 5.13: Six time snapshots of the head of the current with a solid particles concentration decreasing with time because of the entrainment process (see colorbar of Fig.5.11). The red dashed line represent the initial height of the 2D volume, h .

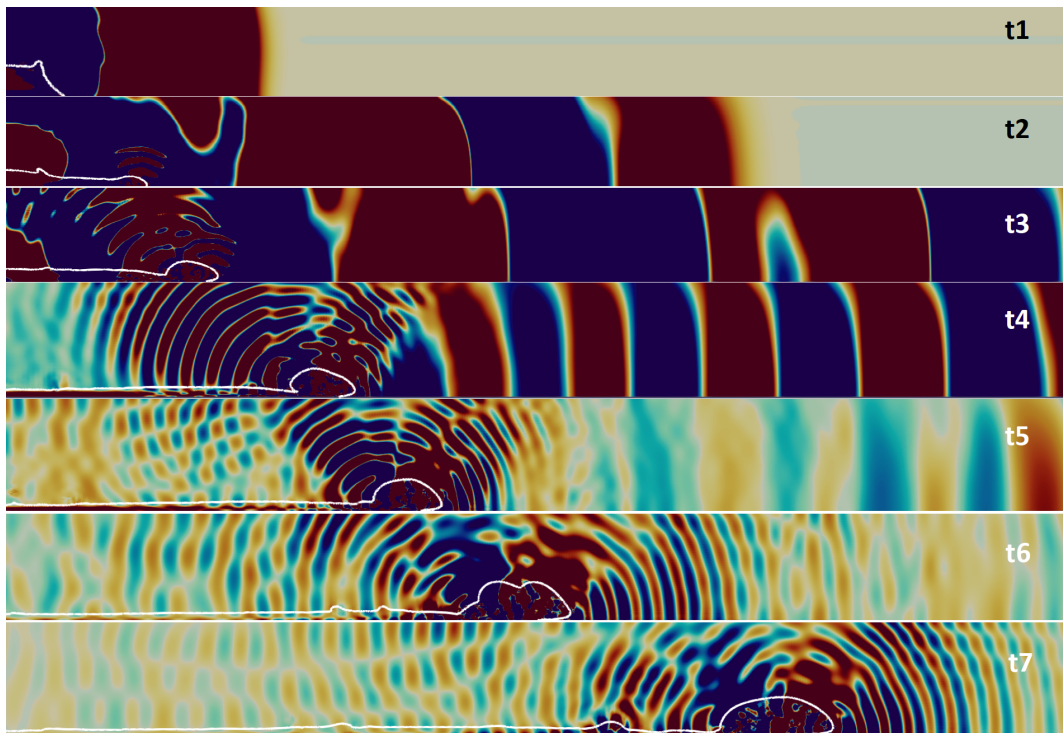


FIGURE 5.14: Sound radiation from the propagating current. The white contour represents the current profile with the 10% of the initial mass fraction. Acoustic waves are visualized as positive (blue) and negative (red) variations of pressure field values measured at two different time steps.

the real microphones in the field. Firstly, we check if the propagation of acoustic waves is well represented by the model comparing signals from the same source recorded at different distances along the current path. Analysis of the amplitude decay at different probes confirms the theoretical geometrical spreading expected for the 2D case:

$$A \propto \frac{1}{\sqrt{r}} \quad (5.22)$$

where the amplitude decaying is inversely proportional to the distance from the source, r .

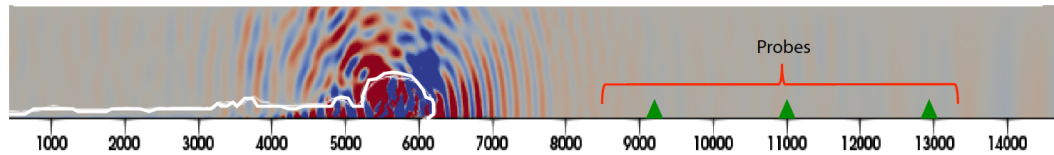


FIGURE 5.15: A snapshot showing the contour of the density current, white line, and the generation of acoustic waves modified to represent in a schematic way our configuration with different pressure probes along the computational domain.

In Figure 5.16 we can see that, once corrected for geometrical spreading, traces from different probes almost perfectly matches. We can also see how this signal recorded after 150 s and referred to the standard case described above in this Section, is characterised by a low frequency content which remains almost unchanged also at large distances, resulting in a very stable waveform.

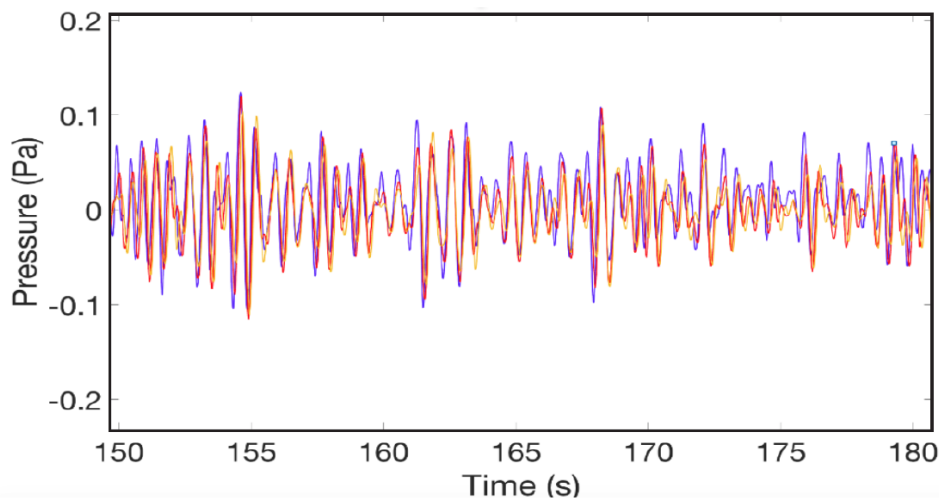


FIGURE 5.16: Three acoustic traces recorded at different distances along the current path and corrected for the source distance following the theory of the geometrical spreading.

Referring to our standard case, we analyse the whole acoustic signal emission recorded ~ 28 km far from the source. A large acoustic signal with an amplitude of about 35 Pa is associated to the initial collapse of the solid material (Figure 5.17 upper plot). Then the signal amplitude significantly

decreases to values of about 0.2 Pa. This lower amplitude signal is related to the inertial phase of the current motion and we can see an enlargement of the acoustic trace between 350 and 600 s in the upper plot of Figure 5.17.

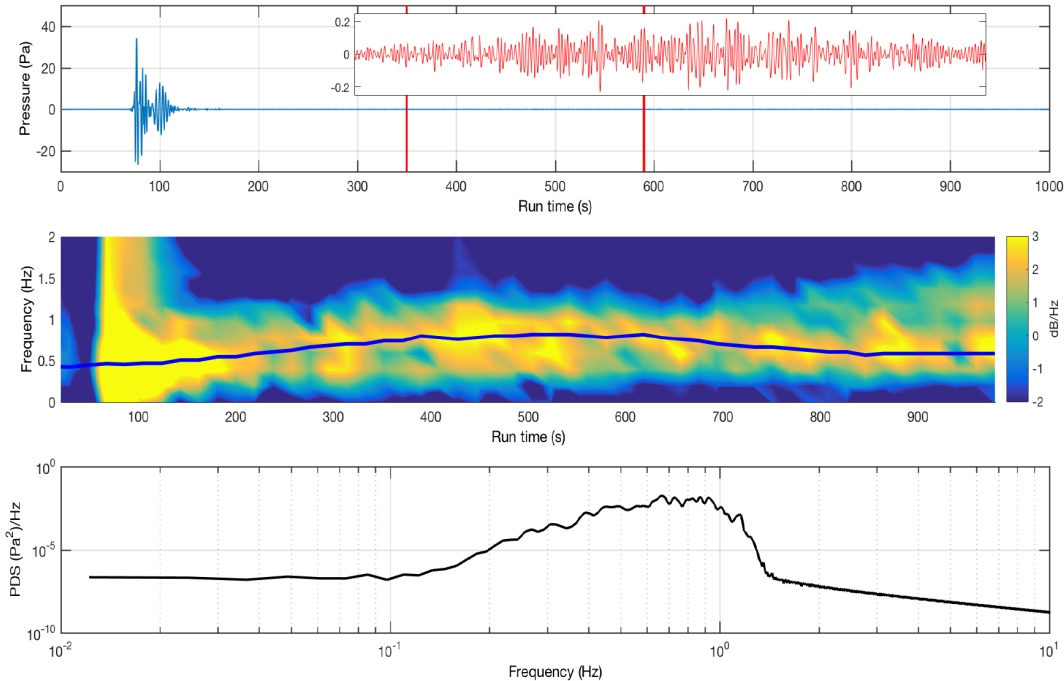


FIGURE 5.17: *The upper plot shows the pressure signal recorded at a distance of ~ 28 km. The enlarged part of the signal of smaller amplitude in the time window between the two red lines is enlarged in the figure. The central figure is the spectrogram of the signal where the blue line represents the value with maximum amplitude in each time window of spectral analysis. The bottom figure is the power spectral density calculated for the red trace in the upper figure.*

Analysis of the frequency content reveals that infrasonic waves, characterized by frequencies below the human hearing, represents the main part of the produced perturbations. In particular the signal is almost confined in a frequency range below 1 Hz, as shown by the power density spectrum (Fig. 5.17, bottom plot). From the spectrogram of recorded signal (Fig. 5.18) we notice that the frequency content remains relatively stable during the whole inertial phase, at an higher frequency respect to the first low-frequency part, produced during the slumping phase of the current.

Since we are interested in the analysis of the sound waves produced by an already developed current, we discard the initial part of the produced

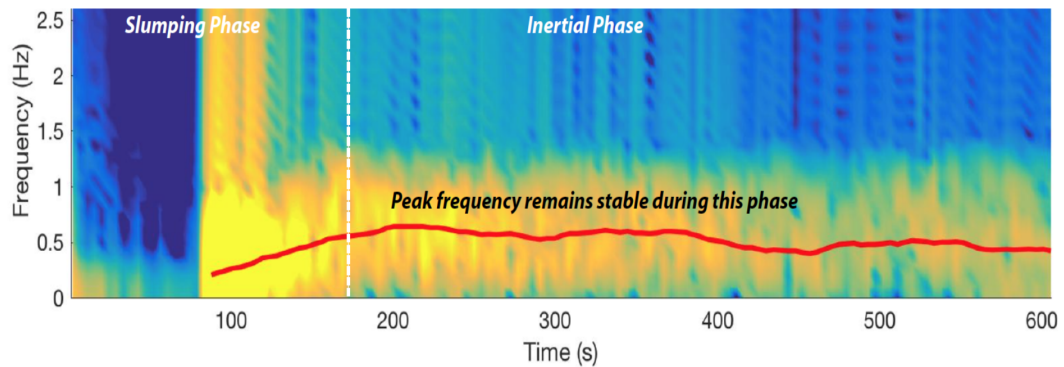


FIGURE 5.18: Spectrogram of the infrasonic signal produced by the evolution of the density current (initial conditions chosen as standard described above in this Section). The red line follows the peak frequency computed for each portion of the signal. We use a time window of 20 s for our analysis with 1 s shift for each computation. White dashed line marks the end of slumping dominated current motion and the beginning of the inertial phase.

signal related to the collapse, that is not properly describing the typical initial situation of a pyroclastic flow. Therefore, we explore the dependence of signal from the initial conditions as shown in the next Subsection.

Among all the observed signal characteristic, we select the signal frequency as the most promising. The reason why we choose to focus our attention on the signal frequency directly follows on from the geophysical observations presented in Chapter 2, where we inferred some dependency of the current dynamics from this parameter. Moreover frequency is much less affected than signal amplitude by wave propagation effects such as the specific topography of the environment and source-receiver distance. This allows to easily compare signals from different density currents recorded at different sites.

5.3.3 Comparison among different scales and initial condition

In order to study the dependence of the infrasonic signal from the current dynamics we vary the initial conditions in two different sets of simulations as summarized in Figure 5.19.

	Typical current dimension	Reduced gravity	fraction of solid particles y_s
Standard case	h	g'	0,90
1 set of simulations	$h/4$	g'	0,90
	$h/2$	g'	0,90
	$3h/2$	g'	0,90
	$2h$	g'	0,90
	$3h$	g'	0,90
	$4h$	g'	0,90
2 set of simulations	h	$g'/4$	0,69
	h	$g'/8$	0,53
	h	$g'/10$	0,47
	h	$2g'$	0,97

FIGURE 5.19: Summary of the strategy followed for different simulation sets. The parameters considered are the characteristic dimension of the current (h), the volume fraction of solid particles in the initial 2D volume (y_s) and the related reduced gravity (g').

Firstly we change the dimensions of the 2D volume (maintaining the original aspect ratio, $h/l = 1$) scaling accordingly all the dimensions of our numerical experiment, such as height and length of the mesh, probes distance, and computation time. This change of the typical dimension, h , of the 2D volume determine a similar change of height of current head during its inertial phase of motion (as shown in the previous Subsection). Unfortunately with this first set of simulations alone we would not be able to isolate the dependence of acoustic signal from the current dimensions. In fact, changes of the collapsing volume size imply changes in the propagation velocity of the density currents. For this reason we run a second set of simulations where we modify the velocity of the generated currents (acting on the initial concentration of solid particles) while keeping constant the

typical head dimension, h , in order to evaluate separately the contribution of velocity changes to the signal.

We perform a scaling analysis to verify the box model approximations and to allow the comparison of our results among all the simulations considered. The current run-outs are reported in Figure 5.20 as function of dimensionless run time, τ , and head position, ξ . Dimensionless time and length scales are computed using the characteristic time of the gravity current, τ_{KH} , and the initial height, h , respectively defined as:

$$\tau = \frac{t}{\tau_{KH}} \quad (5.23)$$

and

$$\xi = \frac{X_f}{h} \quad (5.24)$$

Where $\tau_{KH} = 2\pi\sqrt{h/g'}$ and the reduced gravity g' are computed using a definition chosen to represent the density contrast between the simulated currents and the surrounding fluid. The reduced gravity expresses the effective change in the acceleration of gravity acting on one fluid in contact with a fluid with different density due to buoyancy forces. Recalling Equation 5.4 where the reference density ρ_{ref} has to be chosen accordingly to the characteristic of the simulated flow and background, we can rewrite this equation for sake of simplicity as function of the initial fraction of solid particles (values can be found in Figure 5.19):

$$g' = g \frac{\rho_c - \rho_0}{\rho_{ref}} = g \frac{y_s}{1 - ay_s} \quad (5.25)$$

where changes in the parameter a determine different definitions for g' with a variety of intermediate possibilities between the two end members schematized as follow:

if $a = 0$,

$$g' = g \frac{\rho_c - \rho_0}{\rho_c} \longrightarrow g' = gy_s \quad (5.26)$$

with reference density equal to the density of the current;

if $a = 1$,

$$g' = g \frac{\rho_c - \rho_0}{\rho_0} \longrightarrow g' = g \frac{y_s}{1 - y_s} \quad (5.27)$$

with reference density equal to the ambient density.

We chose an intermediate value $a = 0.7$ to have a reference density that is a blend between that of the current and that of the atmosphere. This value has been chosen as best definition of g' based on the results of the numerical simulations. Indeed, with this normalization, we obtain that the run-outs of all the numerical experiments compare well with the theory (see Fig. 5.20).

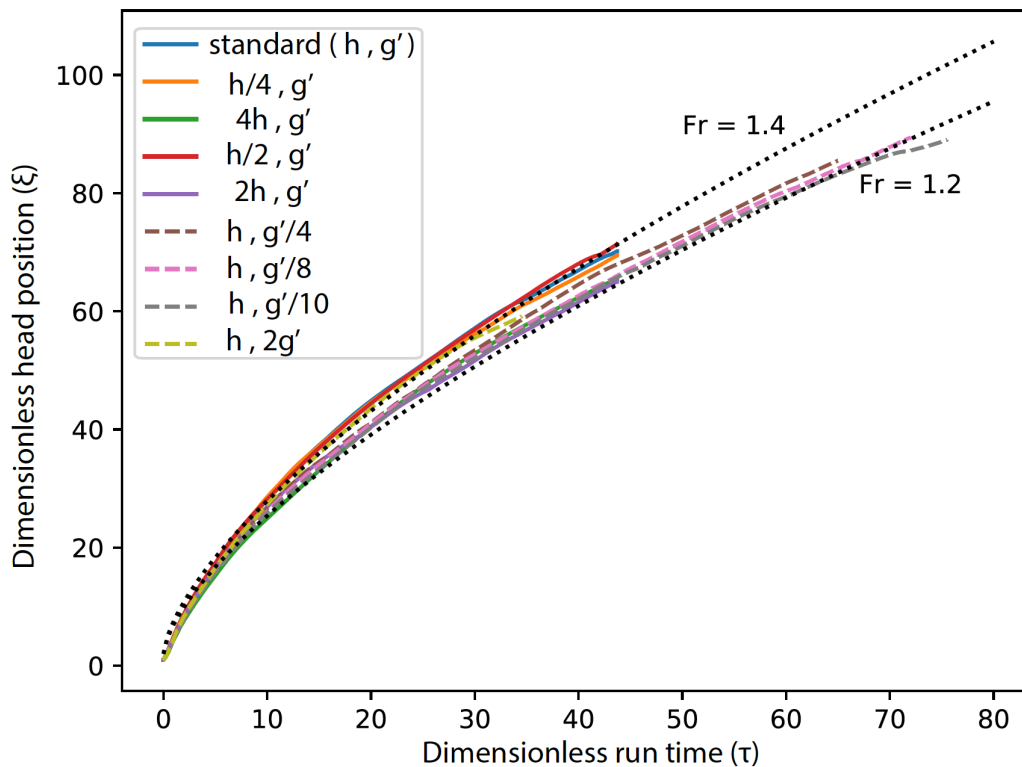


FIGURE 5.20: Propagation of the simulated current expressed in function of the dimensionless run time and head position. Black dashed lines represent the current evolution predicted by the box-model theory for the theoretical Froude number $Fr \sim \sqrt{2}$.

The value of $a = 0.7$ is reasonable considering that we are dealing with a diluted current with well developed mixing zone and with a certain density gradient characterizing the current itself. Therefore, we can see how the propagation of simulated density currents is well approximated by the box-model theory (theoretical values ranging between 1.4 and 1.2 are reported Figure 5.20). Furthermore, the scaling properties explored enable the comparison among the obtained numerical results.

5.3.4 Dependence of the acoustic frequency from the typical source dimensions

Here we report the changes observed in the infrasonic signal and the relations found respect to the initial conditions variation introduced above. As already discussed, we limit our analysis to the stable part of the signal which is produced during the inertial phase of flow motion (Fig. 5.21).

Comparing these signals for all the simulations with different head dimensions, we observe an increase of the signal frequency for decreasing h (Fig.5.22).

Recalling the discussion (Section 3.2.2) about the boundary conditions selected for our simulations, it is important to consider that some reflections of acoustic waves can occur, affecting the frequency content of the recorded signal. In order to correctly evaluate the spectral content of our infrasonic signals produced during the inertial phase, we must take into account possible reflections of the initial large pressure disturbance resulting from the slumping phase. Analysing the spectrograms, we already noticed that this first part of the signal is always characterized by a lower frequency content respect to the following part (see Sec. 3.3.2 and Fig. 5.21). This enables us to recognize the frequency contribution of this phase, which is out from our analysis because the signal produced by the sudden collapse of the initial volume is not comparable with what measured in the field during pyroclastic density currents events. Luckily, the pressure signal produced by the fully developed density current dynamic, can be easily distinguished from possible reflections by comparing the spectral content of the two different portions of the signal (Fig. 5.23).

Once verified the effect of reflections we filter out this contribution from our signals, for each simulation, to select the proper main frequency peak value, which can be considered as characteristic for the selected initial conditions. Figure 5.24 shows the spectral contents for the first simulation set.

The first set of simulations shows that the frequency content shifts accordingly with changes of initial h values. Considering that we are dealing with a moving source we evaluate the contribution of the Doppler effect on the frequency of the recorded signal. Among all the simulations performed, we compute the frequency shift expected for the faster propagating flow (the one with the larger initial typical dimension, $4h$) obtaining maximum error

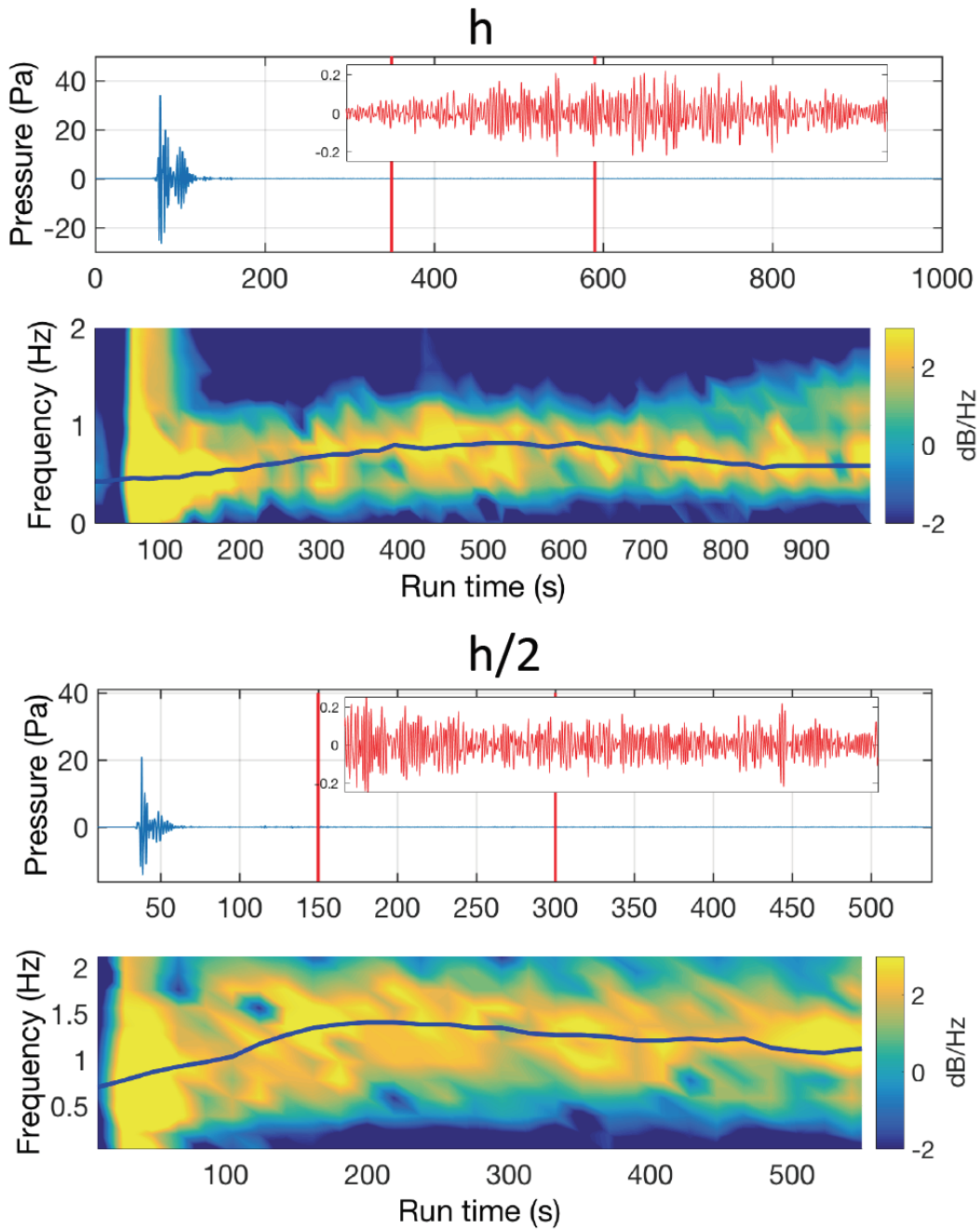


FIGURE 5.21: Comparison between the signal produced by two density current with typical dimension h (top figure) and $h/2$ (bottom figure) respectively and related spectrograms. Blue lines represent the peak frequency in each window of calculation.

of 12% on the recorded frequency. We will disregard this effect in our analysis. Changes of h directly induce changes in the propagation velocity of

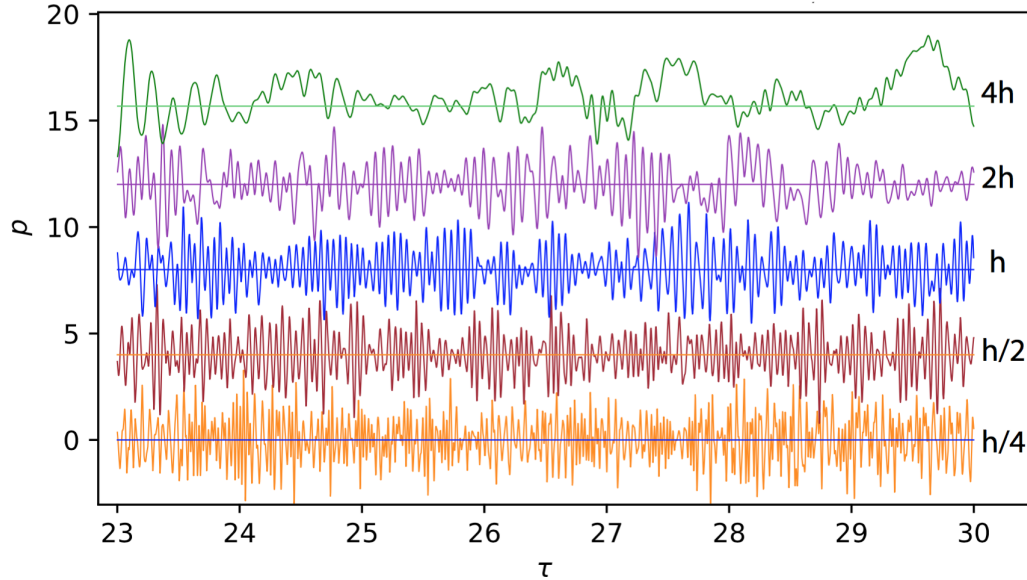


FIGURE 5.22: *Infrasonic traces recorded by pressure probes for different simulations with different h . It is worth to notice that the smaller is h the higher is the frequency of the acoustic signal.*

the flow. In order to discriminate the effect of the current dimension h and the effect of different flow velocity on the generation of infrasonic signal, we perform a second set of simulations. In this set the initial concentration of the $2D$ volume, and thus the value of reduced gravity g' , is varied maintaining instead a fix initial dimension h , equal to the standard case.

As shown in Figure 5.25, varying the values of reduced gravity in a range which goes from $2g'$ to $g'/10$ we simulate flows with different velocity (see the run-outs curves in Fig. 5.25). The propagation velocity of the flows in this second set of simulations cover a range spanning from values comparable with the case h to values comparable with the case $h/2$. Now, looking at the related spectra for these cases with different flow velocity we do not observe the same variation in the peak frequency that we observed changing h .

Hence, we can reasonably infer that the flow velocity is not the main parameter controlling the frequency content of the infrasonic signal. The flow dimension is the most important parameter to determine the main frequency of the infrasonic signal produced by the inertial propagation of the current in atmosphere.

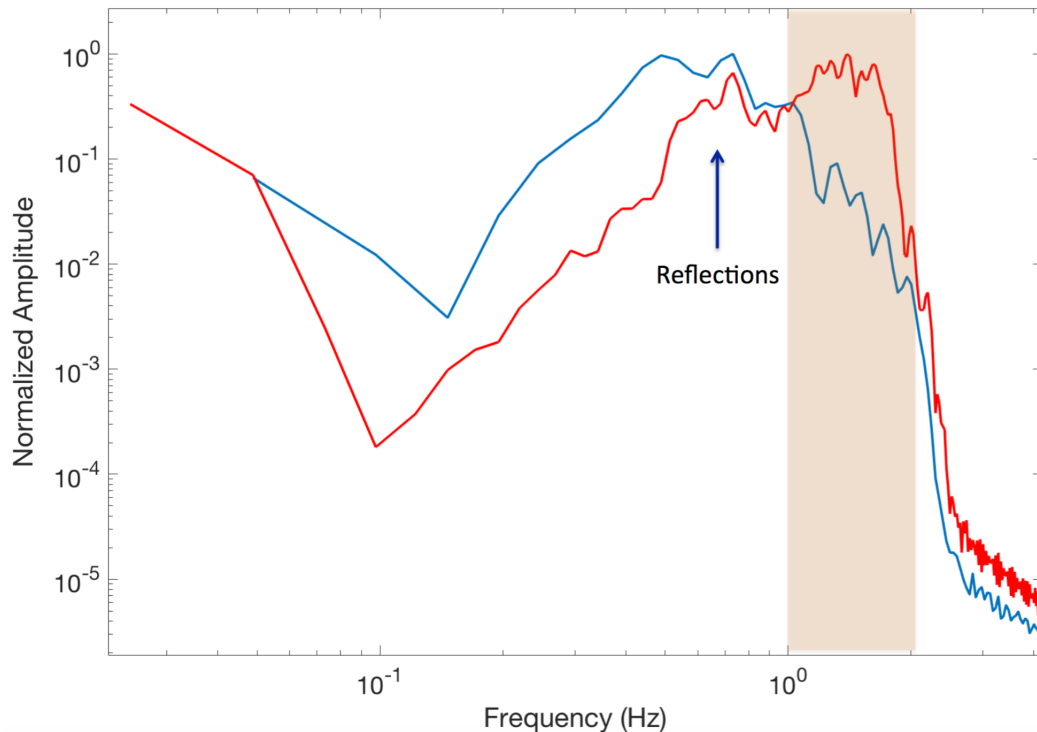


FIGURE 5.23: Example from the $h/2$ case of the analysis we performed to recognize and isolate reflections of the large pressure signal produced by the collapsing phase of the current. We compare the spectrum of the collapsing and slumping phase of the signal (blue), with the spectrum of the inertial part of the signal on which we focus our analysis (red).

It is worth to notice that increases in flow velocity seems to produce signals with a broader frequency content and a higher amplitude. Thus in this case the velocity of the flow would correlate with the total energy released in the atmosphere and thus with the range of frequencies excited and signal amplitude.

The dependence of the peak frequency of the analysed signals from the dimension of the current can be efficiently visualized plotting for each simulation the dominant period of the infrasonic signal produced, as a function of the current dimension h (Fig. 5.27). Our numerical results show a clear linear relation between the acoustic wave period and the current dimension which, if expressed in terms of the physical magnitudes characterizing our problem (sound propagation velocity in atmosphere, c , the acoustic waves period and the typical height of the current, h), may be written as:

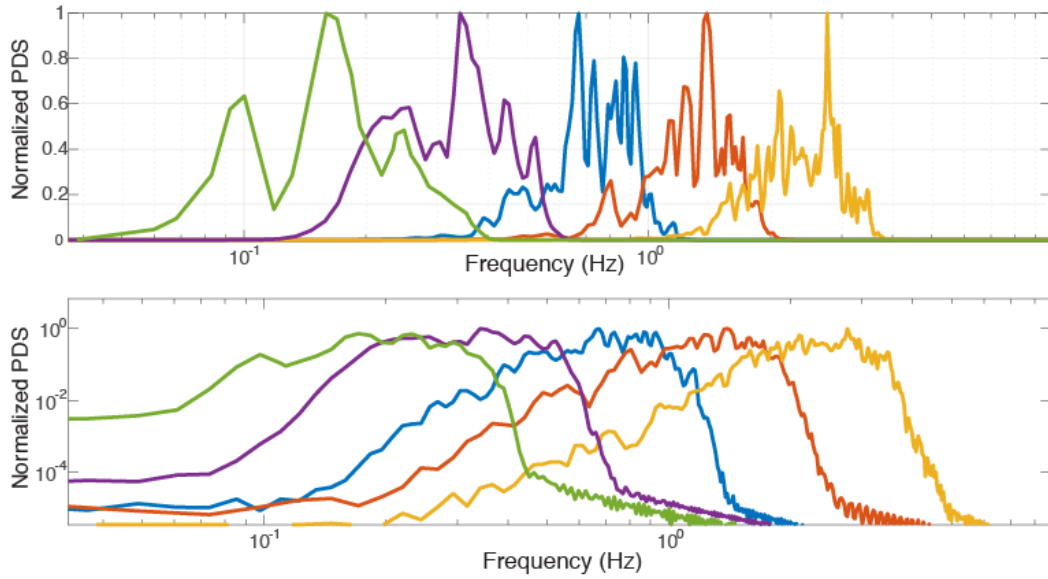


FIGURE 5.24: Power density spectra of the signals from the first set of simulations. The amplitude is normalized and reported both in linear (top) and logarithmic (bottom) scale. Different colors refer to different h .

$$Period = \frac{\pi h}{2c} \quad (5.28)$$

A more comprehensive discussion about physical mechanisms and theoretical implications of our results, along with possible outcomes of our work, are presented in Chapter 6.

5.3.5 Analysis of the numerical configuration

We conclude the chapter briefly showing the results of the analysis we performed to provide an estimation of the error due to approximations and to the discrete numerical solver, such as: temporal and spatial resolution, two or three dimensions of the domain, temporal and spatial interpolation scheme. The model configuration described in Sec. 3.2.2 has proved to efficiently reproduce the dynamics of gravity currents and sound propagation in atmosphere. However, the effect of the numerical setting on the infrasonic peak frequency should be investigated to have a quantification of the error due to the numerical model. The three h , $h/4$ and $4h$ cases have been selected for this analysis, varying numerical configuration in each case, as

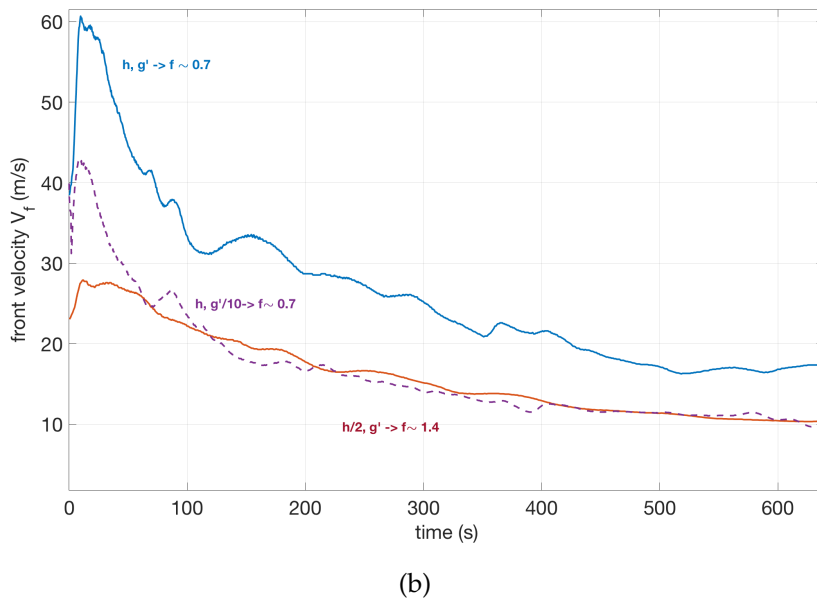
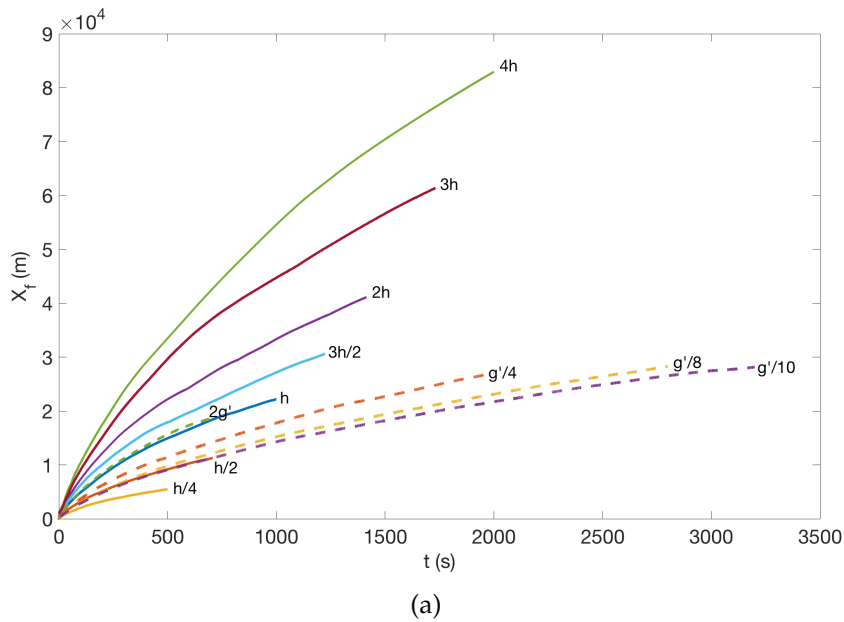


FIGURE 5.25: *a) Evolution with time of the front position for each simulation (first set represented with solid lines and second set with dashed lines). b) Front velocity evolution for the (h, g') case (blue), the $(h, g'/10)$ case (purple), the $(h/2, g')$ case (red).*

summarized in Tab. 5.1. In Fig. 5.28, the variability of the peak frequency of the infrasonic spectrum is shown. The error bar width is the maximum difference with respect to each reference case.

The effect of each explored parameter is described below:

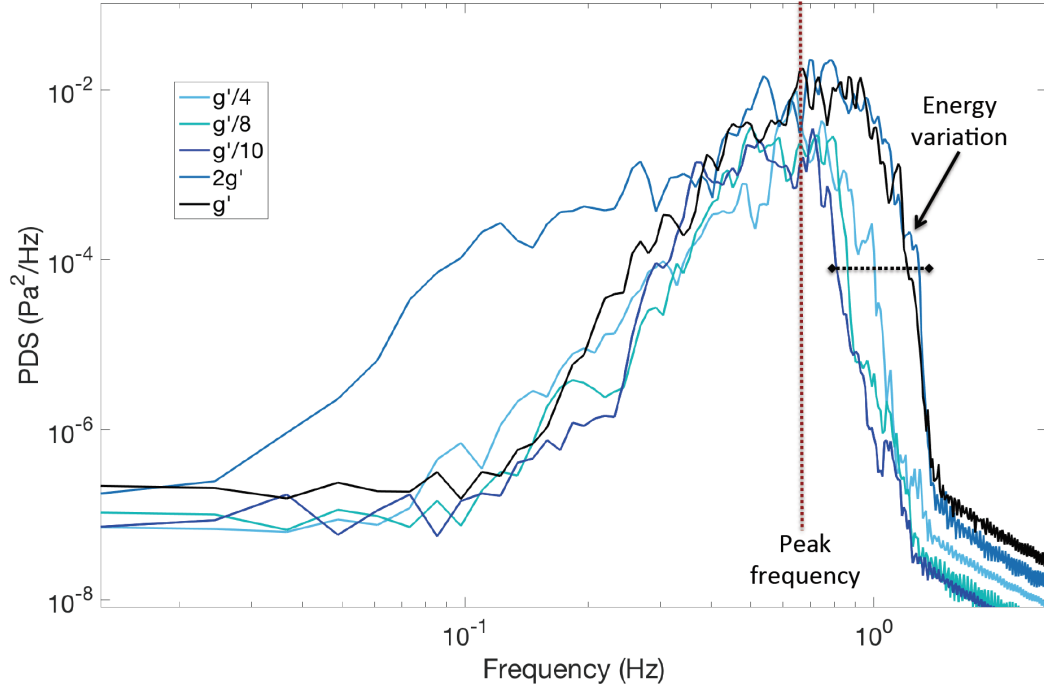


FIGURE 5.26: Power density spectra of the signals from the second set of simulations compared with the standard case (g' , black line). We notice that flows with different velocities produce acoustic signals with almost constant peak frequency but with broader frequency content for higher flow velocity.

- **2D vs 3D.** The comparison between our three-dimensional and two-dimensional simulations shows that the main features of the gravity current are not influenced by the lack of a third dimension. Indeed, the evolution of the front position and of the head volume in 3D remains very similar to that in 2D. In principle, even if the shape of the current is not influenced by the dimensions of the domain, the acoustic emission can be affected by the lack of the third dimension. However, simulations shows that the peak frequency predicted by 2D simulations is very similar to that obtained in 3D.

A possible explanation to this behavior is given here. The governing forces responsible of the gravity currents motion are gravity and entrainment. The former is described by the Von Karman and Benjamin theory [88, 89], telling us that the Froude number of the front of the current can be approximated to a constant. This prediction is reproduced

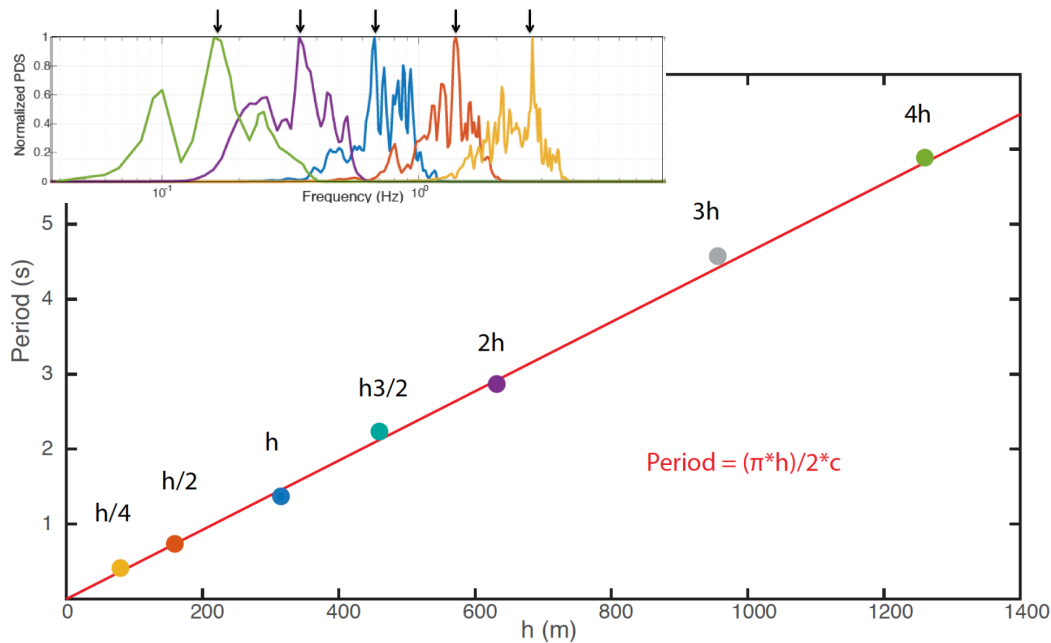


FIGURE 5.27: We report for each simulation with different size of the current the value of the characteristic height, h and the principal period of the related infrasonic signal. A clear linear dependence relate the size of the event and the peak frequency of the sound produced.

identically by both the 2D and 3D model. On the other hand, entrainment is induced by turbulence, but 2D and 3D turbulence are essentially different, with a very different energy spectrum. However, in Large Eddy Simulations of gravity currents the entrainment efficiency is well reproduced even in 2D, being able to capture the head volume evolution. Therefore, although the turbulence structure is three-dimensional, it is reasonable that the first-order, large-eddy dynamics results to be closely reproduced by two-dimensional simulations [104].

- **Grid resolution.** As shown in Tab. 5.1, in each scenario a simulation at higher resolution is performed. In particular, we move from 1500×73 to 2500×121 cells (from 109,500 to 302,500 cells). Results are stable enough to allow us to use the lower resolution for all the simulations presented in this chapter.
- **Time discretization.** The numerical solver uses an adaptive time step based on the Courant number $Co = 0.2$. This is to ensure that $\delta t \lesssim Co \frac{\delta x}{u}$, where δx is the cell size and u is the magnitude of the velocity.

Height m	Resolution m	Dimensions -	Max δt s	Interpolation -	Peak frequency Hz
$10^{5/2}$	20x3.3	2D	$\frac{\delta x}{c} \frac{\sqrt{2}}{2}$	limited linear	0.73
$10^{5/2}$	12x2.0	2D	$\frac{\delta x}{c} \frac{\sqrt{2}}{2}$	limited linear	0.73
$10^{5/2}$	20x3.3	2D	$\frac{\delta x}{u} \text{Co}$	limited linear	0.62
$10^{5/2}$	20x3.3	2D	$\frac{\delta x}{c} \frac{\sqrt{2}}{2}$	linear	0.70
$10^{5/2}$	20x3.3	3D	$\frac{\delta x}{c} \frac{\sqrt{2}}{2}$	limited linear	0.70
$\frac{1}{4} 10^{5/2}$	5.0x0.83	2D	$\frac{\delta x}{c} \frac{\sqrt{2}}{2}$	limited linear	2.3
$\frac{1}{4} 10^{5/2}$	3.0x0.5	2D	$\frac{\delta x}{c} \frac{\sqrt{2}}{2}$	limited linear	2.6
$\frac{1}{4} 10^{5/2}$	5.0x0.83	2D	$\frac{\delta x}{u} \text{Co}$	limited linear	2.0
$\frac{1}{4} 10^{5/2}$	5.0x5.0x0.83	3D	$\frac{\delta x}{c} \frac{\sqrt{2}}{2}$	limited linear	2.0
$\frac{1}{4} 10^{5/2}$	5.0x5.0x0.83	3D	$\frac{\delta x}{c} \frac{\sqrt{2}}{2}$	linear	2.1
$4 * 10^{5/2}$	80x13	2D	$\frac{\delta x}{c} \frac{\sqrt{2}}{2}$	limited linear	0.1
$4 * 10^{5/2}$	48x8.0	2D	$\frac{\delta x}{c} \frac{\sqrt{2}}{2}$	limited linear	0.07
$4 * 10^{5/2}$	80x80x13	3D	$\frac{\delta x}{c} \frac{\sqrt{2}}{2}$	limited linear	0.09

TABLE 5.1: Simulations performed varying the numerical configurations of three different scenarios: h , $h/4$ and $4h$. The reference case is defined by $h = 10^{5/2}$ m. Resolution is given in the form $\delta y x \delta z$ (2D) or $\delta x x \delta y x \delta z$ (3D). The time step $\delta t = \frac{\delta x}{u} \text{Co}$ is fixed by the Courant number $\text{Co} = 0.2$. Simulations with maximum $\delta t = \frac{\delta x}{c} \frac{\sqrt{2}}{2}$ limit the time step to this value. The interpolation scheme for the advective terms is reported beside the peak frequency of the infrasonic spectrum. Highlighted text indicates which parameter is changing with respect to the reference case (at the top of each table section).

However, here we want to model not only the flow dynamics but also the generation and propagation of sound, which travels at velocity c . Thus, we have to ensure also that $\delta t < \frac{\delta x}{c}$. We checked the effect of this last condition. Results are reported in Tab. 5.1. Simulations without the constrain based on the speed of sound are not taken into account for the quantification of the numerical error. All the other simulations are performed with the correct constraint.

We tried also to move from the second-order Crank-Nicolson scheme

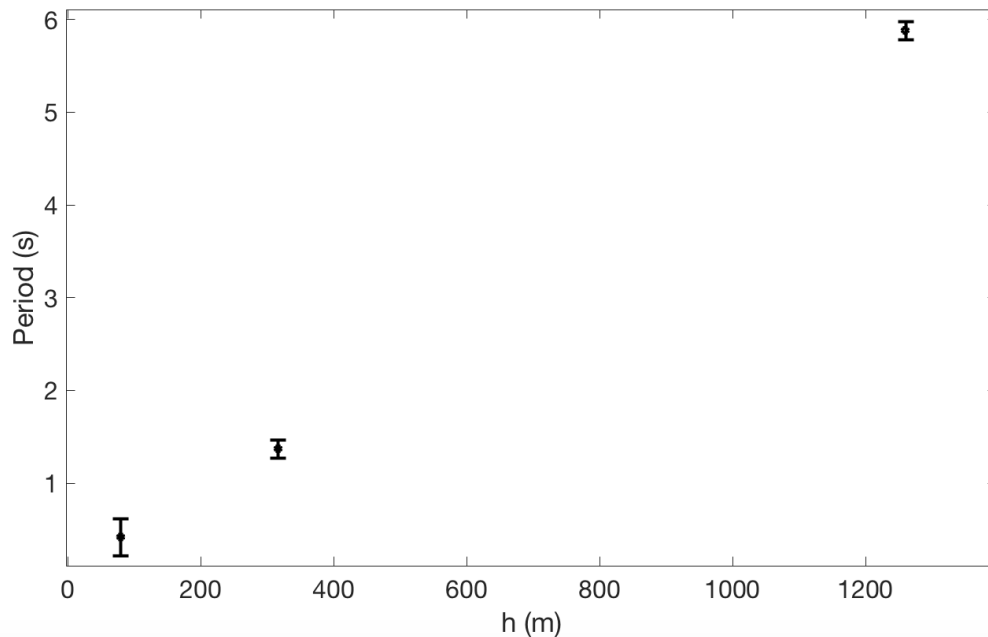


FIGURE 5.28: Error bar evaluated for three cases with different h (h , $h/4$ and $4h$) and obtained changing different numerical configurations for each case and analysing the signal related.

to the first-order forward Euler scheme. Results are not in Tab. 5.1 because a first-order integration in time is not enough to resolve acoustic waves.

- **Spatial discretization.** We have used two kind of second order central schemes for spatial interpolation: the standard linear scheme and the limited linear scheme based on the Sweby limiter [100]. The unbounded linear scheme is not stable enough in 2D. For this reason, all the simulations used in the previous section are performed with the Sweby limiter and the error bars in Fig. 5.28 do not take into account 2D simulations with the unbounded scheme.

5.4 Chapter Conclusions

Our simulations indicate that the turbulent moving head of the density current is the main source of pressure disturbances in the atmosphere. The propagation of such generated acoustic waves is well reproduced by the model. The principal frequency content of the infrasonic signal depends

from the dynamics of the turbulent current inertially propagating in atmosphere. In particular, the peak frequency of the infrasonic signal results to strongly depend from the height of the current head, while changes of the flow velocity do not much affect this principal frequency content. Further investigation will be carried out in future to clarify the possible dependence of the flow velocity on the signal amplitude. A comprehensive discussion about the physical mechanisms suggested from our results, underlying the production of sound from a turbulent multiphase moving flow and possible theoretical implications is presented in detail in the next chapter. An overview of the future directions opened from this study is also discussed at the end of the next Chapter.

Chapter 6

Discussion and Conclusions

Contents

6.1 Towards a quantitative use of infrasound: the frequency-magnitude relation	120
6.1.1 Numerical results	120
6.1.2 From the model to the real case	122
6.2 Linking current dynamics and acoustic emissions: a quest for explanation	124
6.2.1 Density currents as source of sound	124
6.2.2 Comparison between surficial mass movements with different dynamic	127
6.3 Conclusions	127

We discuss here the results presented in the previous chapters taking into account the current state of the art and the principal scientific issues related to the study of the acoustic emission of surficial mass movements. Significant progress towards understanding and modeling seismo-acoustic signals from such events has been made in the recent years. However, extracting quantitative information from seismic and infrasonic signals generated by surficial mass movements still remains a major challenge [1].

Within this general framework, our work represents an innovative approach. Integrating real observations and numerical modeling, we attempt to disclose and investigate the physical processes underlying the acoustic emission of density currents. In the following sections, we discuss and compare our numerical results with field observations, exploring the efficiency of acoustic techniques to measure and quantitatively estimate the magnitude of

density currents. Besides, possible source mechanisms for acoustic waves are explored based on the evidence provided by our modeling. Finally, possible implications of our study, in terms of operational acoustic monitoring are discussed as future steps and improvements.

6.1 Towards a quantitative use of infrasound: the frequency-magnitude relation

While the intrinsic complexity of real PDCs limits the possibility to relate the characteristic features of the flow to the properties of acoustic signals measured in the field, numerical modeling give us the possibility to control the dependence from each parameter, adding complexity step-by-step.

Our numerical results, even if referred to a simplified current dynamics, show how our approach may represent a powerful tool to understand flow-atmosphere interactions.

6.1.1 Numerical results

We studied the simple configuration of the dam-break experiment, focusing our analysis on the sound produced by the current propagating in the atmosphere. In the inertial phase of motion, the head of the current is well developed and maintains a constant vertical dimension h . We analyzed the frequency content of the emitted acoustic signal changing the current height, h , and the reduced gravity, g' , which are the only two variables characterizing our experimental setup.

We found a linear relationship between the peak value of the power density spectrum of the acoustic signal and h , while changing g' , keeping h constant, we do not observe similar frequency shifts. This latter result means that the main signal frequency does not depends either from the flow velocity (which, at fixed h , depends only on g' : $v \sim \sqrt{g'h}$) or from the flow concentration. Our observations are referred to a dilute flow composed by fine particles which remain in suspension during the whole flow motion in the horizontal plane. We suggest that our findings may be extended to the more general case where particles settling is considered. In fact, we expect that flow concentration changes due to deposition processes (affecting g') would

not affect the main frequency of the acoustic emission (particle settling does not affect h).

The motion of the inertially propagating current on the horizontal plane is controlled at the front by the Froude number which results to be approximately constant and parameterize all the resistances to the flow motion. An important consequence is that the dynamics of inertial gravity currents are independent of the slope of the underlying topography up to angles of $\sim 30^\circ$, typical of the conditions for PDCs [4].

Real world situations are characterized by inclined current path where the slope decreases with the distance. As a consequence PDC, in nature, undergo an accelerating-decelerating trend. Infrasonic signals related to PDCs activity recorded in the field are characterized by typical spindle-shaped waveforms (e.g. [9]) and several hypothesis have been made to explain such gradually increasing signal, which imply a source that gradually builds up in time, growing momentum and size. Adding such topographical profile to our experimental setup should allow us to reproduce this observed waveform and to study in much detail how the flow-topography interaction can affect the acoustic emission. Moreover, if the dimensions of the turbulent flow front increase along its downhill path, we expect, given our numerical results, to observe a decrease in acoustic frequencies.

What can be seen for all the performed simulations is that the head of the current is the main source of acoustic wave radiation. In our simulations, intense mixing with the background fluid occurs only at the flow front thus, the head is the only part of the current which develops turbulent structures and large eddies.

Turbulence is thought to be a major source of infrasound in volcanic eruptions. However, the contribution of the turbulent structures to the sound production for these type of flows has not been properly addressed to date [1].

We point out that the turbulent head dynamics are characterized by a time scale, given by the box-model, depending on the current velocity. This typical period results proportional to the square root of h ($\tau_{KH} = 2\pi\sqrt{\frac{h}{g'}}$) as reported in the previous chapter.

Instead, our results show that the pressure perturbations induced by this turbulent moving front, have a typical wave period linearly dependent on

the dimension of the density current h :

$$Period = \alpha \cdot h \quad (6.1)$$

With $\alpha \simeq \frac{\pi}{2c}$.

This means that there are two typical time scales: one for the dynamics of the current and one for the propagation of the acoustic signal. These two time scales are linked to two velocity scales: inside the current we have the flow velocity, proportional to the square root of the modified gravity times the size of the current; outside the current we have the speed of sound, which is constant. Inside the current the typical time is $\tau \propto h/u \propto \sqrt{(h/g')}$, while outside it is $\tau \propto h/c$.

6.1.2 From the model to the real case

We compare our numerical results with the geophysical data reported in Chapter 3. Those observation primarily concern several PDCs episodes along with some cases of powder snow avalanches and rock avalanches. All these type of surficial mass movements have a similar behavior, at least with regard to the flow-atmosphere interaction. These flows develop a largely extended turbulent front, which drive the current during its motion, and is controlled by mechanisms of air entrainment and fed from the denser current body. This general dynamics is well reproduced by our model and significantly differ from other kind of event such as debris flows, lahars or wet snow avalanches. In the latter, in fact, the large amount of water do not allow the formation of an extended dilute and turbulent layer resulting in a different flow-atmosphere coupling.

In the dataset reported in Chapter 3 (Fig. 6.1) a relation between the estimated flow deposit volumes (V_d) and the acoustic signal frequency is shown. Data are reported in logarithmic scales and we computed the best fit (goodness of fit $R = 0.95$ (log)) for a power law of the type $y = ax^n$, obtaining a value for the exponent of $n = 3.2$, which gives the following approximated relationship:

$$V_d \simeq b \cdot f^{-3} \quad (6.2)$$

where b is the fit parameter.

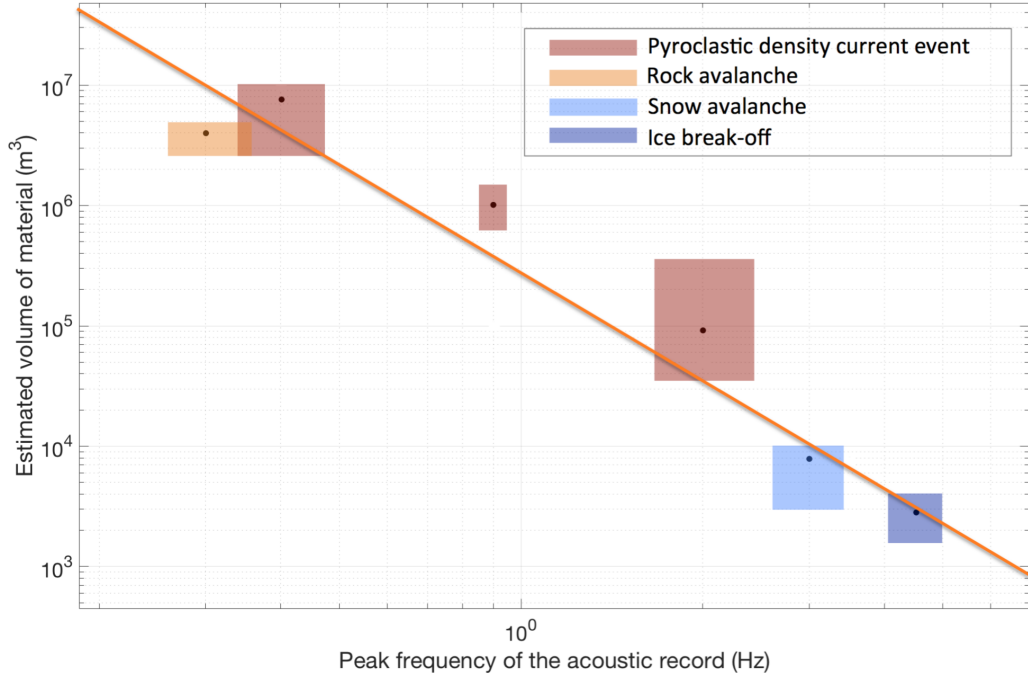


FIGURE 6.1: Data presented in Chapter 3 show a relation between the estimated flow deposit volumes (V_d) and the acoustic signal frequency is. The best fit (red line) is computed for a power law of the type $y = ax^n$, obtaining a value for the exponent of $n = 3.2$.

Assuming that the deposited volume is proportional to the volume of the moving current through a factor ϵ_s which express the average concentration of the solid particles:

$$V_d = \epsilon_s V_c \quad (6.3)$$

and that the volume of the moving current results proportional to the third power of the current vertical dimension

$$V_c = ah^3 \quad (6.4)$$

where a is the shape factor for our current, we obtain:

$$Period = \frac{1}{f} = (\epsilon_s a/b)^{\frac{1}{3}} \cdot h \quad (6.5)$$

Therefore, geophysical observations for this type of turbulent directed flows, with run-out length much larger than the width of the front, can be considered in agreement with our numerical findings. Somehow confirming

a linear relation between acoustic peak frequency and the typical height of the flow front.

6.2 Linking current dynamics and acoustic emissions: a quest for explanation

Despite the unavoidable simplifications requested by the numerical approach, modeling is providing the mean to explore natural phenomena and to understand field observations and measures. This is especially true in the case of volcanic activity or other natural phenomena where the geophysical measures are often limited by the severe exposure to physical damage and safety risk. Here the modeling could be crucial to further advance the understanding of the source mechanism and dynamics.

An integrated approach, coupling infrasound field observations and numerical simulation has already been used by several authors for the study of explosive volcanic sources. All these works mainly focus on wave propagation modeling starting from arbitrary point sources (e.g., [102]; [67]).

However, differently from the common approach, where a simplified source mechanism is imposed, in our case the infrasound generation is a result of the simulated sub-aerial density current propagation. As far as we know this is the first study which simulate together the density current and the corresponding acoustic wavefield [1].

6.2.1 Density currents as source of sound

Source theory for infrasound from mass movement is currently not well understood. A dipole-like behavior may be generated by different internal structures and dynamics of the moving current such as the wave-like oscillations of the velocity and density field. Also, the stable compression and decompression areas originating respectively at the flow front and in correspondence of the large eddy in the head, moving with the propagation of the current, can induce dipole-like disturbances in the background pressure field.

Once observed that the acoustic emission is related to the dynamics of the head (previous section), a more detailed observation of the proximal radiation field could help us to get a deeper insight into the sound production mechanisms.

In general there are two basic types of sound source mechanisms: emission by (moving) rigid body-fluid interaction and emission by fluid (possibly turbulent) flow. In both cases, directivity patterns represent the angular distribution of the sound field radiated by the source. Referring to our observed radiation pattern, Fig. 6.2, we see three evident phase changes, one along the normal direction to the fluid motion and two at almost 45° and -45° .

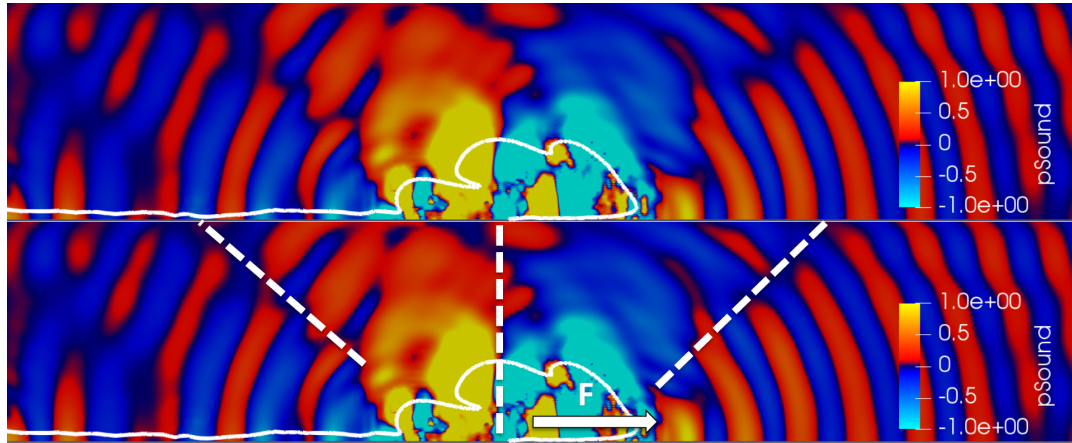


FIGURE 6.2: Proximal wavefield of the current head. Inertial and drag forces act horizontally. We notice different phase changes of the radiated acoustic waves.

We here recall some general concepts on the acoustic source theory for sound produced by moving flows. At the lowest orders, acoustic sources can behave like a point source (monopole), which introduce and withdraw fluid causing rarefaction and contraction, or a dipole source which moves a portion of fluid back and forth. Monopoles are related to a net introduction of fluid while dipoles are equivalent to a force acting on the fluid implying a net momentum transfer [105], in this case no net fluid is introduced. Higher order sources are superposition of dipoles and monopoles.

Our complex radiation pattern can not be easily explained by such simple sources but, guided by the intuition offered by the experimental radiation field, we try to grasp the basic physical mechanism occurring in the current head. A dipole, excited by a force \vec{F} , emits a pressure field given by:

$$p(r, \theta, t) = -\rho \frac{\partial \phi}{\partial t} \quad (6.6)$$

where $\phi = \nabla \vec{v}$ is the velocity potential (see Appendix A for details):

$$\phi(r, \theta, t) = \frac{3F}{Zk} \frac{(1 + ikr)}{r^2} e^{i(\omega t - kr)} \cos \theta \quad (6.7)$$

Z is the impedance of the medium in which the wave is propagating and k in the wave number.

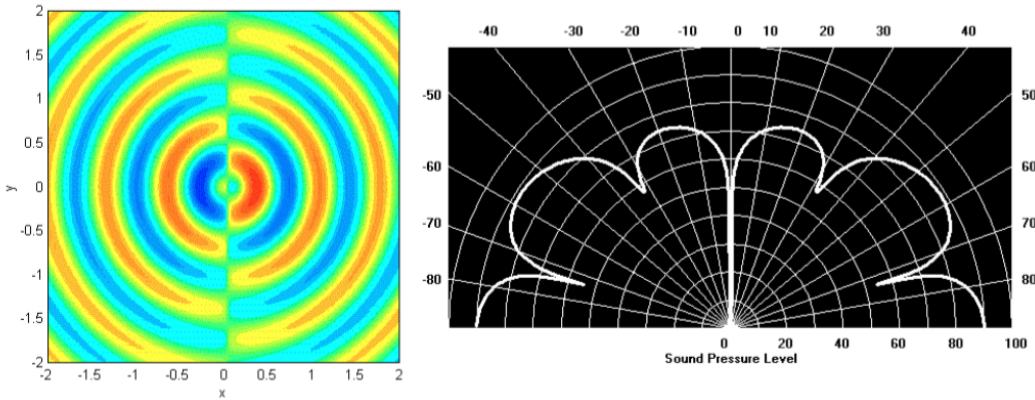


FIGURE 6.3: *Right: Radiation pattern of a dipole excited by a force acting along x . Left: Radiation pattern of a dipole excited by a force acting along x in proximity of a rigid horizontal reflecting surface*

We can see that the field depends only on the distance from the origin, r and on θ the angle between \vec{F} and \vec{r} .

In particular, we note that it is zero along the direction perpendicular to the force which excites the dipole. Here the wave front has a sudden change of phase (see Fig. 6.3).

As we noted, the current pressure field shows a similar behavior: inertial force and viscous drag act along x direction and a change phase is present along y .

Our findings presented in the previous section agree with the general fact that the fundamental frequency of a vibrating body is inversely related to the body typical dimension. This can be seen as follows. Let v_s be the sound speed in body and h the body dimension. The fundamental frequency of oscillations is thus given by:

$$f \propto \frac{h}{2 \cdot v_s} \quad (6.8)$$

where v_s is the acoustic propagation velocity in the body.

6.2.2 Comparison between surficial mass movements with different dynamic

Our simulations show that in the inertial phase of motion acoustic waves clearly originate from the head of the current. Previous field studies show how infrasonic array processing allows tracking pyroclastic flows front position in real-time ([10]; [11]). Similar source tracking using infrasound arrays has been applied to snow avalanches (e.g. [47], [72]). These evidences are in accordance with a localized source of acoustic emission which moves with the active flow front.

On the other hand, a source extended along the whole current body would not produce a coherent signal at different array sensors located at a distance of the same order of the flow length. Similar lack of coherency in the signal recorded by an array of sensors for a debris flow event has been recently reported by Marchetti et al. (see the paper reported in Appendix A).

6.3 Conclusions

Results presented in this thesis may have important implications both in the monitoring and understanding of density current phenomena. We found that the flow front vertical dimension is the most important parameter to determine the main frequency of the infrasonic signal produced by the inertial propagation of a dilute turbulent current in atmosphere.

This indicates that this complex dynamics can be simply represented by a diaphragm which is emitting acoustic waves while is moving along the slope. The acoustic wavefield associated to the density currents are thus generated by the oscillations of the diaphragm induced by the turbulence generated at the head of the current. Frequency content is then representative for the dimension of the moving front and it can be used to quantify the volumes of the density current.

Our empirical relation could have important implication in terms of hazard assessment. If confirmed, it may be used to roughly estimate the magnitude of this type of moving flows in real time, significantly improving the potential of the infrasonic technique in terms of operational monitoring.

The integrated approach presented in this study merging observations from experimental geophysics and the numerical modeling is innovative in this research field. In fact, this is the first study which simulates together the density current and the corresponding acoustic wavefield.

Further extension of the presented study, which may consider the interaction with a real topography, and other improvements as well as comparison with data from large scale experiment will help to clarify the nature of the acoustic sources related to density currents.

Bibliography

- [1] K. E. Allstadt, R. S. Matoza, A. B. Lockhart, S. C. Moran, J. Caplan-Auerbach, M. M. Haney, W. A. Thelen, and S. D. Malone, “Seismic and acoustic signatures of surficial mass movements at volcanoes”, *Journal of volcanology and geothermal research*, vol. 364, pp. 76–106, 2018.
- [2] J. E. Simpson, “Gravity currents in the environment and the laboratory (2nd edn)”, vol. 352, pp. 374–378, 1999.
- [3] J. Dufek, “The fluid mechanics of pyroclastic density currents”, *Annual review of fluid mechanics*, vol. 48, no. 1, pp. 459–485, 2016.
- [4] O. Roche, J. C. Phillips, and K. Kelfoun, “Pyroclastic density currents”, in *Modeling volcanic processes: The physics and mathematics of volcanism*, S. A. Fagents, T. K. P. Gregg, and R. M. C. Lopes, Eds. Cambridge University Press, 2013, pp. 203–229.
- [5] J. Dufek and G. W. Bergantz, “Suspended load and bed-load transport of particle-laden gravity currents: The role of particle–bed interaction”, *Theoretical and computational fluid dynamics*, vol. 21, no. 2, pp. 119–145, 2007.
- [6] B. Sovilla, M. Schaer, and L. Rammer, “Measurements and analysis of full-scale avalanche impact pressure at the Vallée de la Sionne test site”, *Cold regions science and technology*, vol. 51, no. 2, pp. 122–137, 2008, International Snow Science Workshop (ISSW) 2006.
- [7] A. Kogelnig, E. Surinach, I. Vilajosana, J. Hubl, B. Sovilla, M. Hiller, and F. Dufour, “On the complementariness of infrasound and seismic sensors for monitoring snow avalanches”, *Natural hazards and earth system science*, vol. 11, no. 8, pp. 2355–2370, 2011.

- [8] E. S. Calder, R. Lockett, R. S. J. Sparks, and B. Voight, "Mechanisms of lava dome instability and generation of rockfalls and pyroclastic flows at Soufrière Hills Volcano, Montserrat", *Geological society, london, memoirs*, vol. 21, no. 1, pp. 173–190, 2002.
- [9] H. Yamasato, "Quantitative analysis of pyroclastic flows using infrasonic and seismic data at Unzen Volcano", *J. phys. earth*, vol. 45, pp. 397–416, 1997.
- [10] M. Ripepe, S. De Angelis, G. Lacanna, P. Poggi, C. Williams, E. Marchetti, D. D. Donne, and G. Ulivieri, "Tracking pyroclastic flows at Soufrière Hills Volcano", *Eos, transactions american geophysical union*, vol. 90, no. 27, p. 229, 2009.
- [11] D. Delle Donne, M. Ripepe, S. De Angelis, P. Cole, G. Lacanna, P. Poggi, and R. Stewart, "Thermal, acoustic and seismic signals from pyroclastic density currents and vulcanian explosions at Soufrière Hills Volcano, Montserrat", *Geological society, london, memoirs*, vol. 39, no. 1, pp. 169–178, 2014.
- [12] J. B. Johnson and M. Ripepe, "Volcano infrasound: A review", *Journal of volcanology and geothermal research*, vol. 206, no. 3, pp. 61–69, 2011.
- [13] G. Barfucci and M. Ripepe, "Dome collapse interaction with the atmosphere", *Geophysical research letters*, vol. 45, no. 17, pp. 8923–8930, 2018.
- [14] B. Voight, R. Janda, H. Glicken, and P. Douglass, "Nature and mechanics of the Mount St. Helens rockslide-avalanche of 18 May 1980", *Geotechnique*, vol. 33, no. 3, pp. 243–273, 1983.
- [15] H. Kanamori and J. W. Given, "Analysis of long-period seismic waves excited by the may 18, 1980, eruption of Mount St. Helens—a terrestrial monopole?", *Journal of geophysical research: Solid earth*, vol. 87, no. B7, pp. 5422–5432, 1982.
- [16] E. E. Brodsky, E. Gordeev, and H. Kanamori, "Landslide basal friction as measured by seismic waves", *Geophysical research letters*, vol. 30, no. 24, 2003.

- [17] J. Zhao, L. Moretti, A. Mangeney, E. Stutzmann, H. Kanamori, Y. Capdeville, E. S. Calder, C. Hibert, P. J. Smith, P. Cole, and A. LeFriant, "Model space exploration for determining landslide source history from long-period seismic data", *Pure and applied geophysics*, vol. 172, no. 2, pp. 389–413, 2015.
- [18] K. L. Pankow, J. R. Moore, J. M. Hale, K. D. Koper, T. Kubacki, K. M. Whidden, and M. K. McCarter, "Massive landslide at Utah copper mine generates wealth of geophysical data", *Gsa today*, pp. 4–9, 2014.
- [19] M. Ripepe, C. Bonadonna, A. Folch, D. D. Donne, G. Lacanna, E. Marchetti, and A. Hoskuldsson, "Ash-plume dynamics and eruption source parameters by infrasound and thermal imagery: The 2010 Eyjafjallajökull eruption", *Earth and planetary science letters*, vol. 366, pp. 112–121, 2013.
- [20] S. S. Gylfadottir, J. Kim, J. K. Helgason, S. Brynjolfsson, A. Hoskuldsson, T. Johannesson, C. B. Harbitz, and F. Lvholt, "The 2014 Lake Askja rockslide-induced tsunami: Optimization of numerical tsunami model using observed data", *Journal of geophysical research: Oceans*, vol. 122, no. 5, pp. 4110–4122, 2017.
- [21] C. de Groot-Hedlin, M. A. H. Hedlin, and K. Walker, "Finite difference synthesis of infrasound propagation through a windy, viscous atmosphere: Application to a bolide explosion detected by seismic networks", *Geophysical journal international*, vol. 185, no. 1, pp. 305–320, 2011.
- [22] G. Lacanna, M. Ichihara, M. Iwakuni, M. Takeo, M. Iguchi, and M. Ripepe, "Influence of atmospheric structure and topography on infrasonic wave propagation", *Journal of geophysical research: Solid earth*, vol. 119, no. 4, pp. 2988–3005, 2014.
- [23] H. Sato, T. Fujii, and S. Nakada, "Crumbling of dacite dome lava and generation of pyroclastic flows at unzen volcano", *Nature*, vol. 360, p. 664, 1992.
- [24] R Lockett, B. Baptie, L Ottemoller, and G. Thompson, "Seismic monitoring of the Soufriere Hills Volcano, Montserrat", *Seismological research letters*, vol. 78, pp. 192–200, 2007.

- [25] "Source mechanism of seismic waves excited by pyroclastic flows observed at Unzen volcano, Japan", *Journal of geophysical research: Solid earth*, vol. 99, no. B9, pp. 17 757–17 773, 1994.
- [26] A. Brodscholl, S. B. Kirbani, and B. Voight, "Sequential dome-collapse nuées ardentes analyzed from broadband seismic data, Merapi Volcano, Indonesia", *Journal of volcanology and geothermal research*, vol. 100, pp. 363–369, 2000.
- [27] H. Oshima and T. Maekawa, "Excitation process of infrasonic waves associated with Merapi-type pyroclastic flow as revealed by a new recording system", *Geophysical research letters*, vol. 28, no. 6, pp. 1099–1102, 2001.
- [28] N. Green and J. Neuberg, "Seismic and infrasonic signals associated with an unusual collapse event at the Soufrière Hills Volcano, Montserrat", *Geophysical research letters*, vol. 32, 2005.
- [29] M. Ripepe, S. De Angelis, G. Lacanna, and B. Voight, "Observation of infrasonic and gravity waves at Soufrière Hills Volcano, Montserrat", *Geophysical research letters*, vol. 37, no. 19, 2010.
- [30] A. J. Stinton, P. D. Cole, R. C. Stewart, H. M. Odbert, and P. Smith, "Chapter 7 the 11 February 2010 partial dome collapse at Soufrière Hills Volcano, Montserrat", *Geological society, London, memoirs*, vol. 39, no. 1, pp. 133–152, 2014.
- [31] P. Cole, P. Smith, A. Stinton, H. Odbert, M. Bernstein, J. Komorowski, and R. Stewart, "Vulcanian explosions at Soufrière Hills Volcano, Montserrat between 2008 and 2010", *Geological society, London, memoirs*, vol. 39, no. 1, pp. 93–111, 2014.
- [32] S. De Angelis, V. Bass, V. Hards, and G. Ryan, "Seismic characterization of pyroclastic flow activity at Soufrière Hills Volcano, Montserrat, 8 January 2007", *Natural hazards and earth system sciences*, vol. 7, no. 4, pp. 467–472, 2007.
- [33] T. Fukuzono and H. Terashima, "Experimental study of the process of failure in cohesive soil slope caused by rainfall", *H. rep. natn. res. center disaster prev.*, vol. 29, pp. 103–122, 1982.

- [34] B. Voight, "A method for prediction of volcanic eruptions", *Nature*, vol. 332, 125 EP –, 1988.
- [35] C. Hammer and J. W. Neuberg, "On the dynamical behaviour of low-frequency earthquake swarms prior to a dome collapse of Soufrière Hill volcano, Montserrat", *Geophysical research letters*, vol. 36, no. 6, 2006.
- [36] A. Budi-Santoso, P. Lesage, S. Dwiyono, S. Sumarti, Subandriyo, Surono, P. Jousset, and J.-P. Metaxian, "Analysis of the seismic activity associated with the 2010 eruption of Merapi Volcano, Java", *Journal of volcanology and geothermal research*, vol. 261, pp. 153–170, 2013, Merapi eruption.
- [37] E. Gossard and W. Hooke, *Waves in the atmosphere*. New York: Elsevier, 1975.
- [38] P. G. Baines and S. Sacks, "Atmospheric internal waves generated by explosive volcanic eruptions", *Geological society, london, memoirs*, vol. 39, no. 1, pp. 153–168, 2014.
- [39] H. Kanamori, J. Mori, and D. G. Harkrider, "Excitation of atmospheric oscillations by volcanic eruptions", *Journal of geophysical research: Solid earth*, vol. 99, no. B11, pp. 21 947–21 961, 1994.
- [40] M. Ripepe, G. Barfucci, S. De Angelis, D. Delle Donne, G. Lacanna, and E. Marchetti, "Modeling volcanic eruption parameters by near-source internal gravity waves", *Scientific reports*, vol. 6, 36727 EP –, 2016.
- [41] T. Mikumo and B. A. Bolt, "Excitation mechanism of atmospheric pressure waves from the 1980 Mount St Helens eruption", *Geophysical journal international*, vol. 81, no. 2, pp. 445–461, 1985.
- [42] T. Fukuzono, "A new method for predicting the failure time of aslope.", *Proceedings of 4th international conference and fieldworkshop on landslides*, pp. 145–150, 1985.
- [43] V. K. Birman, E. Meiburg, and M. Ungarish, "On gravity currents in stratified ambients", *Physics of fluids*, vol. 19, no. 8, p. 086 602, 2007.

- [44] R. Amen and T. Maxworthy, "The gravitational collapse of a mixed region into a linearly stratified fluid", *Journal of fluid mechanics*, vol. 96, no. 1, pp. 65–80, 1980.
- [45] T. Maxworthy, J. Leilich, J. E. Simpson, and E. H. Meiburg, "The propagation of a gravity current into a linearly stratified fluid", *Journal of fluid mechanics*, vol. 453, pp. 371–394, 2002.
- [46] G. Wadge, B. Voight, R. S. J. Sparks, P. D. Cole, S. C. Loughlin, and R. E. A. Robertson, "Chapter 1 an overview of the eruption of Soufrière Hills Volcano, Montserrat from 2000 to 2010", *Geological society, london, memoirs*, vol. 39, no. 1, pp. 1.1–40, 2014.
- [47] G. Ulivieri, E. Marchetti, M. Ripepe, I. Chiambretti, G. D. Rosa, and V. Segor, "Monitoring snow avalanches in northwestern Italian Alps using an infrasound array", *Cold regions science and technology*, vol. 69, no. 2, pp. 177–183, 2011, International Snow Science Workshop 2010 Lake Tahoe.
- [48] *Monitoring unstable parts in the ice-covered Weissmies northwest face*, 2016.
- [49] M. Arattano and L. Marchi, "Measurements of debris flow velocity through cross-correlation of instrumentation data", *Natural Hazards and Earth System Science*, vol. 5, no. 1, pp. 137–142, Jan. 2005.
- [50] A. Burtin, L. Bollinger, J. Vergne, R. Cattin, and J. L. Nábělek, "Spectral analysis of seismic noise induced by rivers: A new tool to monitor spatiotemporal changes in stream hydrodynamics", *Journal of geophysical research*, vol. 113, no. B5, 2008.
- [51] A. Kogelnig, J. Hubl, E. Suriñach, I. Vilajosana, and B. W. McArdell, "Infrasound produced by debris flow: Propagation and frequency content evolution", *Natural hazards*, vol. 70, no. 3, pp. 1713–1733, 2014.
- [52] A. Schimmel, J. Hübl, B. McArdell, and F. Walter, "Automatic identification of alpine mass movements by a combination of seismic and infrasound sensors", *Sensors*, 2018.
- [53] J. W. Kean, J. A. Coe, V. Coviello, J. B. Smith, S. W. McCoy, and M. Arattano, "Estimating rates of debris flow entrainment from ground vibrations", *Geophysical research letters*, vol. 42, no. 15, pp. 6365–6372, 2015.

- [54] F. Walter, A. Burtin, B. W. McArdell, N. Hovius, B. Weder, and J. M. Turowski, "Testing seismic amplitude source localization for fast debris-flow detection at Illgraben, Switzerland", *Nat. hazards earth syst. sci.*, vol. 17, pp. 935–955, 2017.
- [55] V. H. Lai, V. C. Tsai, M. P. Lamb, T. P. Ulizio, and A. R. Beer, "The seismic signature of debris flows: Flow mechanics and early warning at Montecito, California", *Geophysical research letters*, vol. 45, no. 11, pp. 5528–5535, 2018.
- [56] V. C. Tsai, B. Minchew, M. P. Lamb, and J. Ampuero, "A physical model for seismic noise generation from sediment transport in rivers", *Geophysical research letters*, vol. 39, no. 2, n/a–n/a, 2012.
- [57] F. Gimbert, V. C. Tsai, and M. P. Lamb, "A physical model for seismic noise generation by turbulent flow in rivers", *Journal of geophysical research: Earth surface*, vol. 119, no. 10, pp. 2209–2238, 2014.
- [58] B. Schmandt, R. C. Aster, D. Scherler, V. C. Tsai, and K. Karlstrom, "Multiple fluvial processes detected by riverside seismic and infrasound monitoring of a controlled flood in the Grand Canyon", *Geophysical research letters*, vol. 40, no. 18, pp. 4858–4863, 2013.
- [59] N. Kudo, "Control of infrasonic noise from a waterfall", *Journal of low frequency noise, vibration and active control*, vol. 12, no. 4, pp. 149–155, 1993.
- [60] H. N. Feng, Y. C. Yang, I. P. Chunchuzov, and P. X. Teng, "Study on infrasound from a water dam", *Acta acustica united with acustica*, vol. 100, no. 2, pp. 226–234, 2014.
- [61] J. Hubl, A. Schimmel, A. Kogelnig, E. Suriñach, I. Vilajosana, and B. W. McArdell, "A review on acoustic monitoring of debris flow", *International journal of safety and security engineering*, vol. 3, no. 2, pp. 105–115, 2013.
- [62] M. Hurlimann, D. Rickenmann, and C. Graf, "Field and monitoring data of debris-flow events in the Swiss Alps", *Canadian geotechnical journal*, vol. 40, no. 1, pp. 161–175, 2003.

- [63] L. G. Evers and H. W. Haak, "Listening to sounds from an exploding meteor and oceanic waves", *Geophysical research letters*, vol. 28, no. 1, pp. 41–44, 2001.
- [64] H. T. Chou, Y. L. Chang, and S. C. Zhang, "Acoustic signals and geophone response of rainfall-induced debris flows", *Journal of the chinese institute of engineers*, vol. 36, no. 3, pp. 335–347, 2013.
- [65] J. R. Bowman, "Ambient infrasound noise", *Geophysical research letters*, vol. 32, no. 9, 2005.
- [66] D. L. Liu, X. P. Leng, F. Q. Wei, S. J. Zhang, and Y. Hong, "Monitoring and recognition of debris flow infrasonic signals", *Journal of mountain science*, vol. 12, no. 4, pp. 797–815, 2015.
- [67] G. Lacanna and M. Ripepe, "Influence of near-source volcano topography on the acoustic wavefield and implication for source modeling", *Journal of volcanology and geothermal research*, vol. 250, pp. 9–18, 2013.
- [68] A. Schimmel and J. Hubl, "Automatic detection of debris flows and debris floods based on a combination of infrasound and seismic signals", *Landslides*, vol. 13, no. 5, pp. 1181–1196, 2016.
- [69] C. A. L. Szuberla and J. V. Olson, "Uncertainties associated with parameter estimation in atmospheric infrasound arrays", *The journal of the acoustical society of america*, vol. 115, no. 1, pp. 253–258, 2004.
- [70] S. Rost and C. Thomas, "Array seismology: Methods and applications", *Reviews of geophysics*, vol. 40, no. 3, 2002.
- [71] E. D. Scott, C. T. Hayward, R. F. Kubichek, J. C. Hamann, J. W. Pierre, B. Comey, and T. Mendenhall, "Single and multiple sensor identification of avalanche-generated infrasound", *Cold regions science and technology*, vol. 47, no. 1, pp. 159–170, 2007.
- [72] E. Marchetti, M. Ripepe, G. Ulivieri, and A. Kogelnig, "Infrasound array criteria for automatic detection and front velocity estimation of snow avalanches: Towards a real-time early-warning system", *Natural hazards and earth system sciences*, vol. 15, no. 11, pp. 2545–2555, 2015.

- [73] J. B. Johnson and J. L. Palma, "Lahar infrasound associated with volcán Villarrica's 3 March 2015 eruption", *Geophysical research letters*, vol. 42, no. 15, pp. 6324–6331, 2015.
- [74] A. Badoux, C. Graf, J. Rhyner, R. Kuntner, and B. W. McArdell, "A debris-flow alarm system for the Alpine Illgraben catchment: Design and performance", *Nat. hazards*, vol. 49, pp. 517–539, 2009.
- [75] F. Schlunegger, A. Badoux, B. McArdell, C. Gwerder, D. Schnydrig, D. Rieke-Zapp, and P. Molnar, "Limits of sediment transfer in an alpine debris-flow catchment, Illgraben, Switzerland", *Quaternary science reviews*, vol. 28, no. 11, pp. 1097–1105, 2009.
- [76] G. Bennett, P. Molnar, B. McArdell, F. Schlunegger, and P. Burlando, "Patterns and controls of sediment production, transfer and yield in the Illgraben", *Geomorphology*, vol. 188, pp. 68–82, 2013.
- [77] C. Berger, B. W. McArdell, and F. Schlunegger, "Direct measurement of channel erosion by debris flows, Illgraben, Switzerland", *Journal of geophysical research: Earth surface*, vol. 116, 2011.
- [78] B. W. McArdell, P. Bartelt, and J. Kowalski, "Field observations of basal forces and fluid pore pressure in a debris flow", *Geophysical research letters*, vol. 34, no. 7, 2007.
- [79] T. Mulder and J. Alexander, "The physical character of subaqueous sedimentary density flows and their deposits", *Sedimentology*, vol. 48, no. 2, pp. 269–299, 2001.
- [80] B. C. Kneller, S. J. Bennett, and W. D. McCaffrey, "Velocity structure, turbulence and fluid stresses in experimental gravity currents", *Journal of geophysical research: Oceans*, vol. 104, no. C3, pp. 5381–5391, 1999.
- [81] C. Gladstone, L. J. Ritchie, R. S. J. Sparks, and A. W. Woods, "An experimental investigation of density-stratified inertial gravity currents", *Sedimentology*, vol. 51, no. 4, pp. 767–789, 2004.
- [82] C. Hartel, E. Meiburg, and F. Necker, "Analysis and direct numerical simulation of the flow at a gravity-current head. part 1. flow topology and front speed for slip and no-slip boundaries", *Journal of fluid mechanics*, vol. 418, pp. 189–212, 2000.

- [83] T. Maxworthy, "Experiments on gravity currents propagating down slopes. part 2. the evolution of a fixed volume of fluid released from closed locks into a long, open channel", *Journal of fluid mechanics*, vol. 647, p. 27, 2010.
- [84] H. E. Huppert and J. E. Simpson, "The slumping of gravity currents", *Journal of fluid mechanics*, vol. 99, no. 04, p. 785, 1980.
- [85] O. Roche, S. Monserrat, Y. Niño, and A. Tamburrino, "Experimental observations of water-like behavior of initially fluidized, dam break granular flows and their relevance for the propagation of ash-rich pyroclastic flows", *Journal of geophysical research*, vol. 113, no. B12, 2008.
- [86] L. A. Amy, "Abrupt transitions in gravity currents", *Journal of geophysical research*, vol. 110, no. F3, 2005.
- [87] E. C. P. Breard, G. Lube, J. R. Jones, J. Dufek, S. J. Cronin, G. A. Valentine, and A. Moebis, "Coupling of turbulent and non-turbulent flow regimes within pyroclastic density currents", *Nature geoscience*, vol. 9, no. 10, pp. 767–771, 2016.
- [88] T. von Kármán, "The engineer grapples with nonlinear problems", *Bulletin of the american mathematical society*, vol. 46, no. 8, pp. 615–683, 1940.
- [89] T. B. Benjamin, "Gravity currents and related phenomena", *Journal of fluid mechanics*, vol. 31, pp. 209–248, 1968.
- [90] J. Dufek, T. E. Ongaro, and O. Roche, "Chapter 35 - pyroclastic density currents: Processes and models", in *The encyclopedia of volcanoes (second edition)*, H. Sigurdsson, Ed., Second Edition, Amsterdam: Academic Press, 2015, pp. 617–629, ISBN: 978-0-12-385938-9.
- [91] O. Roche, "Depositional processes and gas pore pressure in pyroclastic flows: An experimental perspective", *Bulletin of volcanology*, vol. 74, no. 8, pp. 1807–1820, 2012.
- [92] M. Cerminara, T. Esposti Ongaro, and L. C. Berselli, "Ashee-1.0: A compressible, equilibrium eulerian model for volcanic ash plumes", *Geoscientific model development*, vol. 9, no. 2, pp. 697–730, 2016.

- [93] M. Cerminara, T. E. Ongaro, and A. Neri, "Large eddy simulation of gas-particle kinematic decoupling and turbulent entrainment in volcanic plumes", *Journal of volcanology and geothermal research*, vol. 326, pp. 143–171, 2016, Numerical models of volcanic eruption plumes: inter-comparison and sensitivity.
- [94] M. Cerminara, "Modeling dispersed gas-particles turbulence in volcanic ash plumes", *Phd thesis*, 2016.
- [95] J. Ferry and S Balachandar, "Equilibrium expansion for the eulerian velocity of small particles", *Powder technology*, vol. 125, no. 2, pp. 131–139, 2002, The fourth international conference on multiphase Flow.
- [96] S. B. Pope, *Turbulent flows*. Cambridge University Press, 2001.
- [97] M. Lesieur, Metais, and Comte, "Large-eddy simulations of turbulence", *Journal of fluids and structures*, 2007.
- [98] E. Garnier, N. Adams, and P. Sagaut, "Large eddy simulation for compressible flows", 2009.
- [99] J. H. Ferziger and M. Peric, "Further discussion of numerical errors in cfd", *International journal for numerical methods in fluids*, vol. 23, no. 12, pp. 1263–1274, 1996.
- [100] P. Sweby, "High resolution schemes using flux limiters for hyperbolic conservation laws", *Siam journal on numerical analysis*, vol. 21, no. 5, pp. 995–1011, 1984.
- [101] C. K. W. Tam and L. Auriault, "Jet mixing noise from fine-scale turbulence", *Aiaa journal*, vol. 37, no. 2, pp. 145–153, 1999.
- [102] R. S. Matoza, D. Fee, M. A. Garcés, J. M. Seiner, P. A. Ramón, and M. A. H. Hedlin, "Infrasonic jet noise from volcanic eruptions", *Geophysical research letters*, vol. 36, no. 8, 2009.
- [103] T. Poinso and S. K. Lele, "Boundary conditions for direct simulations of compressible viscous flows", *J. comput. phys.*, vol. 101, pp. 104–129, 1992.
- [104] J. Etienne, E. Hinch, and J. Li, "A lagrangian-eulerian approach for the numerical simulation of free-surface flow of a viscoelastic material", *Journal of non-newtonian fluid mechanics*, vol. 136, no. 2, pp. 157–166, 2006.

- [105] P. M. Morse and K. U. Ingard, *Theoretical acoustic*, 978-0691024011. Princeton University Press, 1987.

Acknowledgements

Among those who deserve to be acknowledged for their contribution to this work, I would like, in particular, to mention:

My supervisors Prof. Maurizio Ripepe and Prof. Emanuele Marchetti. With their experience they guided me into the world of the experimental geophysics and volcano acoustic monitoring. With them I want to thank the entire *Laboratory of Experimental Geophysics (LGS, University of Firenze)* group, for the fruitful discussions and the close cooperation during the geophysical field campaigns along these three years.

My supervisor Dr. Matteo Cerminara, *Istituto Nazionale di Geofisica e Vulcanologia (INGV, Sezione di Pisa)*, for his work and support with the computational modeling. Most of the original results presented in this thesis would not have been possible without his hard work and enthusiasm. This encouraged me to face all that mathematical and computational issues in physical modeling that are not trivial for a geologist.

Moreover, I want to warmly thank Kristin Jonsdottir and Sara Barsotti for their kind hospitality at the *Icelandic Meteorological Office (IMO, Iceland)*, their generous scientific and technical support and their friendship. The research period I spent in Iceland made me grow significantly both professionally and personally.

I would like also to thank Prof. Raffaello Cioni, University of Firenze, for his valuable insights about physical volcanology. Our discussions about science and Academia were of great value for me. Finally, I thank Prof. Lorella Francalanci, as the coordinator of my Ph.D. program at the University of Firenze. The manuscript has been improved by the comments of two reviewers: Prof. S. De Angelis (*University of Liverpool*) and Prof. N. Wallenstein (*University of the Azores*).